Probing bistable Si dynamics and GaSb nanostructures in GaAs

Citation for published version (APA):
Smakman, E. P. (2014). *Probing bistable Si dynamics and GaSb nanostructures in GaAs*. [Phd Thesis 1 (Research TU/e / Graduation TU/e), Applied Physics and Science Education]. Technische Universiteit Eindhoven. https://doi.org/10.6100/IR778507

DOI:
[10.6100/IR778507](10.6100/IR778507)

Document status and date:
Published: 01/01/2014

Document Version:
Publisher's PDF, also known as Version of Record (includes final page, issue and volume numbers)

Please check the document version of this publication:

• A submitted manuscript is the version of the article upon submission and before peer-review. There can be important differences between the submitted version and the official published version of record. People interested in the research are advised to contact the author for the final version of the publication, or visit the DOI to the publisher's website.
• The final author version and the galley proof are versions of the publication after peer review.
• The final published version features the final layout of the paper including the volume, issue and page numbers.

Link to publication

Probing Bistable Si Dynamics and GaSb Nanostructures in GaAs

PROEFSCHRIFT

door

Erwin Paul Smakman

geboren te Tilburg

Dit proefschrift is goedgekeurd door de promotoren en de samenstelling van de promotiecommissie is als volgt:

voorzitter:	prof.dr.ir. G.M.W. Kroesen
1e promotor:	prof.dr. P.M. Koenraad
2e promotor:	prof.dr. J. Millunchick (University of Michigan)
leden:	prof.dr.ir. O.J. Luiten
	prof.dr. R. Möller (University of Duisburg-Essen)
	dr. M. Hayne (Lancaster University)
	prof.dr. E.P.A.M. Bakkers
	prof.dr.ir. H.J.W. Zandvliet (University of Twente)

Contents

Chapter 1

Introduction

We can not imagine the world today without electronic devices, of which the basic components have shrunk to sizes far beyond our imagination. In an inspiring lecture given by Feynman in 1959, he pointed out that "there is plenty of room at the bottom" [1], proposing the possibility to observe and manipulate on the atomic scale. One obstacle to overcome towards nanoscale miniaturization at the time was the relatively limited resolution of the scanning electron microscope. Another challenge was how to fabricate nanoscale structures and devices in the first place. With his talk, he opened up the field of nanotechnology, which would only really start to develop decades later. However, the downscaling of commercial electronic components had already begun. In 1965, Moore published an outlook predicting that the amount of transistors on a chip would double roughly every two years [2], which has been fairly accurate up to now. With the invention of the scanning tunneling microscope (STM) in 1981 [3, 4], observation and manipulation of single atoms became possible [5]. Shortly after, other scanning probe techniques were developed, further increasing the possibilities at the nanoscale. The field of nanotechnology had truly emerged.

Semiconductor material provides functionality for many electronic devices, from computer chips to solar cells. The electronic and optical properties of semiconductor materials originate in the bandgap, or a "forbidden" energy range for charge carriers. This bandgap can be engineered by choosing the appropriate alloy of atomic species that represent the host lattice. By using combinations of two or more elements in the group III and V columns or in the group II and VI columns of the periodic table, a whole range of bandgap energies is available. In this thesis, the focus is on III-V semiconductor material and on GaAs in particular.

Semiconductor heterostructures can be engineered at the nanometer scale, enabling the confinement of charge carriers in one or more dimensions. If both electrons and holes are confined in the same nanostructure, this is beneficial for charge carrier recombination, which promotes optical properties important in e.g. solar cells and light emitting diodes. If the charge carriers are spatially separated, the recombination rate is low, enabling long storage times and memory functionality. There are many possible geometries for nanostructures, for example by confinement in 1D in the form of quantum wells, or in 2D represented by nanowires or nanostripes. Nanostructures can also be engineered to confine carriers in 3D. These quantum dots (QDs) or related structures can for example be constructed by self-organized growth [6, 7]. In the so-called Stranski–Krastanov growth mode, the strain between the QD and the surrounding host plays an important role in the formation process, which originates in the slightly different lattice constant of the two materials. The QDs act as "artificial" atoms, because discrete energy levels for the charge carriers arise due to the quantum confinement at the nanoscale. By choosing the right material combination and by tailoring their size, nanostructures can be fabricated to produce the desired opto–electronic properties for many applications.

An important characteristic of semiconductors is how they are doped, i.e. if they have donor or acceptor atoms embedded in the host matrix to provide easily available charge carriers. The weakly bound electrons or holes of the dopant atoms can be ionized by electrical, optical and thermal effects and play a large role in the transport of charge, spin and heat through the material. The study of single dopants is becoming more and more relevant [8, 9], because their local properties influence the functionality of electronic devices that are ever decreasing in size [10, 11].

The work presented in this thesis is aimed at investigating structural, electronic, time–resolved, optical and magnetic properties of nanostructures and dopants in GaAs with STM. There are three main topics. Two chapters are dedicated to the nanoscale analysis of GaSb QDs. The goal here is to investigate the influence of various growth parameters on the morphology of the nanostructures and in that way understand their disintegration process that occurs often during the capping of the QD layers. Subsequently, the capping with Al–rich layers is explored, meant to further preserve the GaSb QD shape and enhance the optical quality of the material. More pure and intact QDs result in a larger hole localization energy, which is interesting for many opto–electronic applications. Another two chapters outline the detailed analysis of bistable charge switching on Si dopants located in the top layer of the (110) surface. The focus is on finding out how optical manipulation with

a laser, lateral positioning of the tip and the applied tunneling conditions influence the switching dynamics. The analysis as a whole gives a fundamental understanding of the charge switching process on a single dopant, which has implications for the design of electronic devices that are reaching dimensions where only a few dopants determine their functionality. Finally, two chapters treat the probing of optical and magnetic properties of nanoscale structures. Electroluminescence induced by the STM tip is used to investigate single dopants in the semiconductor surface. Here the goal is to understand the origin of the atomic–scale variation in the luminescence intensity. This could help in improving the technique further to be able to observe spectral features of single nanostructures and dopants. Furthermore, magnetic tips are employed to determine the magnetic state of single MnAs nanoclusters, as well as their electronic structure. The focus is on linking the local information obtained on the nanoscale to the macroscopic properties of the material, to aid in the further optimization of this potential room–temperature ferromagnetic semiconductor material.

Although the three main topics have a different character, several general themes can be extracted. First, the investigation of nanoscale structures in GaAs presented in this thesis show the versatility of the STM technique as a probe of many properties on the atomic–scale. Also, some sort of instability is found in different forms throughout the thesis: as the disintegration process in GaSb QDs, as the bistable switching of Si dopants and as the switching of the magnetic state of MnAs islands. Finally, there is often a connection to nanoscale devices: GaSb QDs can be used as potential flash memory cells and bistable dopants can influence or even serve themselves as logic elements.

In this thesis, various nanostructures and dopants in GaAs are investigated with cross–sectional (X–)STM. For this technique, the sample is cleaved along a crystal direction in ultra–high vacuum (UHV), exposing the cross–sectional surface of the semiconductor. As a result, the surface is free from contaminants and flat. This allows the atomically resolved inspection of the host lattice and of nanostructures and dopants in particular. With X–STM, nanoscale properties can be probed that are often inaccessible for other techniques. In the case of nanostructures, their shape and composition are of interest [12, 13], but also effects of mechanical strain can be made visible with X–STM [14]. In the case of dopant atoms, the extent and nature of the bonds with the surrounding host matrix have a profound influence on how they appear in the X–STM measurements and give information about their role in electronic [15, 16] and magnetic [17, 18] properties of the material.

GaSb and GaAs have a staggered, type–II band alignment in which holes

are confined and electrons repelled from the QD region. This results in a low recombination rate for charge carriers, which makes this material system interesting for memory applications [19, 20]. In Chap. 3, the morphology of GaSb/GaAs QDs is investigated. These nanostructures were grown with molecular beam epitaxy (MBE) and were mapped out in atomic detail with X–STM. Because of the high amount of strain between the pure GaSb QDs and the surrounding GaAs, many nanostructures disintegrate during overgrowth with capping layers. The QD growth is investigated by tuning various MBE growth parameters, e.g. temperature and layer thickness. The X–STM data provides a way to statistically compare the various morphologies for each growth condition and in this way find the optimal settings for growing pure and intact nanostructures. Complementary analysis on the QDs was performed with the help of $\mathbf{k} \cdot \mathbf{p}$ calculations, atom probe tomography (APT), photoluminescence (PL) and scanning tunneling spectroscopy (STS). To preserve the shape of the original uncapped nanostructures even better, overgrowth with Al–rich capping materials is explored with a similar X–STM analysis in Chap. 4. Moreover, stacking faults that appear around the QDs are visualized on the atomic scale and linked to PL results.

The Si atom in the (110) surface layer of GaAs exhibits bistable behavior, switching between a negative and positive charge state [21]. The electric field of the STM tip has a strong influence on the switching of the dopant, which enables manipulation of the charge state, but also makes it difficult to understand the relevant physical processes involved. To probe the system in a different and independent way, the sample was illuminated by a laser during STM operation, described in Chap. 5. The Si atom can be reversibly switched between its positive and negative charge state by turning the laser on and off respectively. The electron escape and capture processes play an important role in the bistability. The dynamics of the switching process were investigated by restricting the STM tip laterally on top of a single Si atom and recording the tip height. This enables the tracking of the charge on the dopant in time, resulting in a random telegraph noise signal. This is the topic of Chap. 6. A physical model was developed to explain the observed dynamics of switching behavior varying with the applied tunneling conditions. Additionally, a single Si dopant was employed as a memory element in the GaAs matrix by manipulating, or "writing", and probing, or "reading", the charge state with the STM tip. This single atom memory demonstrates the potential for using single dopants as the functional building blocks of nanoscale semiconductor devices, a field coined as "solotronics" [8].

In addition to structural and electronic investigations, the STM also enables the detection of optical and magnetic properties of the surface. Scan-

ning tunneling luminescence (STL) is based on collecting electroluminescence from the surface, where the current is injected by the STM tip. In semiconductor material, minority charge carriers are supplied by the tip, that recombine with the majority charge carriers of the doped sample, resulting in optical emission. This is the topic of Chap. 7, where the effects of Si dopants in GaAs on the STL signal are studied. Nanoscale variations are observed in the STL intensity that can be linked to the atomic corrugation and dopant distribution, which are also visible in the simultaneously obtained topography. In Chap. 8 an X–STM study of MnAs nanoclusters in GaAs is presented. This semiconductor material is promising for providing room–temperature ferromagnetism. STS reveals a bandgap that is related to the Coulomb charging of a metallic MnAs cluster. Spin–polarized (SP–)STM was employed to record the switching of an island between two magnetic states. It turns out that at $T = 77$ K only smaller islands exhibit the switching, while larger clusters remain stable. This result supports the view that the larger–sized clusters are responsible for sustaining ferromagnetism at higher temperatures.

Chapter 2

Experimental Techniques

In this chapter, the experimental methods are introduced that are relevant for the work in this thesis. The basic technique is scanning tunneling microscopy (STM), operated under ultra-high vacuum (UHV) conditions to study semi-conductor materials. Briefly the preparation of tips and samples is discussed. Extensions are made to the STM setup by analyzing the noise present in the tunneling current and by observing electroluminescence from the surface. The final part of this chapter is dedicated to explaining the imaging on III-V semi-conductors and embedded dopants and nanostructures in particular. The use of IV-spectroscopy is treated as well as its application in probing magnetic structures with spin-polarized (SP-)STM.

2.1 Scanning Tunneling Microscopy

In 1981 the STM was invented by Binning and Rohrer at IBM [3, 4]. They received the Nobel prize for their work in 1986. Together with the development of the atomic force microscope (AFM) and other scanning probe techniques, it has allowed for the investigation of materials at sizes down to the atomic scale. The basic STM principle of imaging the topography and conductivity of surfaces has since been extended to also probe other material properties, e.g. nanoscale magnetism [22, 23, 24] and luminescence [25, 26, 27].

The STM technique is based on quantum tunneling between a needle-shaped tip and a (semi)conducting sample. Although electronic transport through vacuum is classically forbidden, at the nanoscale the wavefunctions of charge carriers can penetrate a finite potential barrier and allow the transmission of a net current. The transmission is determined by the wavefunction overlap between the states of the tip and those of the sample. In the STM,
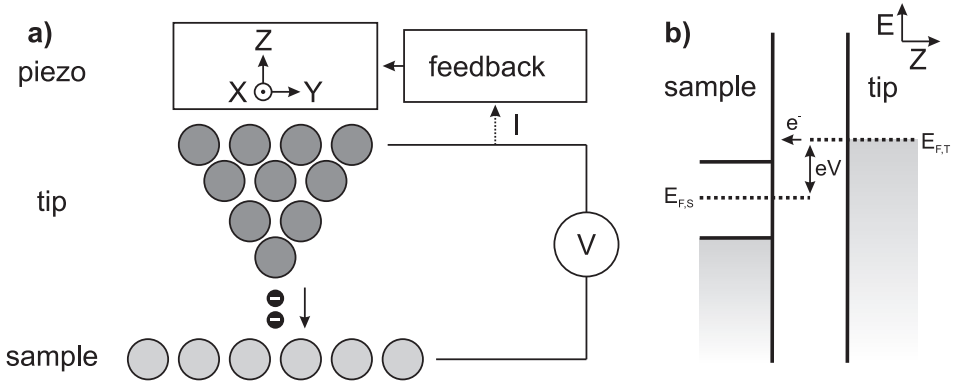
Figure 2.1: (a) The STM principle, with positive bias voltage applied to the sample. (b) The corresponding energy diagram for electrons flowing from a metallic tip through the vacuum barrier to a semiconductor sample.

a small bias voltage is applied between tip and sample and the resulting tunneling current is recorded after conversion to a voltage–scale by a current amplifier. During typical operation, the current is kept constant by means of a feedback loop that adjusts the height of the tip, see Fig. 2.1. The tip is scanned over the surface to record a 2D topographic map. The sub–nanometer precision of the STM is made possible by the development of piezoelectric ceramic materials that allow a precise control over the movement of the tip. Other important prerequisites are advanced vibration isolation methods and low noise electrical amplifiers to ensure a good signal–to–noise ratio.

The theoretical description of the 1D tunneling process through a barrier is based on work by Bardeen [28] and extended for STM by Tersoff and Haman [29, 30]. The theoretical background is treated in detail in textbooks, for example by Chen [31]. The tunneling current I can be expressed in terms of the local density of states (LDOS) ρ of both tip and sample, denoted by subscript T and S respectively:

$$I = \frac{4\pi e}{\hbar} \int_0^{eV} \rho_S(E_{F,S} + \epsilon)\rho_T(E_{F,T} - eV + \epsilon)|M|^2 d\epsilon. \qquad (2.1)$$

Here e is the electron charge, $\hbar$ the reduced Planck's constant, V the applied bias voltage, E_F the Fermi level and M the tunnel matrix element. V is defined as the voltage applied to the sample, which means that for $V > 0$ electrons tunnel from the occupied states in the tip to the empty states of the sample and for $V < 0$ it is vice versa.

In the limit of $T = 0$ K, all states below the Fermi energy are filled and

all states above the Fermi energy are empty. This approximation is still valid at finite temperatures, as long as the relevant energy scales are much larger than the thermal energy. If one assumes that the tip LDOS is flat and the electrons available for tunneling in the tip have an *s*-wave character, then $|M|^2 \propto \exp(-2\kappa d)$, where κ is the inverse decay length in vacuum and d is the distance between sample and tip. Eq. 2.1 can now be simplified:

$$I \propto \int_0^{eV} \rho_S(E_{F,S} + \epsilon) \exp(-2\kappa d) \mathrm{d}\epsilon. \qquad (2.2)$$

With a constant bias voltage and the tip fixed at a lateral position, the integrated LDOS of the sample is constant and Eq. 2.2 reduces to:

$$I \propto \exp(-2\kappa d). \qquad (2.3)$$

This shows the exponential dependence of the tunneling current on the distance between tip and sample. On a semiconductor, κ is in the order of 0.1 nm [32, 33], which indicates that most of the tunneling current flows through the outermost atom of the tip. As a result, the height resolution of the STM is only limited by vibrations and electrical noise in the system and is typically in the order of a few pm. Furthermore, often a lateral resolution is observed in STM measurements that allows the imaging of the atomic corrugation of the sample surface. For the work described in this thesis, W and Cr tips are used, for which the *d*-states of the tip are more important for tunneling than the *s*-states that were used in the approximation of Eqs. 2.2 and 2.3. This influences the tunnel matrix element *M*, making it even more spatially dependent and therefore further enhancing the lateral resolution of the STM measurements. Depending on the type of surface being imaged, the lateral resolution can reach around 100 pm. The high spatial resolution in STM enables not only the study of materials on the atomic scale, but also the manipulation of single atoms on a surface [5, 34] and their embedding in the surface [35, 36].

For the work in this thesis, two STM systems were available to perform measurements on, one operating at room temperature (RT) and one at low temperature (LT). The RT setup contains an Omicron STM1, TS-2 scanner, regulated by an Omicron Scala controller. The rest of the system is home-built. The LT-STM is a commercial Omicron system, regulated by an Omicron Matrix controller. The inner cryostat is connected to the STM scanner head and can be filled with either liquid N_2 to measure at $T = 77$ K or liquid He to measure at $T = 5$ K. The outer cryostat is in either case filled with liquid N_2. The hold time for cryogenic fluids is roughly 24 hours, allowing for *IV*-spectroscopy and other time-demanding measurements. Measurements in

both systems are performed under UHV conditions, at pressures $\leq 6 \times 10^{-11}$ mbar. The preparation of tips and samples is done in a separate chamber, where the pressure is typically one or two orders of magnitude higher. The STMs are isolated from external vibrational noise using eddy–current damping of the STM head and active damping under the setup table. Both systems are positioned on their own concrete island at the ground floor, detached from the rest of the building for further vibration isolation. The electronic noise is limited by filtering the current coming from the power grid and by using carefully designed IV–conversion with a high signal–to–noise ratio for reading out the tunneling current.

Before the actual measurement, the STM tip is brought into close prox- imity of the sample surface by approaching with slip–stick–type coarse piezo motors, operated with a remote control. An optical microscope provides a view of the sample and the tip. In the case of a flat surface, a reflected tip image is visible in the sample. This enables the precise positioning of the tip. The approach of the last 10 μm to the surface is done by a software controlled auto–approach with the feedback loop on. The measurement is then started and controlled by the software.

2.2   Tip and Sample Preparation

To obtain atomic resolution and reproducible measurement conditions, the tips made for STM have to be very sharp and stable. The tips are prepared by electrochemical etching of polycrystalline W wire, see Fig. 2.2 (a) [37]. A W wire of around 15 mm long and 0.25 mm in diameter is attached to a tip carrier on one side. The other side is immersed for 75 % into a 2.0 mol KOH solution in water. An applied voltage to a counter–electrode of 7 V starts the etching process and slowly removes W from the wire:

$$W + 2OH^- + 2H_2O = WO_4^{2-} + 3H_2. \qquad (2.4)$$
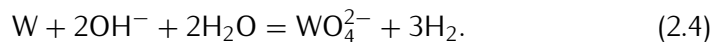
The WO_4^{2-} drops down along the wire and effectively shields the lower part from the etching. This results in a higher reaction velocity at the position where the wire penetrates the solution, eventually leading to a drop–off at that location. The current is delimited by the power supply and the voltage immediately is set to zero when the drop–off occurs. This enables a very sharp tip apex at the meniscus, with a radius in the order of 10 nm. The tip carrier is put into a holder to enable the handling in UHV, where it is kept in its place by a small magnet, see Fig. 2.2 (b).

Additional preparation steps are performed in UHV. The tip is heated to $T = 200$ °C to remove contaminants like oxides, water and organic mate-
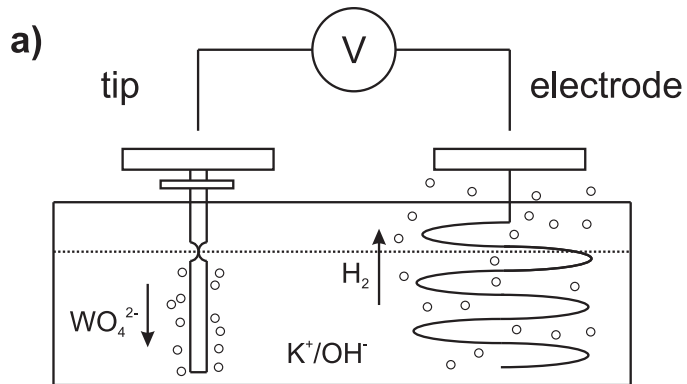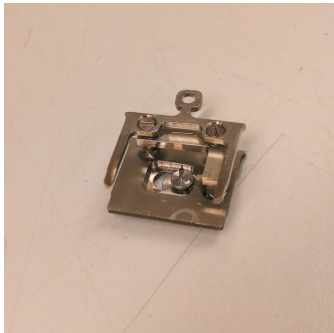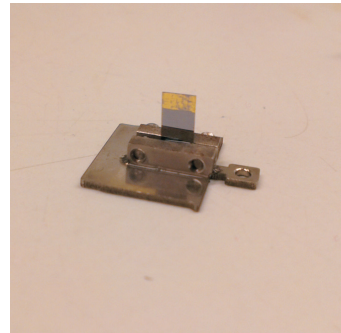
Figure 2.2: (a) Schematic representation of the tip etching method. (b) Tip holder with tip carrier kept onto its place by a small magnet, visible on the right side. (c) Sample holder, in which a contacted semiconductor sample is clamped.

rial. Ar sputtering of the tip apex is performed to enhance the stability during measuring. In the case of an unstable or low-resolution tip, changing the tunneling parameters or applying small voltage pulses often helps in recovering the desired tip quality.

The experiments described in this thesis were conducted on {110} planes of GaAs wafers, that were cleaved in-situ in UHV for cross-sectional (X-)STM. To obtain an atomically flat and clean surface after cleaving, the sample is prepared in the following way. First, the wafer of interest is cut into samples of the appropriate size for X-STM. The width of 4 mm is limited by the sample holders, the height of 10 mm by the transfer positions in the STM setup. Ohmic contacts are then created on these samples, by indiffusion of n-type, Ge/Ni/Au, or p-type, Zn/Ni/Au, material. Contacts are applied on two ends of the sample, to allow the possibility to clamp on both sides. The contacts are not covering the whole surface, to allow space for a scratch that is made to aid the cleaving process in UHV later on. After contacting, the samples are polished down from $400 - 500$ μm to $120 - 150$ μm thickness using aluminum oxide powder with a grain size of 3 μm. The scratch is made along one third of the width of the sample. The sample is then clamped into its metal holder, see Fig. 2.2 (c), using indium as glue and screws to tighten the material.

After insertion into the STM, the sample is baked in the preparation chamber at $T = 150$ °C to get rid of contaminants and transferred to the measurement chamber. Here it is cleaved along the scratch by pushing against the top of the sample with a wobblestick and loaded into the STM head for measuring. As a general trend, samples that contain epilayers with a high build-up of strain are more difficult to cleave, and the amount of atomic step edges per μm is higher. Step edges are typically parallel to the edge of the sample. A high density of step edges can prevent a detailed inspection of the surface, because they obscure the features of interest and they influence the electronic properties of their surrounding. Other cleaving artifacts that can occur are local nm-sized hills or troughs that often appear on or around highly strained nanostructures.

2.3   Scanning Noise Microscopy

Although STM has superior spatial resolution, one drawback is the recording time, which is typically in the kHz range due to the bandwidth of the IV-convertor. This limits the study of fast dynamical processes and tracking of particles on a surface [38]. A possible solution to this problem is the use of high-frequency amplifiers to scan at video rate [39, 40] or to use electrical pump-probe-like experiments [41, 42]. Another approach is to follow the fluc-
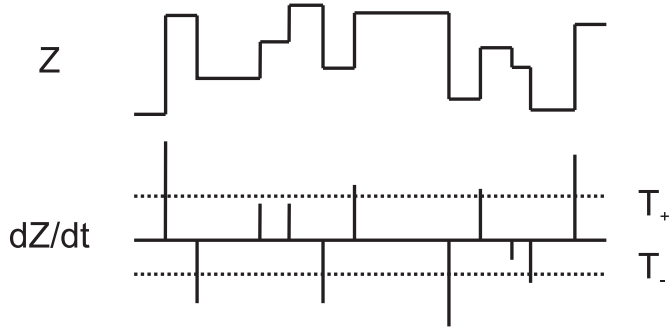
Figure 2.3: Schematic representation of the the SNM technique, where the *Z* signal is used as input with the STM feedback loop on. Abrupt topographic height changes are translated into peaks in the time–differentiated signal. With the appropriate threshold levels T_- and T_+, the relevant height changes are detected.

tuations in the tunneling current with the tip restricted on a single point and record the noise signal, called scanning noise microscopy (SNM) [43]. The application of SNM is interesting for a large range of systems that exhibit some kind of switching at the nanoscale, for example in the study of frustrated rotation of molecules on a surface [44]. In Chap. 6 this technique is employed to study the dynamics of charge switching of bistable Si atoms in the surface of GaAs.

SNM capabilities provided by the Möller group from the University of Duisburg-Essen were added to our LT-STM setup. The input can be either the tunneling current *I* if the feedback loop of the STM is switched off, or the tip height *Z* with the feedback on. The analog electronics extract time-dependent information in real–time during a topography measurement, see Fig. 2.3. The input signal is time–differentiated and the peaks are used for the detection of a step up or a step down. The signal is translated into a voltage scale and the thresholds T_- and T_+ for peak detection are separately set for the "up" and the "down" process. The recorded peaks are integrated and averaged over time by a low–pass filter. The average switching rate *f* is calculated as follows:

$$f = \frac{1}{\tau_{on} + \tau_{off}},$$

(2.5)

where τ_{on} and τ_{off} are the average times the system is in the on and off state respectively. The duty cycle or probability of finding the system in the on state n_{on} is:
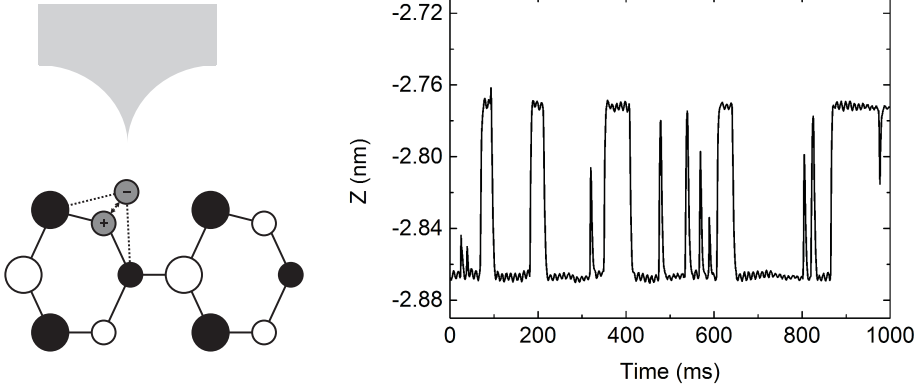
Figure 2.4: (left) Illustration of the switching of a bistable Si atom in the GaAs surface between two charge states. (right) The resulting random telegraph noise signal from topographic height traces, $V = +0.90$ V, $I = 75$ pA.

$$n_{on} = \frac{\tau_{on}}{\tau_{on} + \tau_{off}}, \qquad (2.6)$$

which is a number between 0 and 1. Furthermore, $n_{off} = 1 - n_{on}$.

The sample frequency of the LT–STM Matrix controller is 1 kHz, which imposes limitations on the switching frequency that can be recorded when the feedback loop is on. Additionally, the noise electronics have a dead time of 100 μs, which occurs after the detection of a switching event. However, this is a faster timescale than the STM sample frequency, thus does not limit the frequency range that can be detected.

In Chap. 6, the dynamics of single bistable Si atoms in surface of GaAs are investigated by recording their random telegraph noise. The described experiments are conducted with the feedback loop on, to keep the tunneling conditions the same over time. In Fig. 2.4 a topographic random telegraph noise signal is displayed of a single bistable Si atom. Visible is the discrete switching between two charge states of the Si atom, which directly influences the height of the tip and creates a relative tip–sample distance in the order of 100 pm. This is significantly larger than the background noise level of about 5 pm. The threshold levels T_- and T_+ that detect switches up and down can be determined reliably, as long as there is little change in the input signal over time. The main experimental challenge here is to keep the absolute height difference between the two states the same, because this directly translates

into the absolute peak heights in the time–differentiated signal processed by the noise analyzer. In principle, this stability is achieved by measuring at a low temperature of $T = 5$ K and by keeping the tunneling conditions constant. This allows the atomically resolved mapping of the switching frequency and occupation in the 2D plane.

When the applied tunneling conditions are varied, the absolute height difference between the on and off state changes and the threshold levels have to be adjusted. In this case, a post–measurement analysis of topographic STM height profiles is more straightforward and reliable, because for every experimental setting the threshold levels can be scaled relatively to match the height difference. For this purpose, a Matlab script was developed to extract the frequency and the occupation directly from the topography data.

2.4   Scanning Tunneling Luminescence

Scanning tunneling luminescence (STL) was first demonstrated on metals in 1988 [25] and in 1990 extended to semiconductors [45]. The technique is based on electroluminescence, where charge carriers are injected by the STM tip and photons are collected externally on a detector. The photons are created when the injected charge carriers have enough energy to excite surface plasmons in metals or to create electron–hole pairs in semiconductors. It is also possible to probe magnetic properties of surfaces by looking at the light polarization [46]. In Chap. 7 luminescence of single Si dopant atoms in GaAs is investigated with STL.

Our LT–STM has two optical access points that allow for the detection of luminescence from the surface, see Fig. 2.5 [47]. The light emitting from the surface is captured partially by an $f = 20$ mm lens, which creates a parallel beam that passes through a viewport before exiting the UHV. Outside the chamber it is focused onto an optical fiber, $d = 600$ μm, which guides the light to an Acton Research SpectraPro–300i monochromator. A 576×384 Si liquid N_2 cooled CCD camera operating at $T = 170$ K records the spectra.

The translation and rotation stages for the fiber located outside the vacuum allow precise alignment for optimizing the STL intensity. Because the setup contains two optical access points, one can be illuminated by a lamp to aid the alignment of the optical stage on the other port. The lamp illumination creates an image of the tip and the sample surface at the fiber location. The fiber tip is put into focus at the spot where the image of STM tip is visible. This method greatly simplifies the alignment procedure.

For STL on semiconductors, the quantum efficiency is in the order of $\sim 1 \times 10^{-4}$ [48]. A typical luminescence spectrum on n–type GaAs is de–
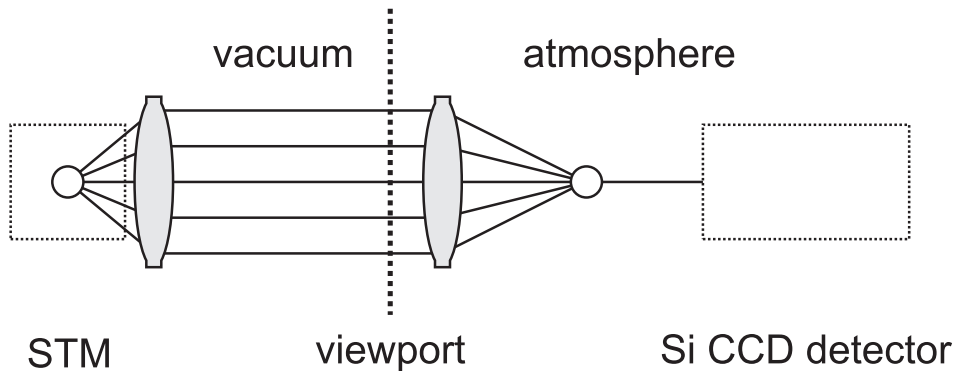
Figure 2.5: The STL setup implemented in our LT–STM. Part of the electro-luminescence from the sample is guided into a parallel beam with a lens. The light passes through a viewport and is then focused onto a fiber leading to a detector [47].
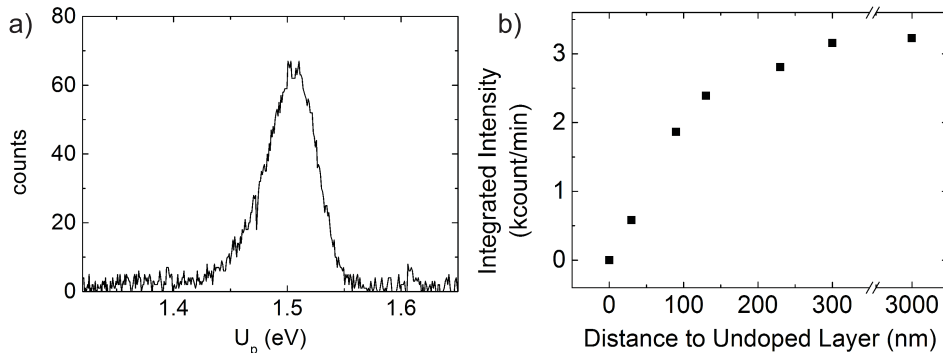
Figure 2.6: (a) Typical STL spectrum recorded on n–type GaAs, $V = -3.60$ V, $I = 800$ pA. (b) Integrated STL intensity obtained on n–type GaAs as function of the lateral distance to undoped GaAs, $V = -3.50$ V, $I = 500$ pA. All spectra taken at $T = 5$ K, with $t_{int} = 5$ min.

picted in Fig. 2.6 (a), where the spectral peak location matches the bandgap of $E_g = 1.52$ eV. The spatial variation of the STL signal is related to the diffusion length of carriers in the semiconductor material, and therefore dependent on a number of parameters such as the doping concentration and the experimental temperature. In Fig. 2.6 (b) the integrated STL intensity is shown, obtained on GaAs n–doped with 2×10^{18} cm^{-2} Si as a function of the lateral distance to an undoped region of GaAs, measured at $T = 5$ K. This allows the estimation of the carrier diffusion length under these conditions. The obtained value is approximately 200 nm, which compares well to numbers found in literature [49].

The flexible design of the LT–STM optics gives the possibility to change the STL arrangement, for example by replacing the detector with a laser to illuminate the sample surface instead. The photo–excitation of carriers in the semiconductor increases the conductivity and in general decreases band bending effects at the surface [50]. In Chap. 5, the effect of illumination on bistable Si in the surface of GaAs is studied.

2.5   III–V Semiconductors

The studied zinc–blende III–V semiconductor materials presented in this work have non–reconstructed {110} surfaces, which are their natural cleavage planes because they are non–polar. These planes provide a flat surface, free of contaminants and without surface states in the band gap, making it ideal for STM [51]. It opens up the possibility to study of dopants and point defects, as well as inspection of heterostructure cross–sections like quantum dots that have been grown in the [001] direction. Fig. 2.7 displays the zinc–blende lattice structure of a III–V semiconductor cleaved along the (110) plane. Along the [001] direction, the distance between the atoms of the same type is the lattice constant a_0 and in the [110] and [1$\bar{1}$0] directions the distance is $a_0/\sqrt{2}$. The top view imaged by the STM results in the characteristic zig–zag rows of the surface [52].

At the semiconductor–vacuum interface, the group V or anion atom buckles slightly outward and the group III or cation atom buckles slightly inward, to obtain thermodynamic equilibrium [53]. As a result of the 27 ° bond rotation, there is a charge transfer between the group III and group V atom at the surface. The dangling bond of the anion is filled with electrons. In the case of the unrelaxed lattice, the group V surface state energy level would be in the bandgap, but in the relaxed situation it shifts into the conduction band. Similarly, the cation dangling bond is empty of electrons and the group III surface state energy level shifts into the valence band.
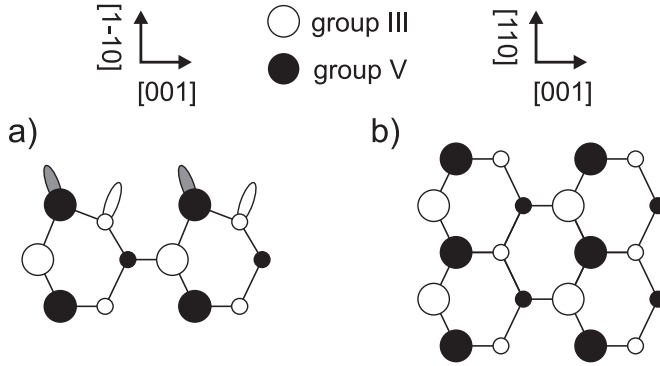
Figure 2.7: Schematic representations of the cleaved and relaxed (110) surface of a zinc–blende semiconductor, (a) perpendicular and (b) parallel to the cleaving plane. The difference in the third dimension is illustrated by the use of larger (closer by) and smaller (farther away) dots that represent the atoms. In (a) the filled (grey) and empty (white) dangling bonds are also indicated at the semiconductor surface.

At negative voltages, the electrons tunnel primarily from the filled valence band states of the group V atoms into the tip. At positive voltages, the electrons tunnel primarily from the tip into the empty conduction band states of the group III atoms. It means that depending on the polarity of the applied bias voltage, the topography is for the largest part determined by either the anions or the cations. Another consequence is that with no surface states in the bandgap, the semiconductor Fermi level is unpinned and the electronic properties of the bulk dominate the STM contrast [54].

2.6   Imaging Dopants and Nanostructures

Dopants in III–V semiconductors have been extensively studied by X–STM [55, 56]. A distinction is often made between shallow and deep dopants, depending on whether their binding energy is roughly below or above 35 meV respectively. Generally, shallow dopants are interesting for bulk electronic applications because they are easily thermally activated. Deep dopants can act as traps for charge carriers and in that way limit electronic transport. Donors have an excess electron available that is not used in a chemical bond. This happens for example when a group IV element occupies the lattice site of a group III atom, like Si_{Ga} in GaAs [57, 58]. Similarly, when a group IV element is placed at a group V site, an extra hole is present that can capture a free
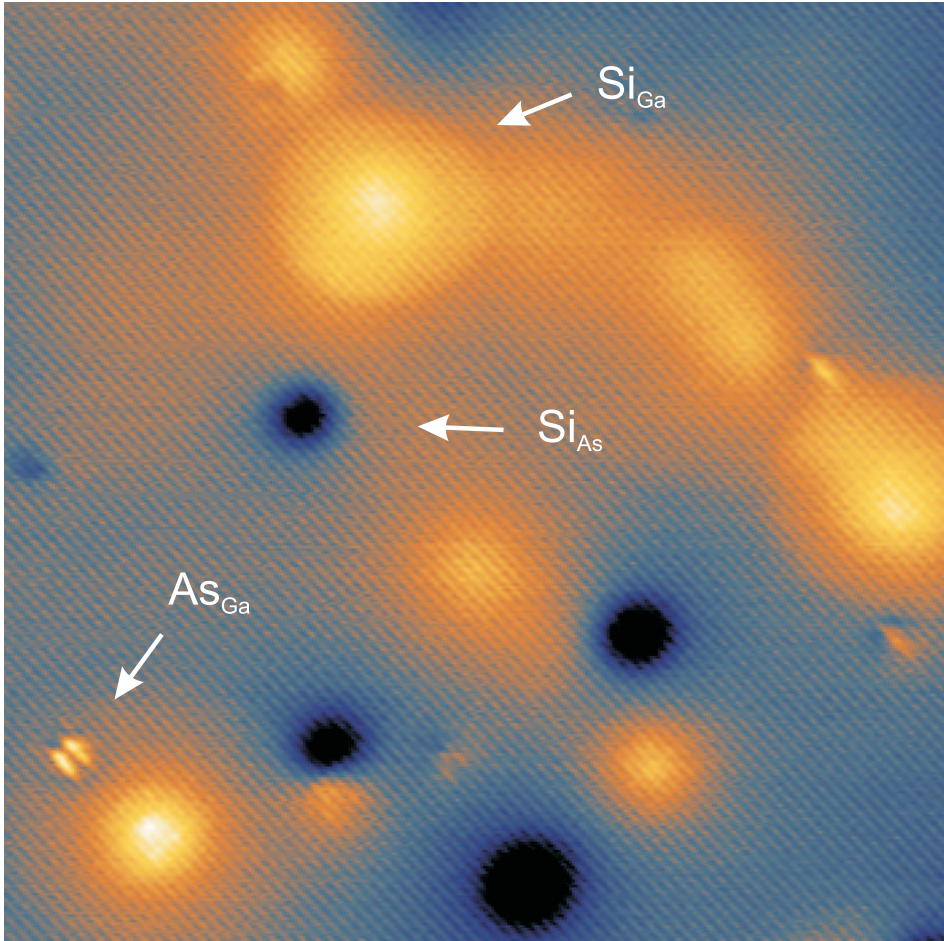
Figure 2.8: Si dopants in GaAs, 35×35 nm^2, $V = +0.50$ V, $I = 70$ pA.

electron. This constitutes an acceptor, like Si_{As} in GaAs [59, 60]. There are many other possibilities for dopants depending on their electronic properties and position in the lattice, for example in GaAs the group II Mn_{Ga} acceptor [61, 17] and the group VI Te_{As} donor [62]. Some dopants can even alter their electronic behavior completely due to a changing electrostatic environment. Examples in GaAs are the switch between an acceptor and isoelectronic state of Fe_{Ga} [63] and the switch between a donor and an acceptor state for Si_{Ga} in the cleaved surface layer treated in Ref. [21] and Chap. 5 and 6 of this thesis.

The amphoteric character of Si in GaAs is visible in Fig. 2.8, where both donors and acceptors are present in the surface due to the auto–compensation effect during the growth of the sample [59, 60]. Si donors appear bright at this positive voltage, because they are ionized by the STM tip. Si acceptors appear dark due to their negative charge. The Coulomb field of the dopants influences the local tunneling conditions, which leads to an apparent height change. The variation in contrast intensity is related to the depth of the donors: donors deeper below the surface are still visible, but much fainter. By analyzing the statistical distribution of intensities measured with STM, the exact atomic layer depth of the dopants in the surface is determined [16, 64]. Furthermore, in the topographic image features with a breaking of their circular symmetry are visible which are probably As_{Ga} anti–site defects [65].

An important effect for imaging semiconductor material with STM is tip induced band bending (TIBB), which makes it difficult to interpret energy levels in the bandgap [66]. The TIBB occurs because the Fermi level of the semiconductor is unpinned and the conduction band and valence band bend when a voltage is applied across the vacuum barrier, see Fig. 2.9 [32]. The difference in Fermi level energy between the tip and sample creates a local electric field. Charge carriers in the semiconductor partially screen this electric field, which results in a Schottky–type barrier. This means there is a depletion region of charge carriers, effectively changing the width of the vacuum gap and influencing the tunneling process. The extent of the TIBB effect is larger when the doping concentration of the semiconductor surface is low, because then the screening length is increased. The TIBB can extend easily over tens of nm and depends also on the polarity of the applied bias voltage and exact tip geometry [67, 33].

The semiconductor bands are flat, i.e. the flatband condition is fulfilled, when the applied bias voltage balances the tip work function W and the electron affinity χ of the semiconductor sample with respect to the vacuum [68]. When the voltage is above the flatband condition, positive charges accumulate
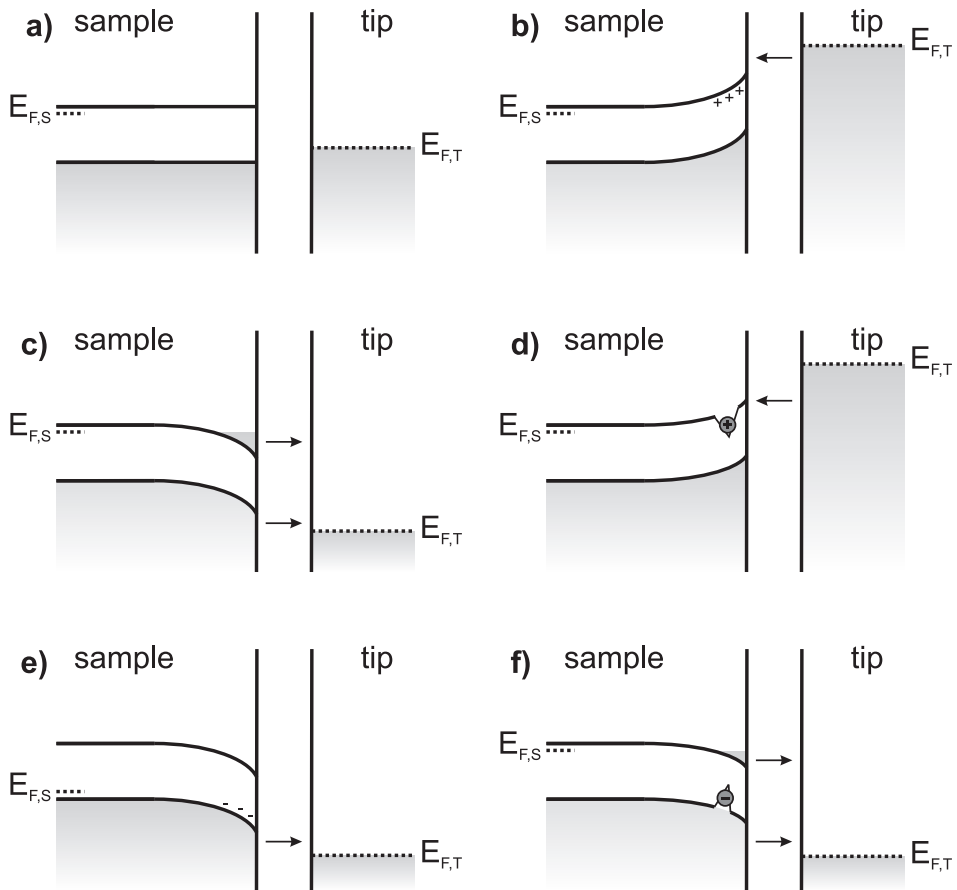
Figure 2.9: TIBB illustrated with energy diagrams of the tip and a semicon-ductor sample. The samples in (a-d, f) are n-type and that in (e) is p-type. (a) Flatband conditions, where the applied bias voltage compensates the TIBB that is present when there is no tip in the neighborhood. (b) Positive TIBB, where bands of the semiconductor are bent upwards and electrons are de-pleted from the conduction band. (c) Negative TIBB, where bands of the semiconductor are bent downwards and electrons accumulate in the conduc-tion band. (d) Similar to (b), but now a nearby donor is ionized that slightly pulls down the bands in its vicinity. (e) Similar to (c), but now for a p-type sample, which results in depleted holes in the valence band and no electron accumulation in the conduction band. (f) Similar to (c), but now a nearby acceptor is occupied that slightly pulls up the bands in its vicinity.
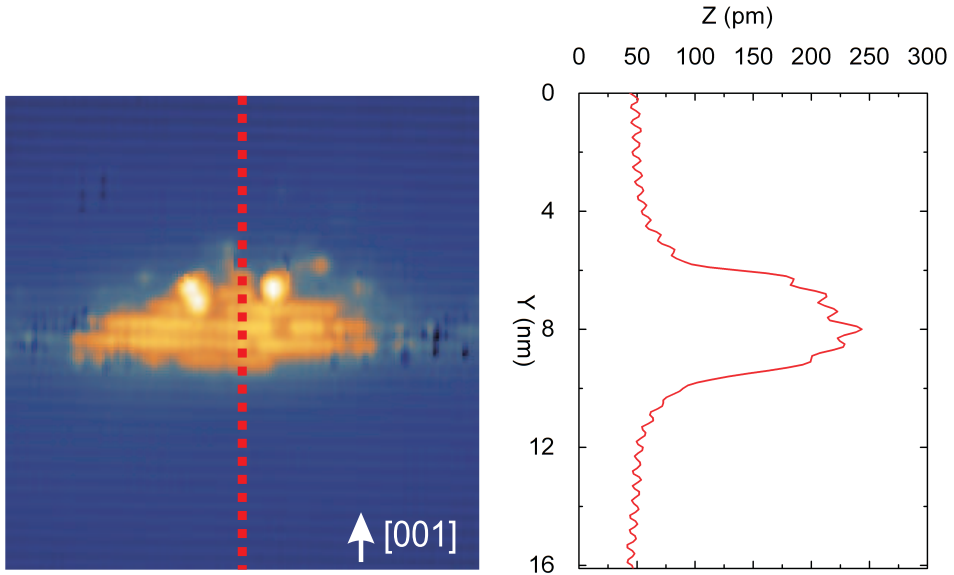
Figure 2.10: (left) GaSb QD in GaAs, 16×16 nm^2, $V = -3.40$ V, $I = 30$ pA. The growth direction is indicated by the white arrow. (right) Height profile taken over the center of the QD, indicated by the dotted red line in the topography image.

in the semiconductor near the tip and the bands bend upwards. When the voltage is below the flatband condition, negative charges accumulate in the semiconductor near the tip and the bands bend downwards. For some cases in Fig. 2.8 a very clear spatial disk appears around the ionized donor. The edge of the disk indicates at which position of the STM tip the donor becomes ionized [69, 16]. When the electron escapes from the donor because of the positive TIBB, the positive ion slightly pulls down the bands, which leads to an enhanced conductivity and therefore a brighter appearance in the STM image. If the TIBB is strong enough, both semiconductor bands become available for tunneling. For example in the case of negative TIBB, when the sample is n–type and the applied bias voltage is high enough, it leads to accumulation of electrons in the conduction band. This gives rise to charge density oscillations in the surface of accumulated free carriers, for instance around dopant atoms, which are also known as Friedel oscillations [15].

X-STM is very well suited for studying semiconductor nanostructures embedded in a host matrix, by exploring the cross-section of cleaved quantum wells (QWs) and quantum dots (QDs). The atomic resolution of STM al-
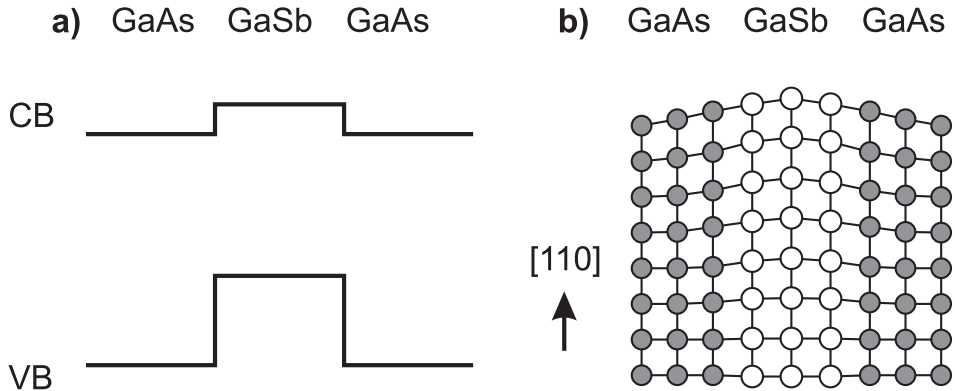
Figure 2.11: (a) Schematic representation of the valence and conduction band alignment of GaAs and GaSb. (b) Visualization of the surface relaxation due to the compressive strain.

lows the composition profiling and structural analysis of the grown structures. In combination with complementary techniques like atom probe tomography (APT) [70] and kinetic Monte Carlo simulations [14], it is possible to obtain full 3D information of nanostructure growth. Self-assembled QDs can for example be grown using the Stranski-Krastanov mode in molecular beam epitaxy (MBE) [6, 7]. Two materials with a slightly different lattice constant are grown epitaxially on each other, which leads to a build up of strain. When a critical thickness is reached, the strain partially relaxes by forming the QDs at random positions.

Semiconductor nanostructures can be visualized with atomic resolution by X–STM. See for example Fig. 2.10, where a GaSb QD in GaAs is imaged and a height profile through the center is displayed. The GaSb appears brighter than the GaAs, an effect which arises both from electronic contrast and local strain. The dimensions and composition of the cleaved QD can be determined from the topography. However, the technique makes a cross–sectional image, which means that we can observe any part of the original QD in the direction perpendicular to the cleaved plane. This is an important consideration when performing statistical analysis on the dot shapes, featured in Chap. 3 and 4 of this thesis.

The electronic contrast at a heterostructure interface originates from the band offsets between the different semiconductor materials, made visible in Fig. 2.11 (a). This leads to a change in the LDOS, resulting in an apparent height change in the X–STM image. The band alignment of GaSb and GaAs is type-II, meaning there is confinement of only one type of charge carrier,

in this case the holes [71]. GaSb has a smaller bandgap than GaAs, with a large valence band offset and a small conduction band offset. When imaging at negative bias voltage, the valence band states contribute the most to the current. Therefore, this tunneling condition results in the largest contrast between the two materials, because of the large valence band offset. However, this effect is most prominent when the bias voltage is close to zero, because the tunneling occurs primarily close to the Fermi energy of the tip and the tunneling probability falls off exponentially for the tip states with a lower energy. In the case of the QD shown in Fig. 2.10, the negative applied voltage is large and we expect the electronic effect to be negligible [12].

During growth of lattice–mismatched heterostructures, compressive or tensile strain is induced. After cleaving such a sample for X–STM, the strain relaxes perpendicular to the surface. In Fig. 2.11 (b) the compressive strain relaxation for GaSb in GaAs is illustrated. The lateral strain is observed directly in the topography image, by comparing the spacing between different rows of the two materials with each other. The perpendicular strain is visible through analysis of the height profile. See for example Fig. 2.10 where the maximum contrast difference represents around 200 pm, which at this applied bias voltage we attribute primarily to strain.

2.7 IV-Spectroscopy

With an STM it is possible to obtain additional electronic information of the sample surface by taking local IV–spectra, otherwise known as scanning tunneling spectroscopy (STS). For each point during the STM topography measurement, an IV–curve can be taken by interrupting the feedback loop and scanning the bias voltage over the preset range. A typical IV–spectrum on GaAs is displayed in Fig. 2.12. The resulting current signal is recorded and gives information about the local electronic properties of the material. Calculating the differential conductivity dI/dV from Eq. 2.2 results in [31]:

$$\frac{dI}{dV}(V) \propto \rho_S(E_{F,S} + eV)\exp(-2\kappa d). \tag{2.7}$$

This shows that the dI/dV is directly proportional to the LDOS of the material at that specific bias voltage.

In the experiments, a single IV–curve typically takes around 1 s, which limits the size of a spectroscopic image to roughly 250×250 pixel^2 due to the cryogenic hold time of the system. The energy resolution in the LT–STM system is in the order of $\Delta E = 50$ meV in the case of $T = 5$ K. From a $dI/dV(X, Y, V)$ dataset, the LDOS can be presented in several ways. A
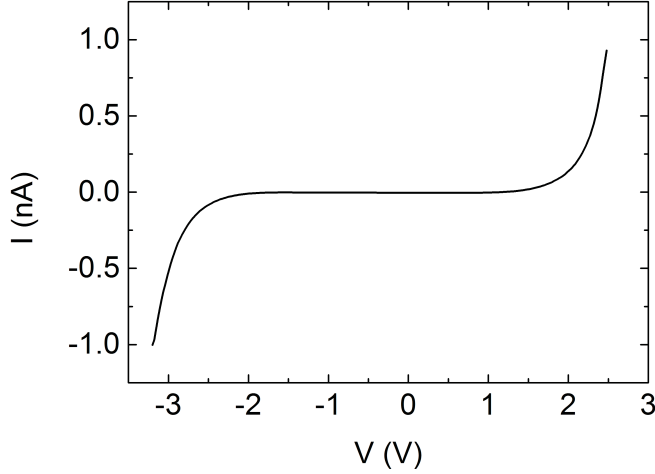
Figure 2.12: A typical *IV*-spectrum on GaAs, $I = 1000$ pA, $V_{min} = -3.20$ V, $V_{max} = +2.50$ V, 34 mV steps.

$dI/dV(V)\,|_{(X,Y)}$ spectrum taken at a single spatial position (X, Y) is useful in for example estimating the bandgap of a semiconductor. This is done by plotting the differential conductivity on a semi–logarithmic scale and determining the intersection of the valence and conduction band with the STM noise level. However, this method should be applied with great care and should be compared to a known bandgap material in the neighborhood to check its validity. It is most reliable when the TIBB is limited, i.e. for high doping concentration materials. A $dI/dV(X, V)\,|_Y$ spectrum taken at several points over a line X, where the LDOS is color coded, can visualize the band offsets between different materials over an interface. A 2D $dI/dV(X, Y)\,|_V$ map of the surface at a given bias voltage gives information about the spatial distribution of the LDOS for that energy and can therefore for example facilitate wavefunction imaging of quantum systems [72, 73]. This technique is applied in Chap. 3.

Numerical derivation of *IV*–spectra often leads to a reduced lateral resolution in 2D dI/dV maps, due to noise and numerical artifacts. To improve this, our LT–STM is combined with an Amatek 5210 Dual Phase lock–in amplifier, to map the $dI/dV(X, Y)\,|_V$ of a surface for a fixed bias voltage. For this purpose, a small AC modulation voltage V_{ref} is added to the DC bias voltage of the STM. The resulting modulation in the tunneling current after conversion by the *IV*-convertor V_{cur} is recorded by the lock–in amplifier. The two input signals for the lock–in can be expressed as $V_{ref} = V_{osc}\cos(f_{osc}t + \phi_{osc})$ and $V_{cur} = V_{sig}\cos(f_{sig}t + \phi_{sig})$, in which V_{osc} and V_{sig} are amplitudes, f_{osc}

and f_{sig} are frequencies, ϕ_{osc} and ϕ_{sig} are phases of the signals and t time. V_{ref} and V_{cur} are then multiplied and integrated over a time τ_{out} to obtain a phase–sensitive output signal. This signal V_{out} is passed through a bandpass filter, which results in a signal only at the modulation frequency f_{osc} with a phase term:

$$V_{out} = V_{osc}V_{sig}\cos(\phi_{osc} - \phi_{sig}). \tag{2.8}$$

If this is Taylor expanded the first order term is:

$$V_{out} \propto V_{osc}V_{sig}\frac{dI}{dV}(V). \tag{2.9}$$

The lock–in output is directly proportional to the dI/dV, which represents the LDOS analogous to Eq. 2.7, but with a greatly improved signal–to–noise ratio. This technique is applied in Chap. 8.

2.8 Spin–Polarized Scanning Tunneling Microscopy

When magnetically sensitive tips are used for tunneling, SP-STM is possible [22]. This technique allows the mapping of magnetism of surfaces and nanostructures down to the atomic scale [74, 75]. In Chap. 8, antiferromagnetic Cr tips are employed together with the lock–in technique to image MnAs nanoclusters in GaAs. The tips are prepared using electrochemical etching, starting from Cr rods in similar fashion to Ref. [76] and [77] and to Sec. 2.2. In this case, the dI/dV from Eq. 2.7 contains an additional magnetic term and can be described by adding the inner product of the magnetization vectors $\mathbf{m_T}$ of the tip and $\mathbf{m_S}$ of the sample [78]:

$$\frac{dI}{dV}(V) \propto \alpha\rho_T\rho_S + \beta\mathbf{m_T} \cdot \mathbf{m_S}, \tag{2.10}$$

where α and β are proportionality factors that depend on the voltage. This shows that not only the strength, but also the direction of the magnetization determines the magnetic LDOS in a SP-STM experiment, which enables the observation of different magnetic domains in a material.

GaSb/GaAs Quantum Dots: Formation and Demolition

In this chapter, the shape and composition of GaSb quantum dots (QDs) in GaAs are investigated with cross-sectional scanning tunneling microscopy (X-STM). The nanostructures are grown epitaxially using molecular beam epitaxy (MBE). The morphology of QDs is strongly influenced by the growth parameters during the application of GaAs capping layers, as visible in X-STM results. The relaxation of high local strain fields around a GaSb QD often involves disintegration of the nanostructure and occurs through Sb segregation in the growth direction and lateral diffusion, leaving behind a ring-like or fragmented nanostructure. Additionally, in some cases structural dislocations are observed around the QDs. In the final part of this chapter, GaSb QDs are investigated in detail by comparing the X-STM results to that of other techniques. $\mathbf{k} \cdot \mathbf{p}$ *calculations predict a significant influence of the QD shape on the hole localization energy. The 3D structure of GaSb QDs is revealed using atom probe tomography (APT). Photoluminescence (PL) measurements show discrete hole charging of quantum rings and confirm the type-II band structure of GaSb in GaAs. IV-spectroscopy performed in the STM is able to resolve several confined hole energy levels near the valence band of a nanostructure and maps out the associated wavefunctions.*

3.1 Introduction

Self–assembled QDs are intensively studied for their unique opto–electronic properties. GaSb/GaAs QDs have a type–II, staggered band alignment, in which holes are confined and electrons repelled from the QD region, resulting in a low recombination rate. Fast carrier capture and long charge storage capabilities of type–II QDs suggest their potential application in memory devices [19, 20]. Recent studies have shown that the use of a 2D electron [79, 80] or hole [81, 82] gas in combination with QDs allows writing and reading information, demonstrating the basic operations required in memory devices.

In the current work, we present an atomically resolved X–STM study of GaSb/GaAs QDs grown by MBE. Previous X–STM studies have shown the structural properties of these QDs grown by metal–organic chemical vapor deposition [83] and droplet epitaxy [84], the principles behind ring formation [85] and the spectroscopic features of these QDs [86]. However, the dependence of the QD morphology on the growth parameters was never investigated. For memory applications, which generally require long storage times, the QDs should have a large hole localization energy. This property depends strongly on the shape and composition of the nanostructure [87], thereby making detailed knowledge of the morphology important for future applications of these QDs.

The samples studied here consist of multiple layers of GaSb nanostructures embedded in GaAs, grown by MBE on an [001] oriented substrate, with a QD density $\sim 5 \times 10^{10}$ cm^{-2}. The samples were provided by R. J. Young from Lancaster University. The QD layers were grown on a GaAs buffer layer, after which 2 monolayers of GaSb were deposited, followed by a thin, 4-16 nm, GaAs first cap layer. After a growth interrupt of 4 minutes under As flux, the GaAs second cap layer was grown at a temperature ~ 100 °C higher than the first cap layer. The overall growth temperatures ranged between 370-580 °C and the V/III ratio during growth was kept constant at 5. Various samples were investigated to study the influence of the GaAs first cap thickness and the GaAs first and second cap temperatures on the morphology of the QDs.

All X–STM measurements were performed in an Omicron STM1 with a TS–2 scanner, under ultra–high vacuum (UHV) conditions, $p \leq 6 \times 10^{-11}$ mbar, at room–temperature. Electrochemically etched W tips were used that were heated and Ar sputtered in UHV for improved stability. The STM was operated in constant current mode to scan cleaved cross-sectional {110} surfaces. Applied bias voltages ranged between $V = -2.5$ and -4.0 V and tunneling currents between $I = 25$ and 50 pA.
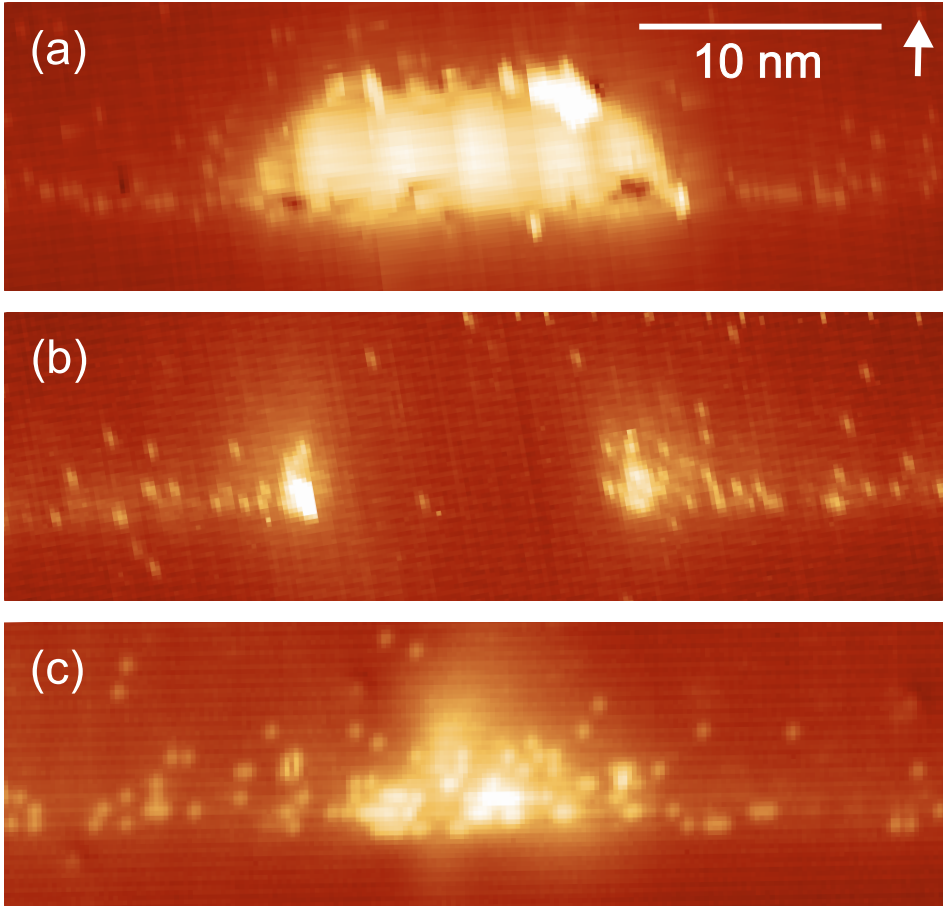
Figure 3.1: Filled state X–STM images of various observed GaSb/GaAs nanostructures. Typical examples of (a) a dot, (b) a centrally cleaved ring and (c) a cluster. $V = -3.20$ V, $I = 25$ pA. The growth direction is indicated by the arrow.

3.2   Morphology

The QDs were grown epitaxially in the Stranski–Krastanov mode. For GaSb on GaAs, the lattice mismatch is 8 % and the strain energy of a Ga–Sb pair 1.87 eV, which is larger compared to standard InAs/GaAs QDs where these are 7 % and 1.40 eV for an In–As pair [85, 88]. In the active region of this material, various nanostructures are created during the growth process, see Fig. 3.1 (a–c). We observe three types of nanostructures: dots, rings and clusters. Dots have the approximate shape of a truncated pyramid, with a nearly pure Sb content. The intermixing between As and Sb is substantially less than was found between In and As in InAs/GaAs QDs [89, 90]. Rings show up as two lobes of a cleaved torus, with a hole in the center that is almost entirely free of Sb, which is different from InAs/GaAs rings where In material is found inside the ring [88]. Clusters have a strongly inhomogeneous Sb concentration, with widely varying morphologies. For some clusters, pure fragments of GaSb are observed with GaAs areas in between. The large lattice mismatch, high pair energy and little intermixing of Sb and As lead to strong local strain fields around the nanostructures, that are relaxed in different ways leading to various shapes.

In Fig. 3.2 (a) a dot is shown with a screw dislocation nearby, which is shown in more detail in Fig. 3.2 (b). It starts at the top of the dot and is terminated about 15 nm above it. Such structural deformations occur often around dot–shaped nanostructures with a nearly pure Sb content, relaxing the local strain.

Free-standing GaSb QDs can also reduce the strain by evolving into rings when they are capped with GaAs. During the capping process, the local strain is initially enhanced because the QDs become encapsulated by material with a smaller lattice constant [91]. The build–up of strain can then be relaxed by mass transport: Sb is removed from the dot by processes involving lateral diffusion, As/Sb exchange and Sb segregation [85]. Diffusion of Sb occurs at regions with the highest local strain, such as the center of a QD. The instability arises at the position where the equilibrium of the interfacial sur-face tensions between the substrate, the QD and the cap layer are disturbed [91]. As/Sb exchange and Sb diffusion empty those regions of Sb, leading to ring centers with very little intermixing. This in contrast to what is found for InAs/GaAs ring centers, where strain driven diffusion is the main formation process and rings are not completely emptied of In [88].

We argue that the observed clusters can form under similar conditions as the rings, but the exchange and segregation processes are incomplete, see for example Fig. 3.1 (c). Above these structures, we typically observe Sb rich regions. Some clusters contain multiple unstable regions from which the Sb is
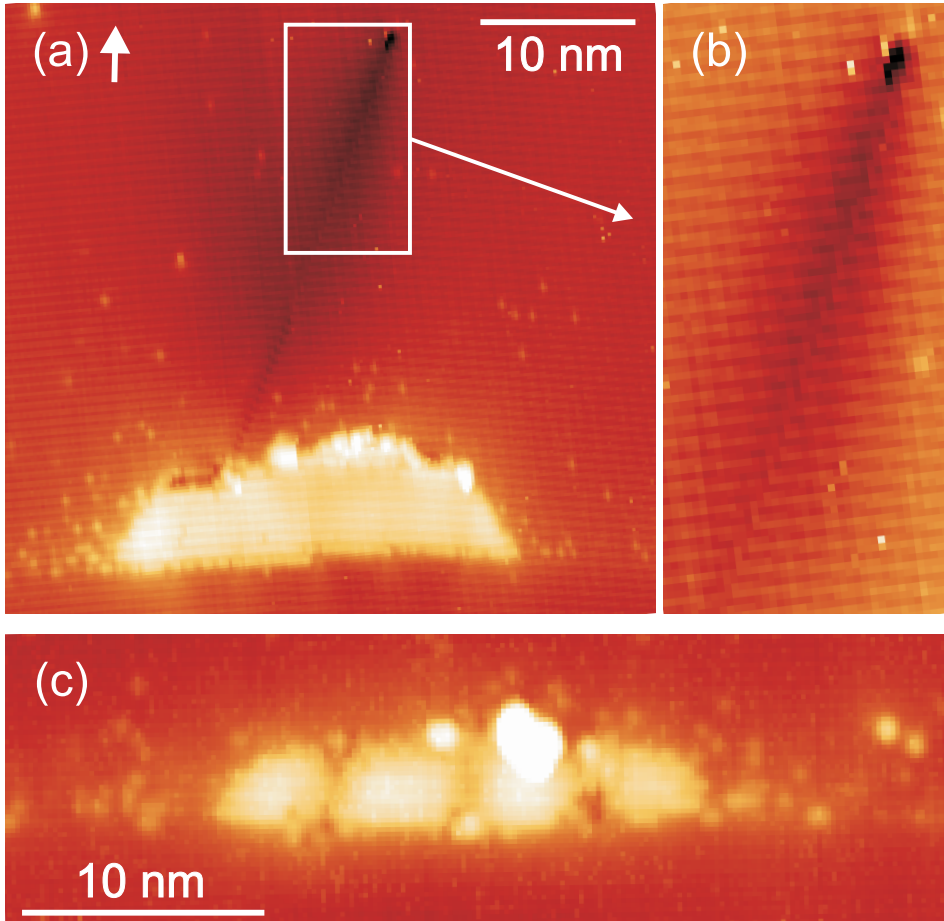
Figure 3.2: Filled state X–STM images of (a) a dot with a screw dislocation on top, $V = -4.00$ V, $I = 30$ pA, (b) a magnified portion of the dislocation revealing the termination at the top and the phase mismatch of the atomic rows at the dislocation boundary and (c) a cluster with multiple segments of GaSb, $V = -3.20$ V, $I = 25$ pA. The growth direction is indicated by the arrow.

removed, see for example Fig. 3.2 (c), in which segments of GaSb are clearly visible with GaAs holes in between. They could be formed under the influence of interfacial misfit dislocations, which occur already at the beginning of the GaSb growth layer where they reduce the strain [92]. The distance between the gaps in these clusters is 5–6 nm, which matches that of misfit dislocations measured on other GaSb/GaAs interfaces [93]. However, with STM we were unable to observe any clear lattice defects around the base of these clusters. The limited occurence of these structures prevented a more detailed study of possible misfit dislocations.

3.3   Growth Statistics

A statistical analysis was performed on four different samples, that were grown with a range of growth parameters. In total, 374 nanostructures were analyzed from the X–STM results and classified. We find that the thickness of the first GaAs cap layer grown directly over the uncapped nanostructures strongly influences the outcome of the growth process: see Fig. 3.3 (a), where the occurrence of various nanostructures is depicted as a function of the thickness of the first cap layer. For sufficiently thick cap layers, i.e. 8 and 16 nm, a dot shape is preserved for 63 % and 46 % of the measured cases respectively. For the 4 nm cap layer, the formation of rings is favored and only 9 % of the dots survive. In this case, the uncapped QDs are not completely overgrown with the first cap layer, exposing them to the higher growth temperature of the second cap layer. The higher energy that is available for mass transport driven by diffusion, As/Sb exchange and Sb segregation leads to more rings and fewer dots. The occurrence of clusters is not influenced significantly by variation of the growth conditions; they are always present in a concentration of about 25–50 %.

The growth temperatures of the first and second cap layers were both varied, but only the second cap temperature showed a significant effect, which is shown in Fig. 3.3 (b). In this case, all the QD layers were grown with a first cap thickness of 8 nm or higher, excluding the influence of partially uncapped QDs. For second cap temperatures in the range of $T = 480\text{–}530$ °C, dots are the predominant shape. For an second cap temperature of $T = 580$ °C, rings are favored. This supports the view that rings form during the capping process, when there is enough energy available to enable mass transport. These results confirm previous studies performed by atomic force microscopy (AFM), where measurements on uncapped GaSb/GaAs nanostructures show only dots with no indication of holes in the center or other forms of dot demolition [94, 87].
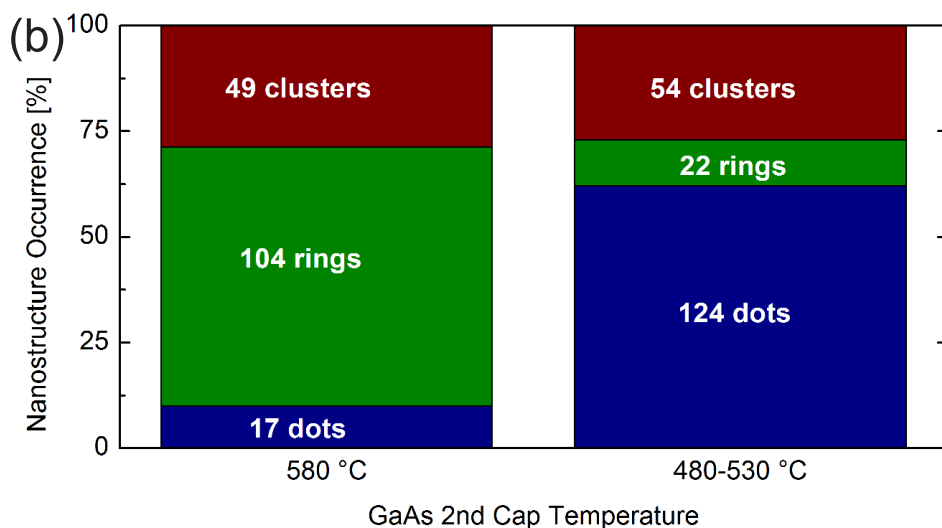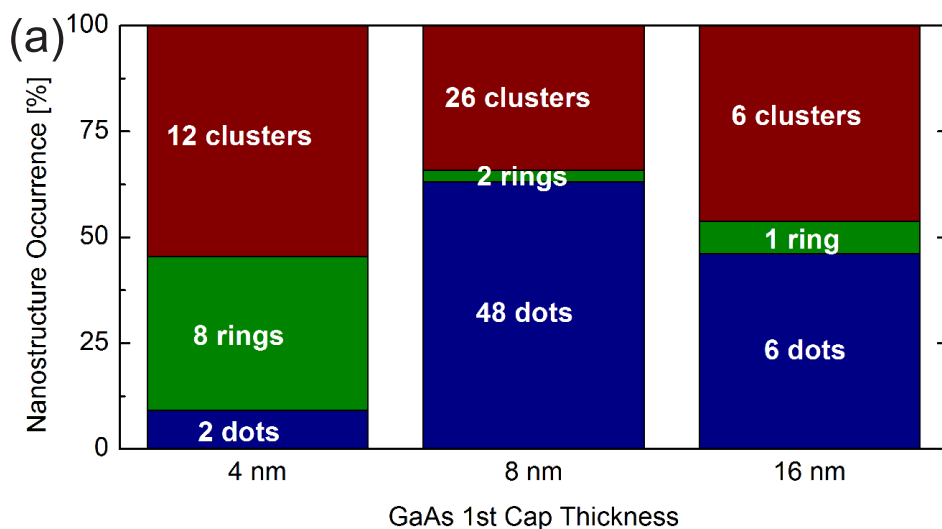
Figure 3.3: Relative occurrence of dots (blue), rings (green) and clusters (red) grown with a range of growth conditions. The observed amounts of each type are indicated in the figure. (a) Various GaAs first cap thicknesses, where first and second cap temperatures always were $T = 430$ and $530\,°C$ respectively. (b) Various GaAs second cap temperatures, where the first cap thickness always was ≥ 8 nm.
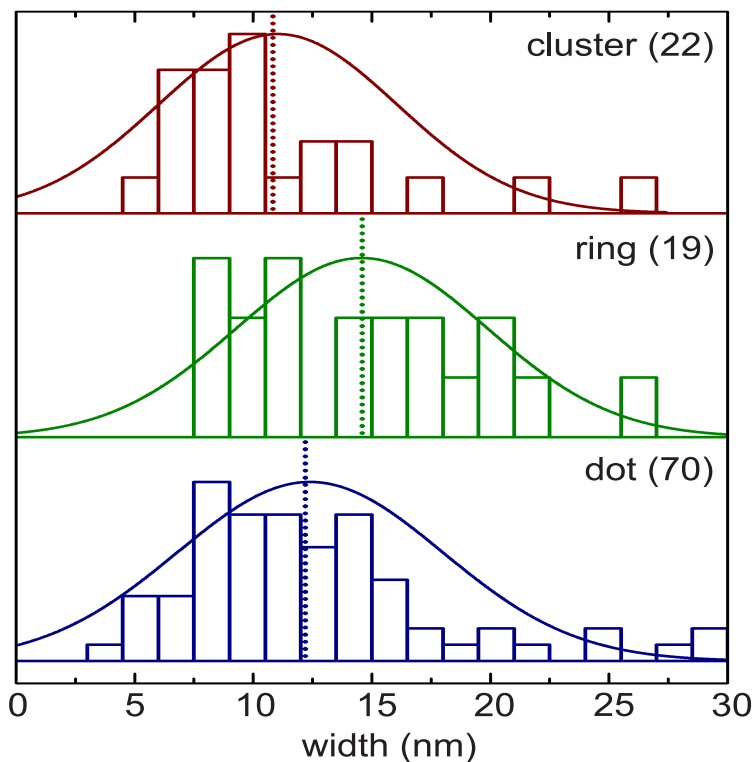
Figure 3.4: Nanostructure width distributions (histograms) and Gaussian fits (lines) of dots (blue), rings (green) and clusters (red). Dashed lines indicate the peak position of the distributions. Rings are on average about 20 % wider than dots and clusters.

For 112 nanostructures grown under similar growth conditions, the base width was determined, see Fig. 3.4. Because the X–STM measurements are restricted to the cleavage plane, different cross–sections of the dots, rings and clusters are imaged. This means that the width distributions are convolutions of the actual size of the nanostructures and the position of cleavage. However, the maxima of the fitted Gaussian distributions are a reasonable measure for comparing the sizes of the different nanostructures. Clusters and dots are on average 20 % smaller in width than rings. We suggest that ring formation is mostly favored in the presence of a large strain field. Smaller uncapped QDs remain dots often decorated with threading dislocations or evolve into clusters during the capping process. Some clusters could have formed around interfacial misfit dislocations that are already present before the overgrowth.
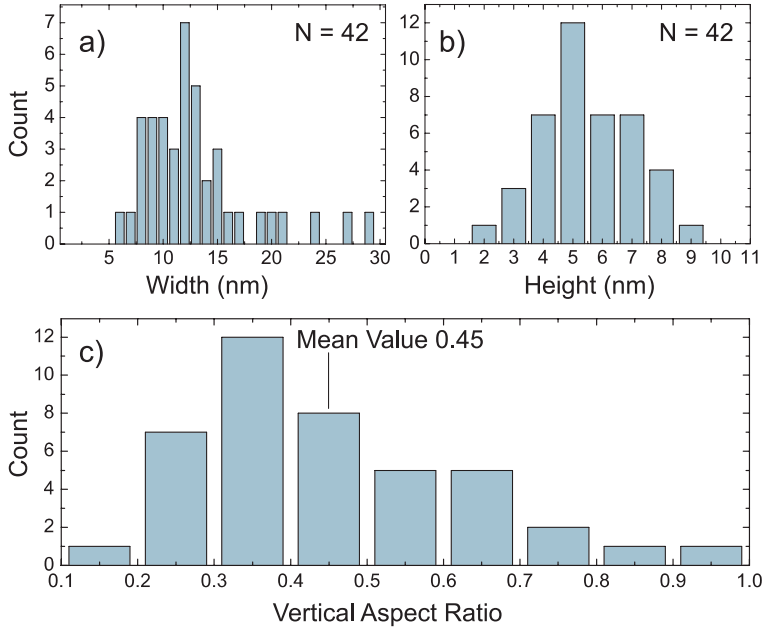
Figure 3.5: Shape statistics from X–STM measurements on 42 pure intact QDs. (a) Width histogram. (b) Height histogram. (c) Vertical aspect ratio distribution.

3.4 Hole Localization Energy

As a first approximation, because GaSb and GaAs have the same group III element, the conduction band offset between the two materials is expected to be small. Therefore, the difference in bandgap energy results primarily in a valence band offset. The effect of strain alters the local band structure and results in an increase of the GaSb conduction band [95]. Therefore, the two materials form a type–II band alignment that favors hole confinement and repels electrons. The hole localization energy, or the ground state of holes trapped in the valence band of the GaSb/GaAs QD, was measured using deep–level transient spectroscopy (DLTS) by T. Nowozin at the Technical University of Berlin, which yielded $E_0 = 0.61$ eV. To compare this value with a theoretical model, they performed eight–band $\mathbf{k} \cdot \mathbf{p}$ envelope function calculations that take into account the real 3D morphology and resulting strain with the associated piezoelectric fields, as outlined in Ref. [96]. X–STM measurements served as an input for the calculations, providing the geometry, sizes and composition of the QDs.

The shape statistics on GaSb QDs from X–STM measurements were extracted from the samples described in Sec. 3.1, with a first cap layer of 8 nm deposited at $T = 460$ °C and a second cap layer at $T = 480$-500 °C. Only pure intact dots are considered in this analysis, that show very little intermixing and have a Sb content of nearly ~ 100 %. Their width and height are depicted in Fig. 3.5. For these nanostructures, the width is 11 ± 6 nm and the height is 5 ± 3 nm. This results in a vertical aspect ratio for most nanostructures of ≤ 0.50. However, as indicated in Sec. 3.3, the width is underestimated because of the cross-sectional technique. Therefore, on average the vertical aspect ratio is expected to be even lower.

The results of the $\mathbf{k} \cdot \mathbf{p}$ calculations of QD size variation are shown in Fig. 3.6 (a). Using X–STM measurements as input, a truncated pyramidal shape is taken to be the base shape for the calculations. The QD height is varied between 1.4-6.3 nm, with a fixed vertical aspect ratio of 0.20. The latter value takes into account and compensates for the width underestimation of the X–STM results. The size variation of pure GaSb nanostructures results in hole localization energies ranging from $E_0 = 0.49$-0.69 eV, where the low value corresponds to the smallest QD and the high value to the largest QD. For alloyed nanostructures, the energies are roughly 0.10 eV lower, which results from the smaller valence band offset when there is intermixing with GaAs.

To study the effect of shape on the hole localization energy with $\mathbf{k} \cdot \mathbf{p}$ calculations, the vertical aspect ratio is varied between 0.05-0.42. The results are shown in Fig. 3.6 (b). In these calculations, the volume is kept constant to avoid the influence of size. The effect on the hole localization energy is smaller than in (a) and varies from $E_0 = 0.60$-0.66 eV in the case of pure QDs and $E_0 = 0.45$-0.55 eV for nanostructures with 50 % GaSb. The change in hole localization energy for a varying QD shape originates primarily in strain effects. The strain distribution is more uniform for high, compact QDs and has a biaxial orientation in the case of flat, stretched out nanostructures, leading to weaker hole confinement in the latter situation.

Taking the average height from X–STM, a pure GaSb content and a vertical aspect ratio of 0.20, the hole localization energy is $E_0 = 0.65 \pm 0.04$ eV, which is in good agreement with the experimental value found in DLTS.

3.5   3D Structure

Although STM has a superior lateral and height resolution, the structural analysis of nanostructures is limited to the 2D plane. A technique to investigate 3D structures on the nanoscale is APT, which can be used complementary
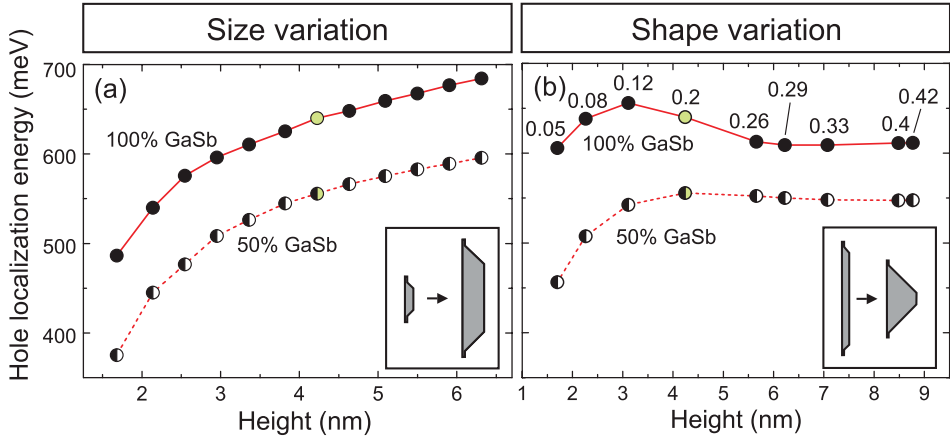
Figure 3.6: The calculated effect on the hole localization energy of (a) QD size and (b) QD shape, for which the height is varied keeping a constant volume. In (b), for each dot the vertical aspect ratio is indicated. The green dots in (a) and (b) represent calculations using the same starting parameters. Calculated by T. Nowozin at the Technical University of Berlin.

with X-STM on semiconductors [70]. To compare X-STM and APT for this work, GaSb QDs were grown by MBE by A. J. Martin at the University of Michigan. Five QD layers were grown at $T = 460 \,°C$, as measured by an optical pyrometer, to deposit 2.3 ML of GaSb at a rate of 0.3 ML/s with a V/III ratio of 2, capped by a 50 nm GaAs layer. The APT technique requires a tip-shaped sample, which is in this case prepared using focused ion beam lift-out [97] and subsequent annular milling to obtain a tip apex of roughly 100 nm. The APT was conducted by E. A. Marquis at the University of Michigan in a Cameca LEAP 4000X, which was operated in voltage pulsing mode with a 15% pulse fraction at a temperature between $T = 20\text{-}33$ K. During analysis, reconstruction parameters were selected to obtain flat GaSb layers and to match the MBE grown layer thicknesses.

Various GaSb nanostructures are depicted in Fig. 3.7 as measured by X-STM. In (a) an intact, compact QD is visible with a truncated pyramidal shape. Cross-sections of disintegrated nanostructures are shown in (b-e), with varying morphologies. Those of (b) and (d) appear as ring-like nanostructures with a center emptied of GaSb. In (c) and (e) clusters of GaSb are present, where multiple segments remain after overgrowth with GaAs. These nanostructures appear very similar to the ones described in Sec. 3.2.

The compositional structures of GaSb QDs imaged by APT are shown
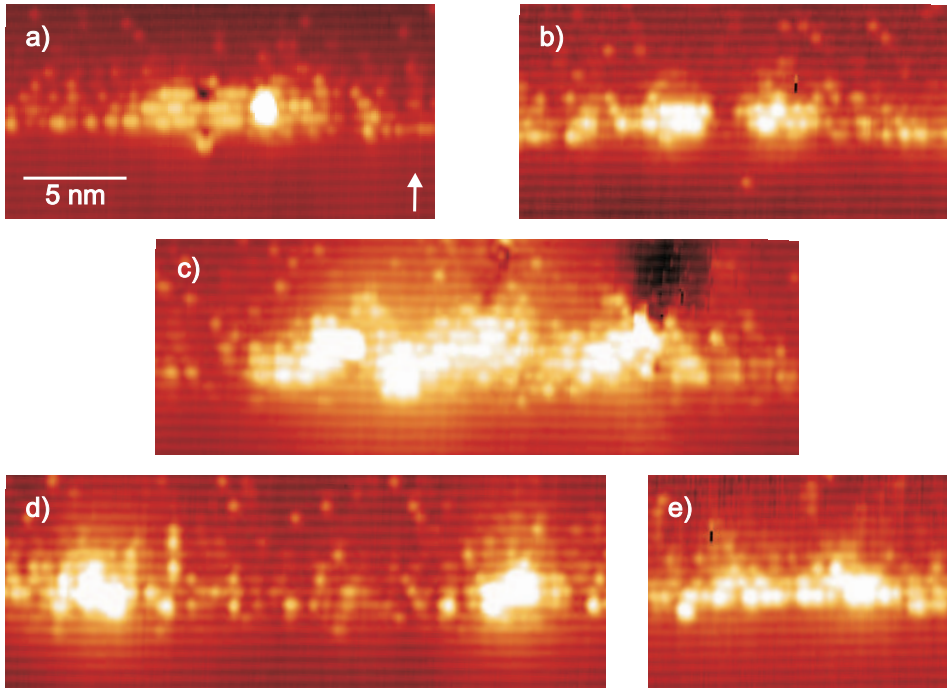
Figure 3.7: X-STM images of GaSb nanostructures in GaAs, showing (a) a pure intact QD and (b-e) various ring-like clusters of smaller islands, $V = -2.80$ V, $I = 100$ pA. The arrow indicates the growth direction.
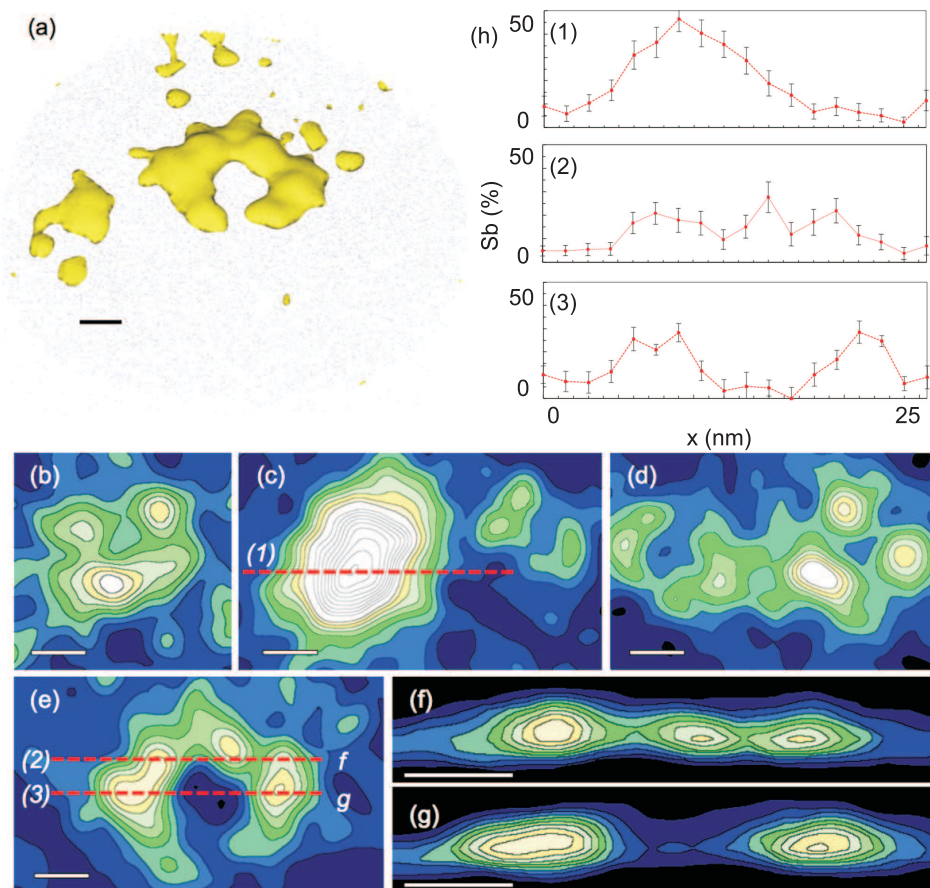
Figure 3.8: (a) An iso–concentration area of 9 % Sb atoms in a 3D APT volume. (b–e) 2D Top–view cross–sectional contour plots, where darker and lighter contrast corresponds to lower and higher concentration of Sb respectively. All plots have the same concentration scale. The scale bars represent 5 nm. The white with black contour lines in (c) represent higher concentrations. (f–g) 1D cross–sectional views along the red lines indicated in (e). (h) Line profiles of the Sb concentration along the red lines (1–3) indicated in (c) and (e). Measured by E. A. Marquis at the University of Michigan.

in Fig. 3.8. The nanostructure shapes match with those visible in X–STM measurements. The yellow iso–concentration area of 9 % Sb in (a) shows the 3D extent of two nanostructures. To further analyze the composition, top–view contour plots are made from the APT data set by taking cross–sections through the center of the nanostructures. For this, iso–concentration surfaces are extracted and mapped to the 2D slices. In the analysis, the voxel size is $0.5 \times 0.5 \times 0.5$ nm^3 and the delocalization distance is 3 nm. The concentration scale is the same for all the contour plots. It is depicted using a dark–blue–green–yellow–white color scale, representing a low to high concentration scale. For the compact QD in (c), the highest concentrations are displayed in white, with black contour lines separating the scale. Over the lines in (c) and (e), 1D profiles are obtained and displayed in (1–3). For a quantitative analysis, cylinders with a diameter of 1.5 nm are used to extract values for the concentration of Sb. In (f–g) cross–sectional contour plots are shown over the lines indicated in (e), which are compared to the X–STM results.

From the APT results, it is clear that 3D information is important for understanding the complete shape of the GaSb QDs. In the samples studied, about one third of the nanostructures consist out of pure intact QDs, visible in for example Fig. 3.8 (c) and comparable to Fig. 3.7 (a). The remaining majority of nanostructures are build up out of clusters of a few small GaSb islands, that in most cases form ring–like structures, see Fig. 3.8 (b, d–e). Note that in (d) two clusters are displayed. There is variation in the size and shape of the islands, as well as in the Sb concentration between them. However, the lowest Sb concentration is consistently found in the center between the islands.

These results suggests that there is a whole spectrum of disintegrated QD shapes. The QDs vary from shapes where primarily the center of the original truncated pyramid is removed to structures that show even more disintegration and where only small segments are left behind after capping. The cross–sections in Fig. 3.8 (f–g) also show the limitation of X–STM compared to APT: by choosing a slightly displaced cross-sectional slice of material, a totally different 2D morphology is obtained. Compare for example Fig. 3.8 (f) with Fig. 3.7 (e) and compare Fig. 3.8 (g) with Fig. 3.7 (c). However, as discussed in Sec. 3.3, the growth parameters during capping have a big impact on the morphology, and we can not determine whether the shapes observed for those samples have a similar distribution as in this sample. In all samples, the distinction between rings and clusters is probably not clear cut and a whole spectrum of disintegrated QD shapes exists.

APT is a very powerful method to determine 3D compositions and shapes

of semiconductor nanostructures. The atomic resolution, strain imaging and the ability to gather more statistics are strengths of X–STM. Both techniques together enable the study of QD morphology in detail and provide more information than a single method alone.

3.6   Optical and Electronic Properties

Due to the type–II band structure of GaSb in GaAs, the holes are confined and the electrons repelled from the QDs. This results in poor optical quality, because recombination is less likely to occur. Moreover, in optical experiments Coulomb repulsion in the QDs is expected to play an important role, because of the close proximity of charge carriers that are of the same type. For this work, the optical and electronic properties of GaSb QDs are investigated in more detail to provide insight in the carrier confinement in these nanostructures.

To probe the optical properties of GaSb QDs, PL measurements were conducted by R. J. Young at Lancaster University. A single QD nanostructure layer was MBE grown at $T = 490\ ^\circ$C, capped with 5 nm of GaAs at $T = 430\ ^\circ$C and subsequently overgrown with 245 nm GaAs at $T = 580\ ^\circ$C. The X–STM results from Sec. 3.3 showed that these conditions resulted primarily in the growth of GaSb rings. The PL sample was cooled down to $T = 1.4$ K in a LHe cryostat and excited with a 532 nm continuous wave laser via an optical fiber. The PL was collected from an area of 2 mm^2 with another fiber and guided to a Peltier-cooled InGaAs detector.

A typical PL spectrum is displayed in Fig. 3.9 (a). The main contribution to the observed emission comes from the GaSb nanostructures, which have a peak emission energy of around 1 eV. Furthermore, the peak displays clear oscillations, that were evaluated in more detail by varying the PL excitation power, shown in (b). Increasing the pump intensity over five orders of magnitude resulted in a blueshift of the ring emission of more than 50 meV. This is a characteristic feature of type–II systems and in this case is proposed to be due to discrete hole charging, similar to Ref. [98] and [99]. In (a) the ring peak is fitted with Gaussian subpeaks having a width of 26 meV, while the subpeaks are separated by an average 21 meV. The latter is a measure for the energy needed for adding another hole to the QD. The individual subpeaks show a small blueshift with power, visible in (c). This blueshift is explained by a band bending effect in the material due to the increasing amount of electrons that accumulate around the nanostructures at higher laser powers.

The electronic properties of a GaSb quantum ring are investigated in detail by scanning tunneling spectroscopy (STS), by taking IV-spectra on
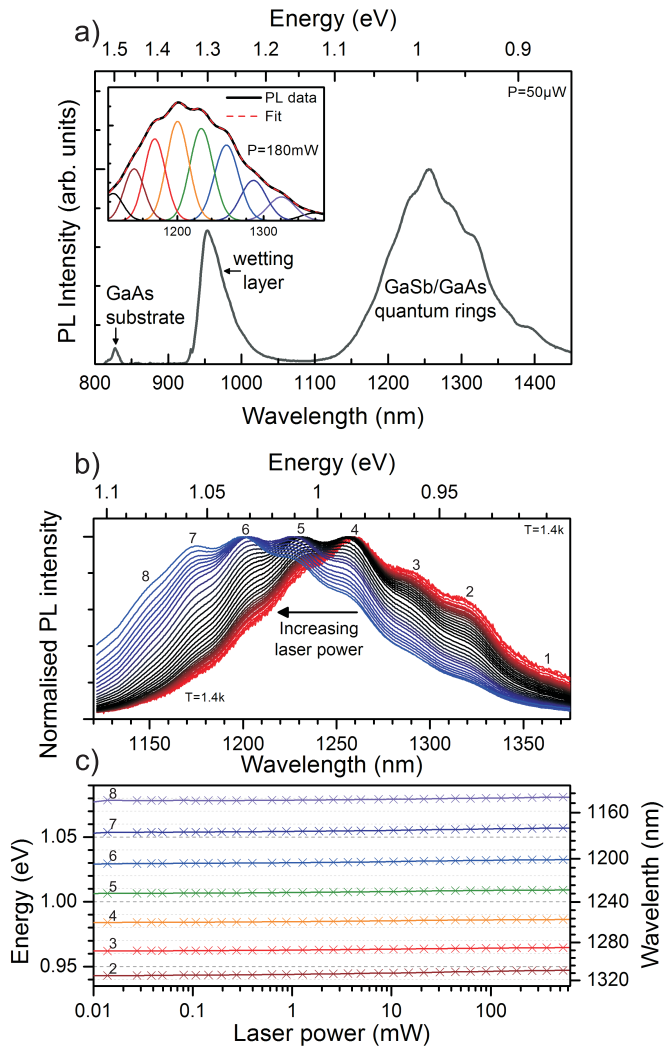
Figure 3.9: (a) PL on a sample containing primarily GaSb quantum rings. The optical spectrum shows a clear peak around 1 eV that is attributed to the quantum ring emission. The discrete hole charging is responsible for the oscillations in the peak. The inset shows a fit with multiple Gaussian sub-peaks of the quantum ring peak under high-power illumination. (b) The quantum ring peak has a strong blue-shift with increasing laser power over five orders of magnitude. (c) The sub-peaks exhibit a weak blue-shift with increasing power. The labels in (b) and (c) represent the individual hole populations. Measured by R. J. Young at Lancaster University.
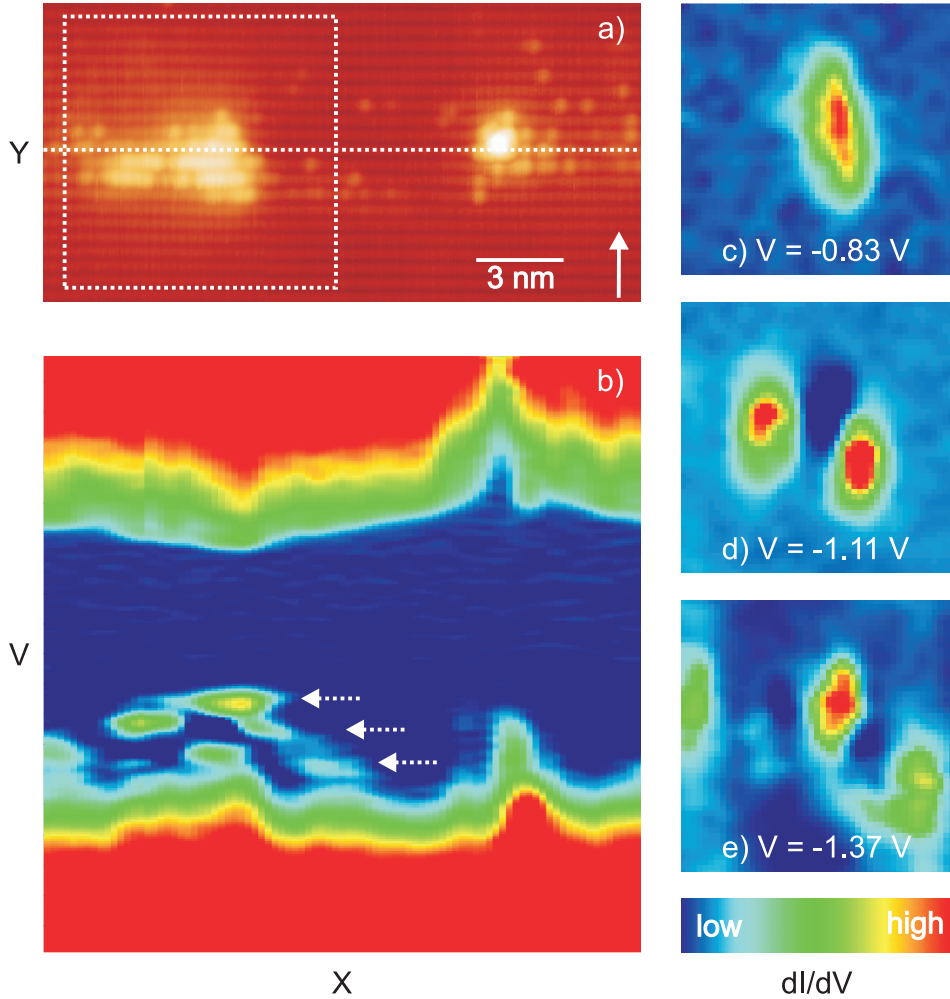
Figure 3.10: (a) Topography of a GaSb quantum ring in GaAs, $V = -3.00$ V, $I = 300$ pA, $T = 77$ K. The arrow indicates the growth direction. (b) Spectroscopy line spectrum, taken over the dotted white line shown in (a), $V_{min} = -3.00$ V, $V_{max} = +2.00$ V, 20 mV steps. (c-e) 2D LDOS maps, in the area of the dotted white rectangle in (a), of the hole wavefunctions at three different bias voltages close to the valence band, indicated by the white arrows in (b).

each point in the topography map, see Fig. 3.10. The STS technique is performed using our low–temperature (LT–)STM operated at $T = 77$ K and is further explained in Sec. 2.7. The dI/dV information is displayed as a color scale representing low (blue) to high (red) local density of states (LDOS). The topography in (a) shows the cross–section of a very irregularly ring–shaped object. As discussed in Sec. 3.5, the actual 3D nanostructure of the ring might be a cluster of small islands. The interruption of the wetting layer between the ring lobes indicates that this was a single nanostructure before capping and the Sb diffused away from the center during overgrowth.

A dI/dV line spectrum is shown in Fig. 3.10 (b), taken over the dotted white line in (a). It shows the band structure parallel to the wetting layer. Surprisingly, the conduction and valence band offsets of the GaSb material are very different on both lobes of the ring. The left side lobe displays an almost flat conduction band with respect to the surrounding GaAs, which comes close to the $\sim +0.10$ eV conduction band offset reported in literature [98]. On top of the right side lobe, an adatom is visible in the topographic image. We suspect that this adatom is charged and is therefore responsible for the different electronic structure observed at that position. Comparing the X–STM observations to the APT results in Sec. 3.5, we propose that this nanostructure is a ring–like cluster of small islands and that variations in the electronic structure arise due to the different composition and size of the islands. Due to quantum size effects, we expect that only larger–sized islands have confined electronic states.

A rich electronic structure is visible in the large island on the left side of the quantum nanostructure, where discrete energy levels can be distinguished. The spatial 2D wavefunctions of these confined electronic states are visualized by plotting the LDOS in real space [72, 73]. The quantum nanostructure wavefunctions are displayed in Fig. 3.10 (c-e), taken from the dotted white square region indicated in (a). The three voltages correspond to three distinct wavefunction shapes. A single localized maximum in the dI/dV is visible at $V = -0.83$ V, which corresponds to the ground state of the confined holes. Two maxima are visible at $V = -1.11$ V and three at $V = -1.37$ V, corresponding to the first and second excited state respectively. A rough estimate of the hole localization energy is made from the dI/dV by estimating the GaSb hole ground state energy with respect to the GaAs valence band, which yields $E_0 = 0.68 \pm 0.05$ eV. This is in good agreement with the values found in the DLTS measurements and $\mathbf{k} \cdot \mathbf{p}$ calculations of Sec. 3.4.

Using a similar approach to Ref. [73], the quantum nanostructure can be described as a harmonic oscillator. The wavefunctions Ψ_n are calculated by:
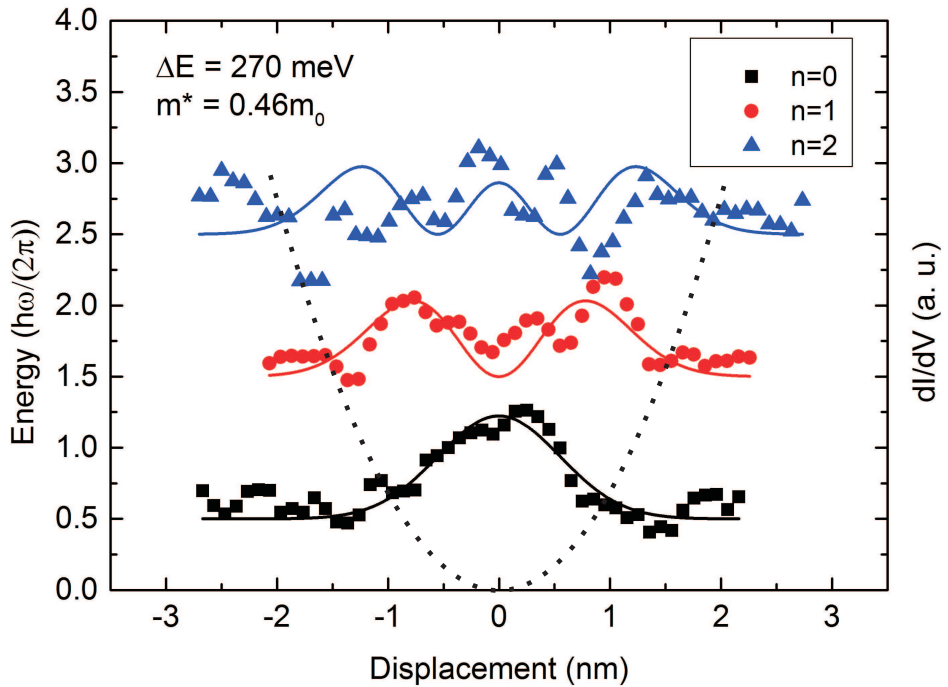
Figure 3.11: dI/dV intensities (dots) taken over horizontal lines in the center of Fig. 3.10 (c-e) fitted with $\mid \Psi_n \mid^2$ (solid lines) from Eq. 3.1. The corresponding harmonic potential is displayed as a dotted black line.

$$\Psi_n = (2^n n! \sqrt{\pi} X_0)^{-1/2} \exp\left(-\frac{1}{2}\left(\frac{x}{X_0}\right)^2\right) H_n\left(\frac{x}{X_0}\right), \qquad (3.1)$$

where n is a non–negative integer indicating the different discrete quantum states and H_n are Hermite polynomials. The characteristic length X_0 is:

$$X_0 = \sqrt{\frac{\hbar}{\omega m_h^*}}, \qquad (3.2)$$

where $\hbar$ is the reduced Planck's constant, ω the harmonic oscillator frequency and m_h^* the hole effective mass. The eigenenergies E_n of the system are:

$$E_n = \hbar\omega\left(n + \frac{1}{2}\right) \quad \text{for} \quad n \geq 0. \qquad (3.3)$$

In Fig. 3.11 the distinct states from Fig. 3.10 (c–e) are fitted with Eq. 3.1. The zeroth order harmonic fits well to the data, the first and second order fits are less optimal. In the first order harmonic there is a small third peak coming from the energy-broadened zeroth order, see Fig. 3.10 (b). In the second harmonic the outer two maxima are weak and there is some mixing with the two energy-broadened maxima from the first order. We estimate an error in the fits of 20 % based on these observations. From the global fit we find a characteristic length of $X_0 = 0.8 \pm 0.2$ nm. Together with the average energy difference between the three states $\Delta E = 0.27 \pm 0.05$ eV, this results in an estimation of the hole effective mass of $m_h^* = 0.46 \pm 0.09\ m_0$, with m_0 the free electron rest mass. This value is in the range between that of $m_h^* = 0.5\ m_0$ for GaAs and that of $m_h^* = 0.23\ m_0$ for GaSb [100]. This spectroscopy measurement demonstrates that holes are strongly confined in the GaSb/GaAs nanostructures.

3.7   Conclusion

In summary, GaSb/GaAs QDs give rise to a larger local strain as compared to standard InAs/GaAs QDs. This is due to larger lattice mismatch, higher pair energy and less intermixing. The high local strain can be relaxed by means of dislocations around the dots, ring or cluster formation through Sb segregation or fractioning of the nanostructures into clusters that originate from misfit dislocations at their base. The occurrence of rings and dots strongly depend on the capping layer growth conditions, where the application of higher temperatures favor the formation of rings over dots. The X–STM results provide the input for $\mathbf{k} \cdot \mathbf{p}$ calculations, that result in a hole localization energy of

$E_0 = 0.65 \pm 0.04$ eV, which is in good agreement with DLTS measurements. The APT data of these nanostructures reveal that quantum rings can disintegrate into clusters of small islands. The optical and electronic investigations of GaSb quantum nanostructures demonstrate the strong hole confinement of this material system.

Chapter 4

GaSb/GaAs Quantum Dots: Shape Stabilization

GaSb quantum dots (QDs) in a GaAs matrix are investigated with cross-sectional scanning tunneling microscopy (X-STM) and photoluminescence (PL). The nanostructures are grown with molecular beam epitaxy (MBE) and are capped with Al-rich material aimed to preserve the QD height. Furthermore, structural defects appearing around the nanostructures are investigated in detail with X-STM. These defects occur primarily around the taller, better preserved nanostructures and result in a reduced QD PL emission intensity. Complementary PL measurements on the same samples are discussed and compared to the X-STM results.

4.1 Introduction

It was demonstrated recently that a significant number of GaSb nanostructures grown on GaAs disintegrate under the influence of high local strain fields and Sb segregation in the growth direction during capping with GaAs, for example in Ref. [83], [85] and [94] and in Chap. 3. That is, the strain induced by capping causes lateral out-diffusion of Sb from the QD core [91]. A strategy to prevent disintegration would be to curtail Sb out-diffusion. Al-containing compounds in general have higher bond strengths, and thus lower surface diffusion rates than those containing Ga, while maintaining nominally the same lattice parameter. Therefore, QD height retention should improve with the addition of Al to the capping layer. This material system could be interesting for intermediate band solar cells [101, 102, 103] and flash-memory applications [19, 20]. In the latter case, the QDs are coupled to a 2D hole

gas to obtain very fast read and write times [81, 82]. A large hole localization energy is then crucial for a long storage time. Recently it was shown that the hole localization energy for GaSb/GaAs QDs is increased when Al–rich capping material is used compared to pure GaAs [104]. In this work we present a X–STM and PL study on GaSb QDs in a GaAs matrix grown by MBE, overgrown with with Al-containing III–V capping materials.

All of the QD samples were grown in Stranski-Krastanov mode using MBE on GaAs (100) substrates. The samples were grown by M. DeJarld at the University of Michigan. Each sample had an undoped 500 nm GaAs buffer layer, grown at a rate of 1.0 monolayer (ML)/s. Before QD formation, samples were cooled to $T = 460$ °C, as measured by an optical pyrometer, to deposit 2.3 ML of GaSb at a rate of 0.3 ML/s with a V/III ratio of 2. The resulting QD concentration was approximately 5×10^{10} cm^{-2}. The original uncapped dot height as measured by atomic force microscopy (AFM) was 4 ± 1 nm. Immediately afterward, the capping layer was grown, and four different capping layer compositions were used: 50 nm of GaAs, 1 ML of AlAs with 50 nm of GaAs, 3 ML of AlAs with 50 nm GaAs, and 20 nm Al$_{0.50}$Ga$_{0.50}$As with 30 nm of GaAs. The capping layers were grown at 0.3 ML/s as well, with the exception of the AlGaAs layer which was grown at 0.6 ML/s. All of the material was annealed for 10 minutes at the growth temperature and quenched.

The samples for X–STM contain seven QD layers, one layer with GaAs capping as a reference, and two layers of each other capping material. They were cleaved revealing {110} surfaces under ultra–high vacuum (UHV) conditions in an Omicron LT–STM, operated at a pressure of $p \leq 4 \cdot 10^{-11}$ mbar and a temperature of $T = 77$ K. Electrochemical etching was used on polycrystalline W wire to obtain atomically sharp tips. These tips were subsequently annealed and sputtered with Ar under UHV conditions. The samples for PL each contained ten layers of QDs of a single capping composition. Cooled to $T = 10$ K, they were measured by M. DeJarld at the University of Michigan using a Coherent Mira Ti:Sapph tunable laser at $\lambda = 845$ nm with a spot size of 5 μm. An 850 nm filter was placed in the collection path and emission was collected using an InGaAs detector.

4.2 Al–Rich Capping

Examples of topography images of the GaSb nanostructures are shown in Fig. 4.1. At the chosen tunneling conditions, the STM technique primarily images the filled states of the group V elements. The contrast is thus mainly determined by the local dangling bonds of the chemically different As and Sb
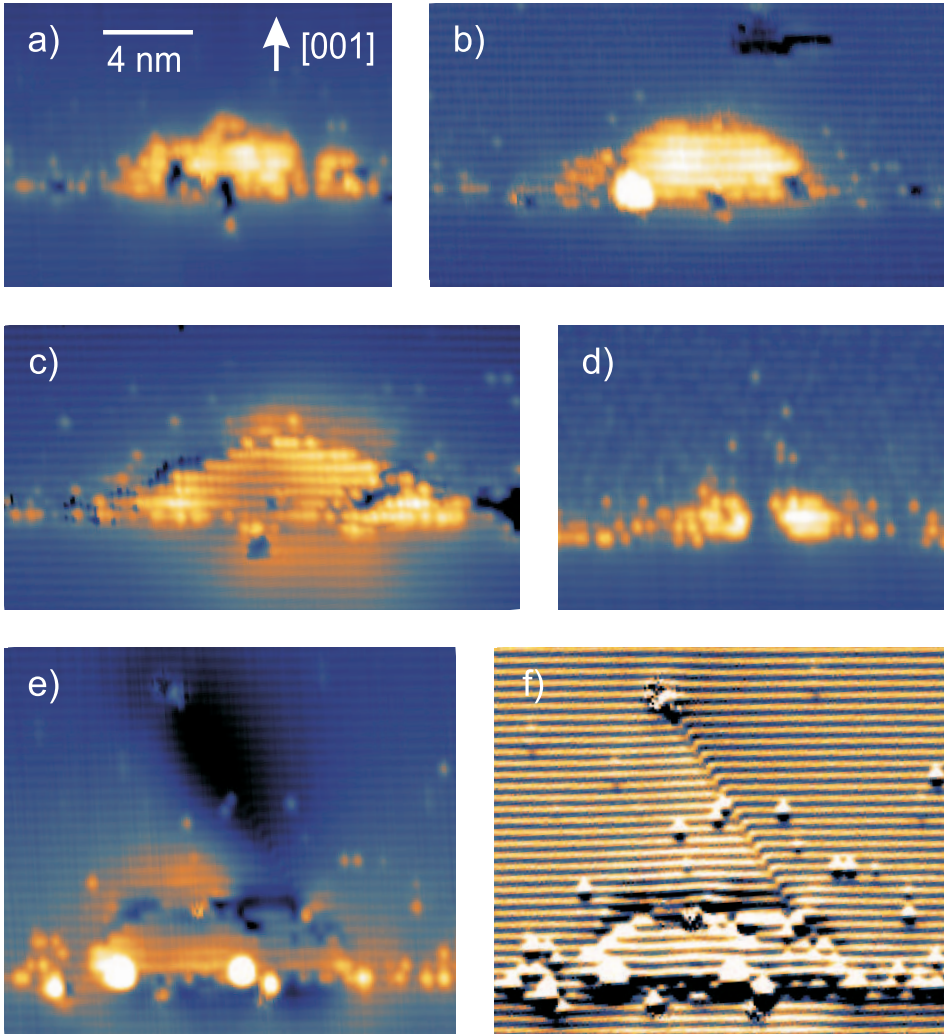
Figure 4.1: STM images taken at $V = -4.00$ V and $I = 250$ pA. Typical examples of GaSb nanostructures grown on GaAs, capped with (a) 50 nm GaAs, (b) 1 ML of AlAs followed by 50 nm GaAs, (c) 3 ML of AlAs followed by 50 nm GaAs and (d) 20 nm of $Al_{0.50}Ga_{0.50}As$ followed by 30 nm of GaAs. Fig. (b–c) represent intact QDs, (a) and (d) are disintegrated nanostructures. (e) Topography and (f) current images of a QD capped with 1 ML AlAs, with a structural defect emanating from the nanostructure.
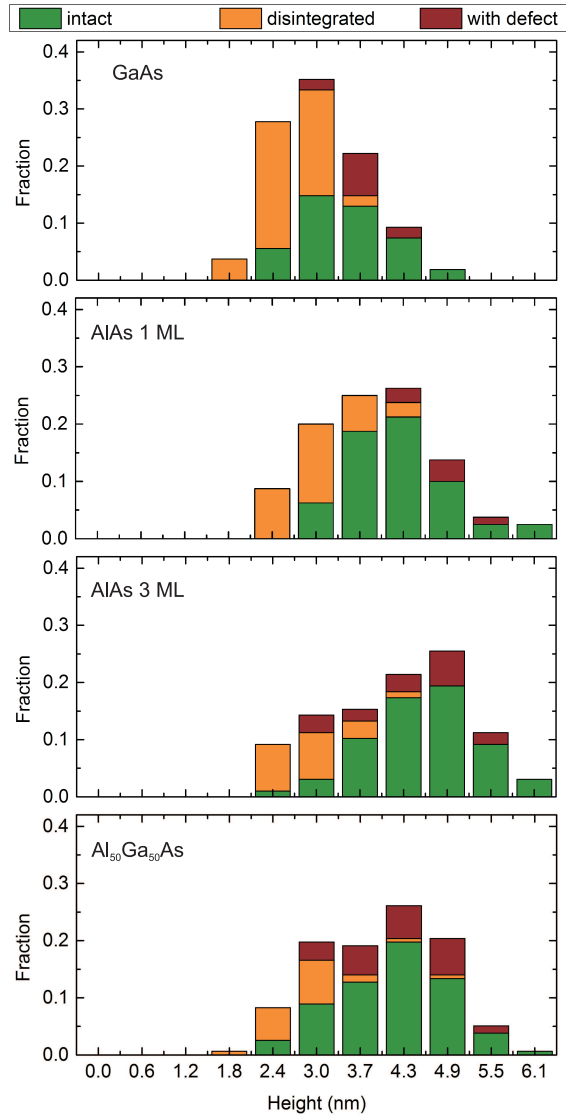
Figure 4.2: Height distributions of the QD nanostructures for the various capping materials. The histograms bin size is chosen to be one lattice constant of GaSb, equal to 0.61 nm.

atoms, which appear darker and brighter respectively. The influence of group III atoms on this contrast is weak due to the fact that they are nearest neighbors to the group V atoms. Furthermore, for surface group V elements only a fraction of the three nearest neighbor Ga atoms are replaced by Al atoms, further reducing the contrast for the Al in the thin capping layer. Unfortunately the sample did not allow stable tunneling at positive bias voltages, which would allow tunneling directly in the empty dangling bonds of the group III atoms. Additionally, the effect of strain is also visible as a bright contrast in the images representing outward relaxation around the QDs. The size and purity of the QD leads to a high build-up of local strain, which is partially relaxed outwards from the surface when the sample is cleaved for X–STM measurements. Because of the high local strain around the QDs, some of the images contain cleaving artifacts, i.e. material that is ripped out or left behind when the sample is cleaved.

For this work we analyzed 389 QDs recorded by X–STM and determined their morphology and size. A substantial part of the imaged nanostructures is very pure and the original uncapped QD height is retained, see for example Fig. 4.1 (b–c). However, quite frequently the QDs are disintegrated and appear as segmented structures, visible in (a), or ring–shaped objects, visible in (d), see also Chap. 3. There is almost no intermixing visible in the GaSb/GaAs QDs, which is clear from the absence of any alloy fluctuations and the pure Sb content visible in our X–STM images. This is different from InAs/GaAs QDs, where intermixing plays a more important role in ameliorating any high local strain that could potentially destabilize the nanostructures [90, 88]. We also observed the appearance of structural defects around the larger, intact QDs, such as those visible in Fig. 4.1 (e–f).

The QD height distributions for the various capping materials are presented in Fig. 4.2. We categorize a nanostructure as disintegrated when at least 10 % of the intact dot shape is affected. We estimate a 10 % error in the statistical analysis, mainly due to the fact we are using a 2D imaging technique to classify 3D nanostructures. Clearly, the Al–rich capping materials have a large effect on the growth, because the average dot height shifts from around 3.1 nm for GaAs capping to around 4.5 nm for the other three Al–rich capping materials, which matches with the original uncapped QD height. Disintegrated QDs are on average much lower, because the GaSb migrates from the top of the nanostructures during growth, leaving behind only a part of the original shape. The height distributions thus reveal that the use of Al–rich capping materials leads to the better preservation of the original dot height after capping. The percentage of retained structures increases from 52 % in the case of GaAs capping to 70 % by capping with 1 ML AlAs. With

3 ML AlAs and AlGaAs capping the height retention is increased to 79 % and 83 % respectively.

4.3   Defects

The data show that including Al in the capping layer does in fact result in higher, less eroded QDs, likely due to the reduction of lateral Sb diffusion during overgrowth. But removing QD height reduction as a mechanism to reduce the strain around the capped nanostructures results in the appearance of another strain relieving mechanism. A side–effect of the dot preservation is that structural defects appear around some of the QDs, primarily around the taller, intact QDs. A structural defect that appears close to a QD is shown in Fig. 4.3 (a–b). Mismatch between atomic rows is visible along two ⟨111⟩ directions that start around the QD and end in a single point in the cross-sectional plane. The area on top of the QD is relaxed inward with respect to the surrounding surface, suggesting tensile strain in that region. Inspection of Fig. 4.2 reveals that the defects are present in 9 % of the structures for 1 ML AlAs, 17 % for 3 ML AlAs and up to 22 % for AlGaAs capping, compared to 11 % for GaAs capping. The data show that they occur especially near the QDs that retain their full height, which means that the Al–rich capping layers contain the most defects.

The structural defects occur because of the large lattice mismatch between the almost pure GaSb QD and the GaAs substrate. We suggest a structural atomic model for this type of defect, which is displayed in Fig. 4.3 (c). This ball and stick model represents the (110) plane imaged by X–STM. The bigger dots are the atoms in the surface layer accessible to the STM. 1 ML below there is another layer of atoms indicated by the smaller dots. In this model we propose that there are several dislocations present at the interface between the GaAs and the GaSb QD. This assumption is consistent with published reports that show that these interfacial misfit dislocations can occur during growth of GaSb QD nanostructures [93, 92]. Due to the misfit dislocations and the high amount of strain, the surrounding GaAs or AlGaAs does not grow in perfect registry with the capping layer directly on top of and in the immediate vicinity of the QD. Thus, the GaAs lattice grown on top of the QD is displaced 1 ML in the [001] direction with respect to the surrounding GaAs matrix, effectively forming a stacking fault [105]. In 3D, the stacking fault forms a displaced {111} plane, which terminates in a defect or when it meets another stacking fault. The latter is the situation displayed in the model and in the observed X–STM images where two stacking faults meet and annihilate.
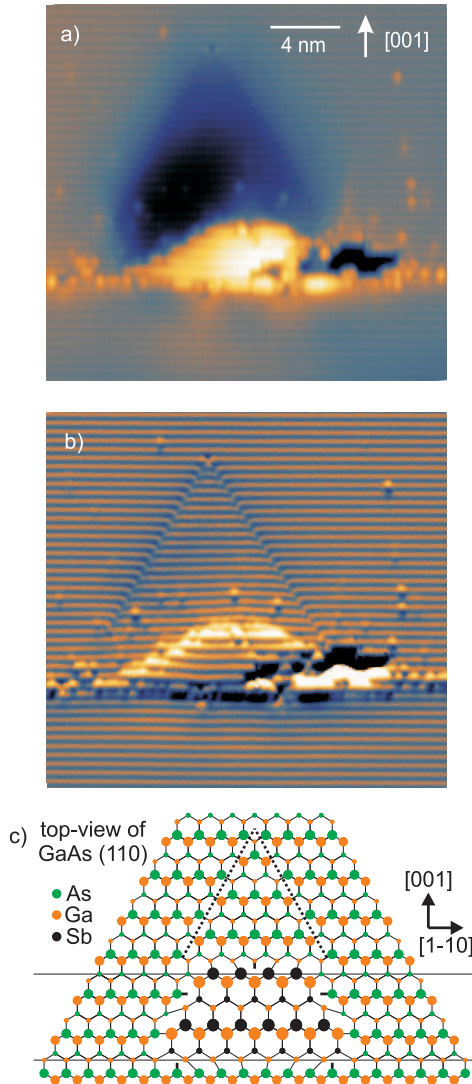
Figure 4.3: STM images taken at $V = -4.00$ V and $I = 250$ pA. Example of a defect near a QD capped with AlGaAs, visible in (a) a topographic and (b) a current image. (c) Structural model showing the (110) plane of the material, similar to the X–STM images. Around the QD, several misfit dislocations are visible that result in two stacking faults on top, extending into two different ⟨111⟩ directions.
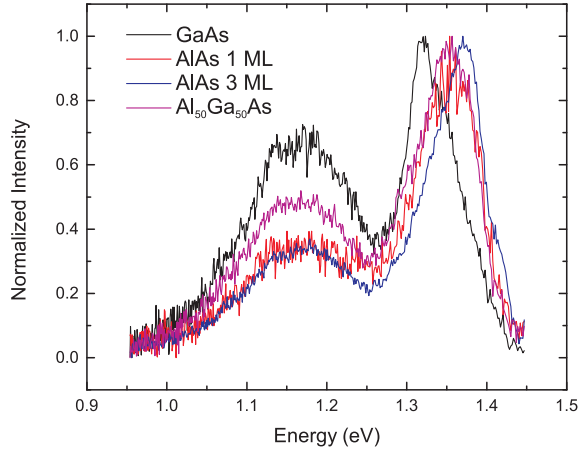
Figure 4.4: PL measurements of ten layers of QDs capped with GaAs, 1 ML of AlAs, 3 ML of AlAs, and AlGaAs. The samples were excited below the GaAs bandgap to isolate wetting layer and QD emission. Laser power density was approximately 2.6×10^3 Wcm^{-2}. The spectra are normalized to the wetting layer peak. Measured by M. DeJarld at the University of Michigan

4.4 Optical Emission

The change in QD height, as well as the presence of stacking faults, is expected to alter the optical properties of these films. The PL measurements depicted in Fig. 4.4 are consistent with the structural trends observed in the X-STM results. The energy positions of the wetting layer peak for the Al-containing capping are blue-shifted to between 1.35 and 1.36 eV, with respect to the GaAs capped sample that emits at 1.32 eV. Since the Al capped layers retained the QD height better than the GaAs capped layer, it is expected that less Sb out-diffused from the nanostructures in these samples. This means that the Al-rich overgrowth would result in a thinner wetting layer, which emits at higher energies. The uncertainty in our X-STM analysis of the wetting layer profiles does not exclude the shift in PL. Recent atom probe tomography (APT) measurements were able to accurately determine concentration profiles in GaSb/GaAs wetting layers of various heights and the corresponding PL indeed revealed a blue-shift for thinner wetting layers [106]. Additionally, the Al-rich capping material creates a larger energy barrier for the wetting layer with respect to the GaAs overgrowth. The resulting stronger hole confinement also contributes to a blue-shift in the wetting layer PL. Despite the observed increase in QD size with Al capping according to

X–STM, there is no significant change in QD peak position compared to the GaAs reference sample according to the PL. This is surprising, because larger QDs should emit at lower energies. We suggest that only smaller QDs, those with the same average height as in the GaAs capped sample, are optically active. The lack of emission from the larger QDs could be caused by the misfit dislocations and stacking faults acting as non–radiative recombination centers. Furthermore, the QD emission intensity is lower for the Al capped samples than for the GaAs reference sample. Inspection of Fig. 4.2 shows that the Al capped samples indeed have a lower absolute number of smaller, optically active QDs.

To obtain high uniformity GaSb QD layers with a good optical quality, we propose the growth of relatively small QDs capped with Al–rich material. This combines the benefit of preserving the original dot height by suppressing Sb out–diffusion while lowering the overall amount of strain, reducing the chance to inject strain relaxing structural defects that negatively affect the optical properties. Another approach would be to grow intermixed GaAsSb QDs or use an intermixed AlGaAsSb capping layer to reduce the strain and prevent stacking faults.

4.5 Conclusion

In summary, we show that the addition of Al into the GaAs capping layers result in higher, more intact GaSb QDs. This is due to the suppression of strain driven lateral Sb diffusion, As/Sb exchange and Sb segregation. A consequence of the QD erosion process is that misfit dislocations and stacking fault formation are enhanced during overgrowth. The optical properties of the studied nanostructures are consistent with the observed structural trends, showing lower intensity emission from the optically–active smaller QDs. We suspect the growth of smaller QDs or the use of As intermixing in the nanostructures or Sb intermixing in the capping layer can create a material with a good optical quality.

Bistable Si: Laser and Voltage Manipulation

A single Si dopant exhibits bistable behavior in the (110) surface layer of GaAs, where it is either positively or negatively charged. Its configuration can switch under influence of a locally biased tip of a scanning tunneling microscope (STM). For this work, to independently manipulate the Si charge state, the sample was illuminated by a laser during STM operation. The Si atom can be reversibly switched between its positive and negative charge state by turning the laser on and off, respectively. This process occurs mostly with the photon energy tuned above the bandgap of GaAs, indicating that photogenerated electron–hole pairs play an important role in the process. The occupation of the charge states depends on the carrier dynamics, i.e. the possibility of the electrons to escape or to be captured.

5.1 Introduction

In semiconductor devices, dopant atoms are important for the operation because of the free charge carriers they add to the material. With the scaling down of these structures, properties of individual dopant atoms start to play a role in their functionality. The influence of a single dopant atom on its surrounding environment can be studied with STM. Examples are studies of the deep acceptor Mn [61, 35], the shallow donor Si [57, 58] or the shallow acceptor Si [59, 60] in the surface of GaAs. A more complete understanding of the fundamental properties of dopants will assist in the development of

---
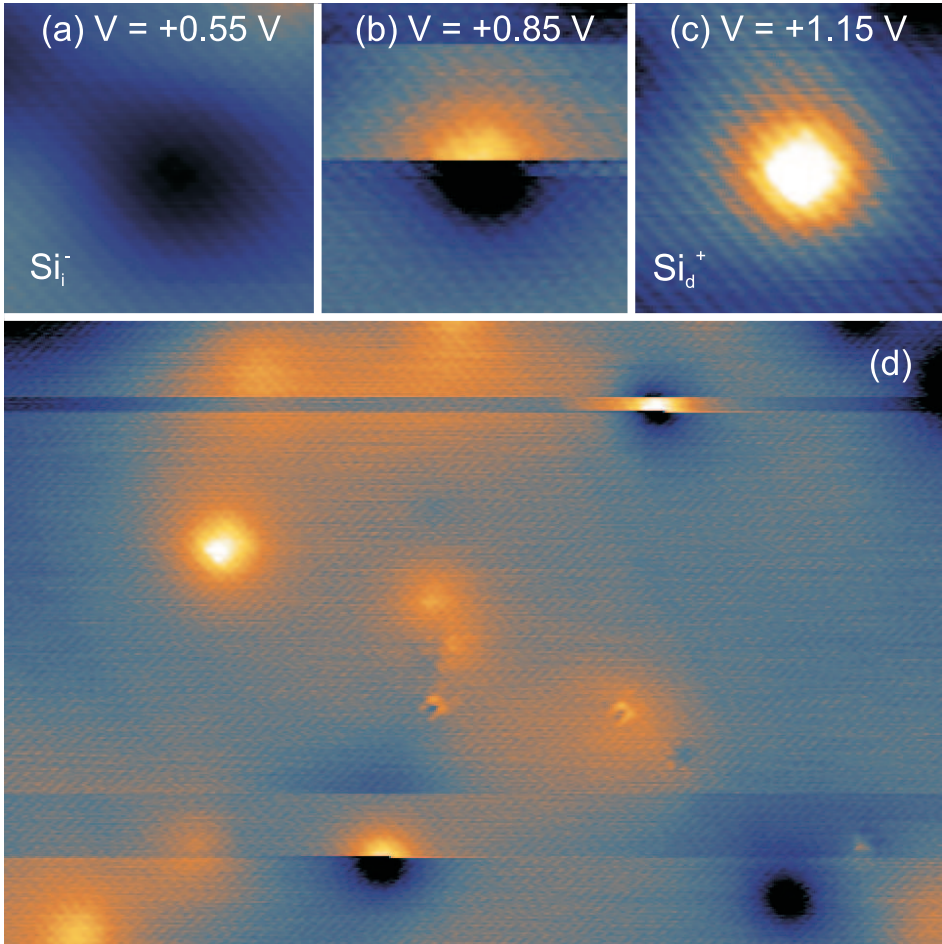
Figure 5.1: (a–c) Example of a bistable Si atom in the GaAs (110) surface, STM topography of 10×10 nm^2 taken at $I = 100$ pA. (a) Negatively charged interstitial state Si_i^-. (b) Bistable behavior during scanning. (c) Positively charged donor state Si_d^+. (d) Two bistable Si atoms surrounded by Si donors (bright) and acceptors (dark). STM topography of 48×36 nm^2 taken at $V = +0.75$ V and $I = 50$ pA.
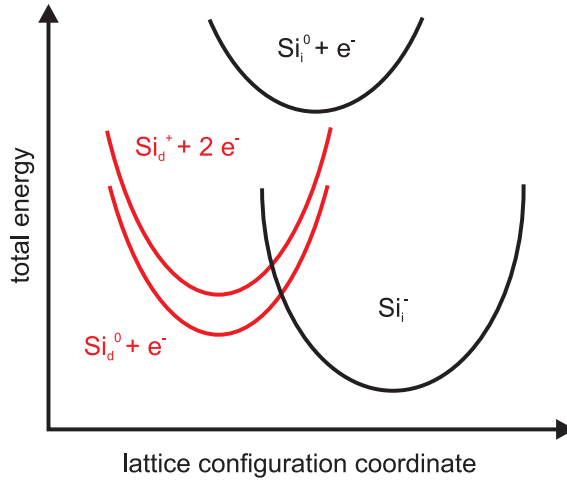
Figure 5.2: A qualitative lattice coordinate energy diagram of the Si atom in the (110) surface layer of GaAs, see the text for explanation.

In the figure, the vertical axis is labeled "total energy" and the horizontal axis is labeled "lattice configuration coordinate". The curves are labeled $Si_i^0 + e^-$, $Si_d^+ + 2\,e^-$, $Si_d^0 + e^-$, and Si_i^-.

so–called solotronic or single dopant electronic devices [8]. In this work we discuss laser and voltage manipulation of bistable Si dopants in the GaAs (110) surface.

An STM simultaneously collects information about the topography and the electronic properties of a surface, which allows for imaging the charge state of single dopant atoms. Here we focus on Si in GaAs, which is a donor when located on a Ga site and an acceptor when on the position of a As atom. A bright contrast in the STM images corresponds to the Coulomb field of a positively charged Si donor [107]. Ionization of the shallow donor state occurs at positive sample bias voltages, due to the local upward tip induced band bending (TIBB) [69]. Similarly, at these tunneling conditions, Si acceptors in GaAs appear dark because they are negatively charged.

Si atoms in the GaAs (110) surface layer show bistable behavior in STM measurements [21]. The exact depth of Si with respect to the GaAs surface can be determined by topographic height measurements. It was shown that only and all the Si in the topmost surface layer are bistable at low temperature and below this layer the behavior is not observed. During scanning of the STM tip, the Si can switch between a dark and a bright contrast. Examples of switching Si atoms can be seen in Fig. 5.1. In the presented STM images, the fast scan direction of the tip is left to right and the slow scan direction bottom to top. In Fig. 5.1 (a) Si appears with the dark contrast of a negatively charged dopant at relatively low positive sample bias voltage. In Fig. 5.1 (c)

a higher voltage is applied and now a positive charge state is visible. There is an intermediate critical voltage at which the Si configuration is bistable, see Fig. 5.1 (b) and (d). The switching between positive and negative charge occurs within one STM image at random positions during scanning. The exact value of this critical voltage is affected by the tip work function, which controls the amount of TIBB at the surface of the semiconductor [33]. Also there is a slight variation between various bistable Si in the surface layer, due to the random distribution of other charged dopants in their neighborhood, leading to a different electrostatic environment.

The STM observations show many similarities to the behavior of the DX^- center in bulk semiconductors. Here dopants also appear in bistable configurations, which can be related to different lattice positions [108, 109]. In the case of the DX^- center in bulk GaAs under hydrostatic pressure, the negative charge state involves the breaking of one bond between the Si and an As neighbor, combined with a lattice relaxation of the dopant to an interstitial position and a more localized charge distribution compared to the donor configuration. Recent density functional theory (DFT) calculations revealed that indeed the Si atom in the GaAs (110) surface can occupy similar bistable configurations [110, 111], but without any broken bonds. It was shown that a negatively charged Si atom on an interstitial position in the lattice has a total energy of ~ 500 meV lower compared to when it sits on a substitutional donor position in a neutral charge state.

A qualitative lattice coordinate energy diagram of the Si atom in the (110) surface layer of GaAs is shown in Fig. 5.2. The total energy of the Si is depicted for different charge states as a function of the lattice coordinate [108, 111]. Extra electrons are added in the diagram for a correct energy comparison between the configurations. On the left, the substitutional donor configuration is indicated in red. There is the neutral charge state plus one electron in the bulk, Si_d^0, and the positive charge state plus two electrons in the bulk, Si_d^+. The energy difference between the neutral and positive donor state can be overcome by the presence of the STM tip through upward TIBB, leading to clear rings of ionization appearing in the STM images [69]. Additionally, charge configurations exist that are located on interstitial positions in the lattice, displayed on the right and indicated in black. These are either neutral plus one electron in the bulk, Si_i^0, or negatively charged, Si_i^-. The neutral interstitial configuration has not been observed by STM measurements. Important here is that in order to switch between the positive and negative charge states observed in the measurements, an energy barrier needs to be overcome in either direction.

Experiments were performed in an Omicron LT–STM, operated at a tem–
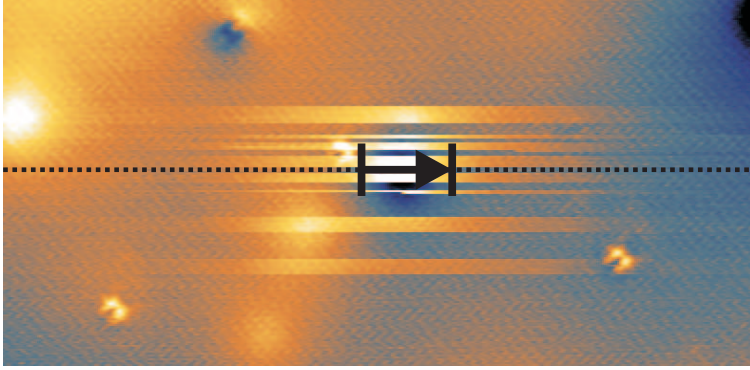
Figure 5.3: Illustration of the line restriction (dotted line) applied during measurements. Only part of the line scan directly on top of the bistable Si atom (bracketed arrow) is shown in Fig. 5.4 and 5.6. STM topography of 40×20 nm^2 taken at $V = +0.75$ V and $I = 50$ pA.

perature of $T = 5$ K with a base pressure of $p \leq 2 \times 10^{-11}$ mbar. Electrochemically etched tips made from polycrystalline W wire were used. Further tip preparation was done under ultra–high vacuum (UHV) conditions, including heating and Ar sputtering for improved stability [37]. We studied commercially grown GaAs wafers n–doped with Si with a concentration of $\sim 2 \times 10^{18}$ cm^{-2}. The samples were cleaved in UHV, to obtain atomically flat and clean (110) surfaces.

To study the behavior of a Si atom in time, the STM tip is restricted to scan over a fixed single line, see Fig. 5.3. These repetitive line scans track the charge state and record any switching event on or around the Si atom. This allows not only the determination of switching dynamics in time, but also enables a systematic way to study the variation of tip parameters like bias voltage and tunneling current on a single dopant. Moreover, an optical experiment is possible in which a laser illuminates the sample surface. The laser is turned on or off and the effects on the Si atom are recorded directly as function of time by the scanning STM tip.

5.2 Laser and Voltage Manipulation

In the STM setup, a $\lambda = 632$ nm diode laser was focused to a ~ 0.1 mm radius spot on the sample and tip by means of an in situ lens in the STM [47]. The effect of illumination with photon energy $U_p = 1.96$ eV on the configuration of the Si atom is shown in Fig. 5.4 (a). For clarity, only 2 nm of the scanned line
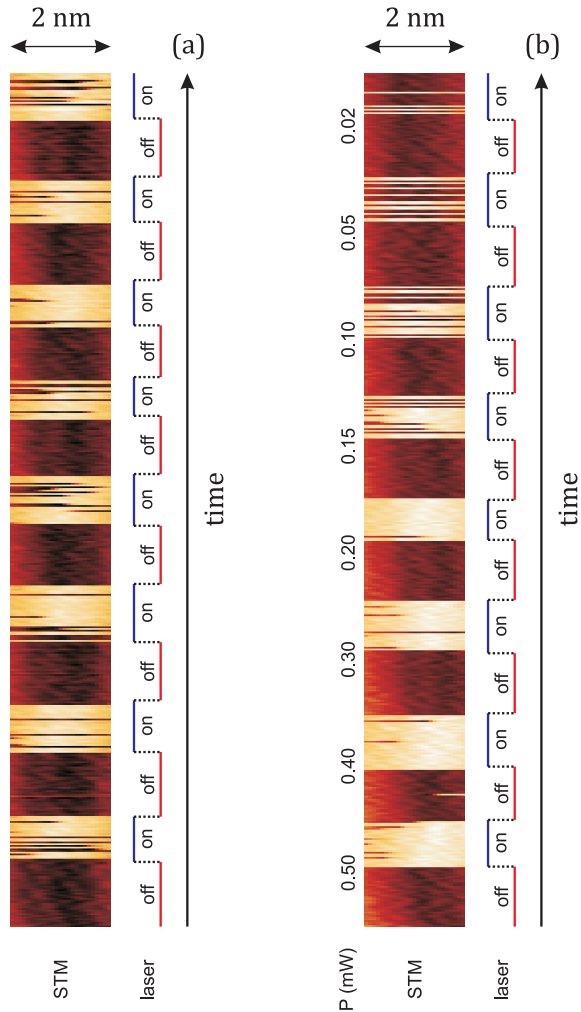
Figure 5.4: (a) A 12 minute long STM line scan recording the charge state of a Si atom in the GaAs surface. The bias voltage $V = +0.50$ V, which favors the dark Si_i^- if the laser is off. $I = 50$ pA, $P = 0.25$ mW and $U_P = 1.96$ eV in this experiment. Illumination results in the bright Si_d^+ being the predominant state. (b) A similar experiment in which the laser power is varied, showing a gradual decrease of the bright state occupation with lower laser power.

on top of the Si atom is depicted as function of time. The rest of the 60 nm line scan was used to appropriately level the contrast of the Si atom against the GaAs surface. This means the dark and bright contrasts here represent the negative and positive charge states respectively. The tunneling conditions are chosen such that Si_i^- is favored when the laser is off. In this case, the bias voltage $V = +0.50$ V, resulting in a near absence of spontaneous switching to Si_d^+. When the laser is turned on, the Si atom immediately switches to the bright state. During illumination, switching back to the dark state occurs sometimes at random positions, but this effect is rare. The effect of varying laser power P is shown in Fig. 5.4 (b). Lower power gradually leads to less occupation of Si_d^+, with the lowest power settings matching almost full occupation of Si_i^- when the laser is off.

To understand the physical mechanism behind the observed behavior, we view the tip–sample system in terms of energy. To incorporate the bound electrons qualitatively in the model, two different energy levels should be distinguished: the substitutional donor state at the surface where the binding energy is ~ 40 meV [16] and the interstitial state located ~ 500 meV below the conduction band minimum [110, 111]. Note that both energies differ from the value of 6 meV for a Si shallow donor in bulk GaAs. From this, the influence of the tip on the occupation of both states can be understood, see Fig. 5.5 (a–b). If the TIBB is large enough, the bound electrons from Si_i^- can tunnel into the conduction band of the sample, making it possible to switch to Si_d^+. However, if the band bending is small, the electrons can not escape and Si_i^- is the favorable configuration.

The effect of illumination can be considered for a system of metallic tip and semiconductor sample [50]. If the laser is tuned above the bandgap of GaAs, electrons and holes are created that result in a photocurrent and a photovoltage. The photocurrent is in the same direction as the tunneling current between tip and sample, so the STM feedback in constant current mode retracts the tip slightly for compensation. The photovoltage counteracts the applied bias voltage. Both effects result in a decrease of the TIBB. To estimate if these effects are relevant in our experiments, we studied the size of donor Si disks of ionization as function of applied laser power [69]. There was no visible change in disk size with the laser power up to 4 times higher than the values used in the rest of the experiments, meaning the change in TIBB due to illumination is negligible. Furthermore, a decrease of TIBB can not explain the observed occupation of the bright state being due to illumination, because this situation would favor the dark state.

An explanation for the observed illumination effect on switching is found in electron–hole recombination, which is illustrated in Fig. 5.5 (c–d). Part of
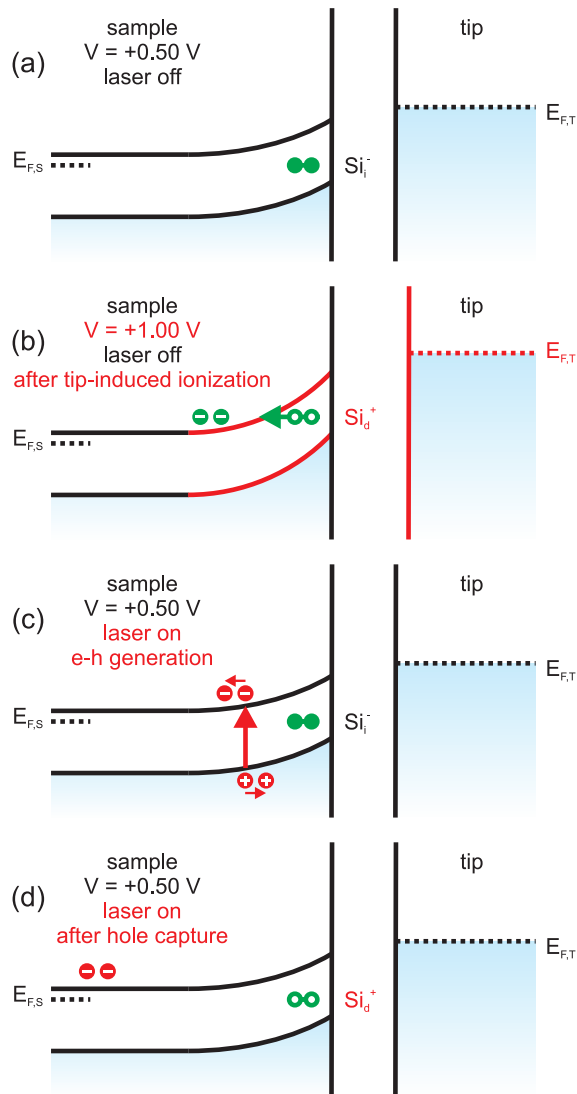
Figure 5.5: (a) The tip–sample band image without illumination. The inter–stitial level is indicated by the solid green line, with two electrons occupying this level. At these tunneling conditions, Si_i^- is favored. (b) When the TIBB is increased the electrons can escape by tunneling into the conduction band. (c) The effects of illumination: electrons and holes are created. The holes accumulate in the region of TIBB. (d) When the holes recombine with the bound electrons on the Si, the atom switches to Si_d^+.

the holes that are created by photon absorption accumulate in the region below the tip, because of the local upward TIBB there. Electrons from Si_i^- can now recombine with the available holes, creating a path for the electrons to effectively escape the Si atom.

The immediate switching to Si_d^+ both at high bias voltage and at high laser power suggest that under these conditions the escape of electrons from the dopant atom is a relatively fast process. The relevant timescale is then faster than or in the order of the sample frequency of the STM, which is 1 kHz, because we observe only few dark pixels under these conditions. In case of an applied bias voltage, the TIBB is the parameter that determines the chance of quantum tunneling for electrons into the conduction band. Under illumination and low TIBB, the photoexcited hole concentration determines the recombination rate.

Switching to Si_i^- is strongly dependent on the tunneling current and reaches a frequency of about 1 Hz for $I = 250$ pA [21]. The switching depends on the availability of electrons introduced by the tip, which is favored by a high current. At the same time, a high local TIBB repels electrons. This means there is a finite distance away from the center of the Si atom where the switching to the dark state is most efficient. Another consequence of this is that for certain tips the switching to Si_i^- is never possible while the tip is near the dopant. This is a reason why the length of the line traces in the measurements presented here are typically 60 nm, preventing any proximity effect and allowing the Si atom to relax back into its negative charge state with the tip far enough away. We also suspect that ultra–sharp tips with an apex of only a few nanometers are required to observe the switching behavior. More blunt tips already influence the Si configuration at a large distance, making it impossible to record any change in the charge state.

A possible effect influencing the optical switching of the charge state is optically induced charge depletion [112, 113]. At relatively low laser power, while photoexcited holes recombine with the electrons on Si_i^-, photoexcited electrons occupy donor states in the material and are not available for capture on Si_d^+. However, at higher laser power these donor states are saturated and more electrons are available for capture on the bistable Si dopant. Therefore, it might be that at higher laser power than used in this study, the negative charge state becomes more favorable again. A related effect that also might influence the switching is the altered local band bending due to the change of the charge on the dopant itself, creating a dynamic equilibrium. A positive charge slightly lowers the electronic bands, making it easier for electrons to be captured on the dopant. Similarly, a negative charge slightly raises the electronic bands and makes electron escape easier.

5.3 Photon Energy Dependence

To confirm that the switching indeed depends on holes originating from absorbed photons, the sample was again illuminated with a laser, but now with varying photon energy. This was accomplished by using a tunable Ti:Sapphire laser, enabling a wavelength range of $\lambda = 780$–920 nm. If the bright state occupation depends on the availability of holes in the surface region, tuning the photon energy below the bandgap of GaAs should stop this effect. In this experiment, of which the results are shown in Fig. 5.6 (a), the laser power was kept constant at $P = 0.25$ mW and the photon energy was varied between $U_p = 1.41$–1.59 eV. The bandgap of GaAs at $T = 5$ K is $E_g = 1.52$ eV, so this range investigates the effects of illumination below and above the bandgap.

At photon energies above the bandgap, an almost full occupation of the bright state is visible, similar to Fig. 5.4 (a). However, at subsequent lower photon energies below the bandgap, the bright state occupation becomes less, until it reaches the laser off level at $U_p = 1.41$ eV. This supports the idea that electron–hole pairs created during illumination play an important role in the dynamics of the bistable Si atom.

In Fig. 5.7 the occupation of Si_d^+ is shown as function of photon energy. Each data point in the graph represents the statistics of 12 minutes under the same illumination and tunneling conditions. It reveals a gradual decrease of the occupation with the photon energy tuned further below the bandgap of GaAs. It does not fall directly to zero below the bandgap and we propose this effect can be explained by local TIBB. With above bandgap excitation, holes are created everywhere in the illumination area of the sample. Diffusion then brings the holes near the region of the TIBB, where they can recombine with the bound electrons of the Si atom. When the laser is tuned below the bandgap, only in the region with enough TIBB photons can still be absorbed. This is due to the electric fields from the tip, creating a strong local Franz–Keldysh effect. An electron can be photoexcited from the valence band that is shifted up, to the conduction band with a lower shift slightly farther away from the tip, where the electron and hole wavefunctions still overlap. The created hole is then available for recombination with electrons on the Si atom.

The photon absorption α in a semiconductor under influence of an electric field is described by an Airy function. The below bandgap part is of the form [114]:

$$\alpha \sim e^{-(8\pi\sqrt{2m_{eh}^*})/(3heE_s)\cdot(E_g-U_p)^{3/2}},\qquad(5.1)$$

where m_{eh}^* is the exciton effective mass, e the electron charge and E_s the electric field at the surface induced by the STM tip. $E_s = E_{BB}/(ew)$, where
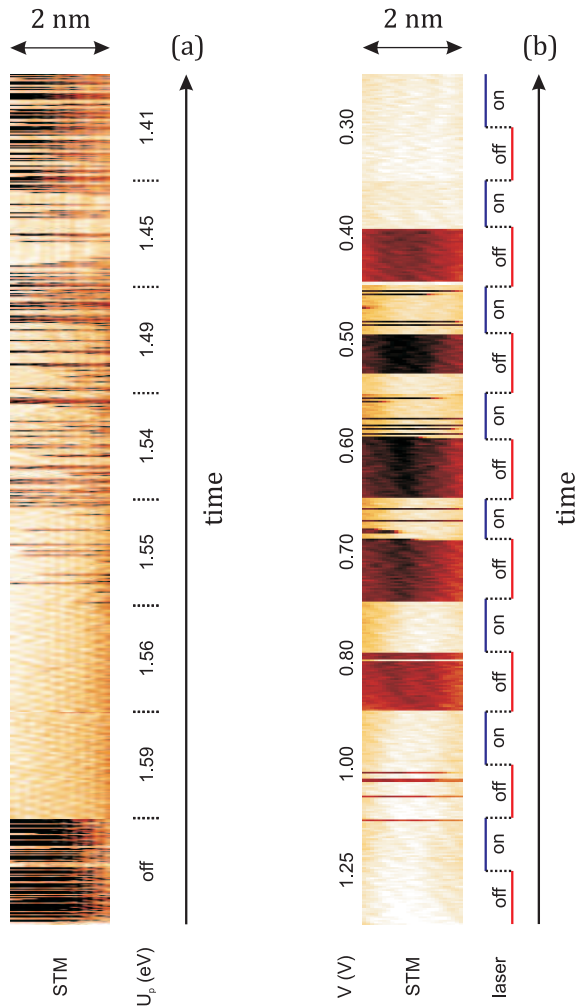
Figure 5.6: (a) A 12 minute long STM line scan recording the charge state of a Si atom in the GaAs surface showing the effect of varying photon energy, with $V = +0.65$ V, $I = 100$ pA and $P = 0.20$ mW. (b) A similar scan in which the bias voltage is varied. $I = 50$ pA, $P = 0.25$ mW and the photon energy is fixed at $U_p = 1.96$ eV, well above the bandgap of GaAs.
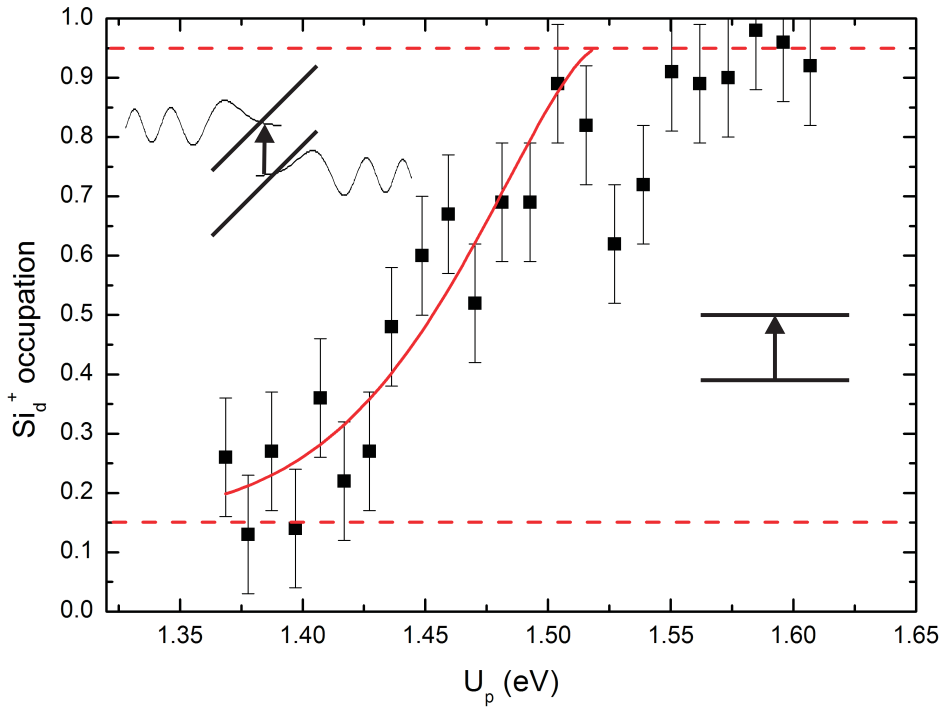
Figure 5.7: The occupation of Si_d^+ as function of photon energy. The dotted red lines indicate levels of 15% and 95% for the dark to light spontaneous switching and the reverse process, respectively. The solid red line is a fit of below bandgap photon absorption in a semiconductor under influence of an electric field using Eq. 5.1. $V = +0.50$ V and $I = 250$ pA for all data points. The two schematics illustrate the photon absorption in a semiconductor with and without an added electric field, on the left and right respectively.

E_{BB} is the TIBB potential energy at the surface and w is the depletion length in the semiconductor. The depletion length can be estimated using a typical work function for W of $\Phi_{WF} = 4.50$ eV [33], which results in $w = 19$ nm [67].

Fitting Eq. 5.1 yields $E_{BB} = 0.7 \pm 0.4$ eV. The fit follows the data quite well and the obtained value for E_{BB} is in the expected order of magnitude [67, 33]. The extraction of the value for the TIBB through this optical method might prove to be more exact than when using only electrical information obtained with the STM.

In another experiment, the sample bias voltage was varied with the photon energy fixed above the bandgap of GaAs, see Fig. 5.6 (b). For every voltage, the laser was turned on and off to study the influence on the Si configuration. For relatively high voltage, e.g. $V = +1.00$ V, Si_d^+ is predominant, regardless of the presence of illumination. This is because the sample is biased above the critical voltage at which the electrons from the interstitial level can tunnel into the conduction band through upward TIBB, see Fig. 5.5 (b). For intermediate positive V, the dark state is favorable when the laser is off, like is shown also in Fig. 5.4. Illumination creates holes, which allow the electrons from Si_i^- to recombine and escape the atom. For low bias voltages, e.g. $V = +0.30$ V, Si can be put in the bright state by turning on the laser, but it does not switch back to the dark state when the laser is turned off. This can be understood by considering the energy barrier that has to be overcome in order to change the configuration of the dopant, see Fig. 5.2. When electrons are injected from the STM tip with a low energy eV, the atom cannot cross the energy barrier from Si_d^+ back to Si_i^-. This is because the provided energy by the electrons is not enough to relax the atom into a different lattice position, probably by either inelastic excitation of phonons or quantum tunneling [21]. Therefore scanning at low bias voltage allows us to determine the charge state of the Si atom, without the STM tip affecting it.

5.4   Conclusion

By combining optical measurements with STM, we were able to study the dynamics of the bistability of the Si atom in the (110) surface layer of GaAs. The Si charge state is affected by the laser and the applied bias voltage. The electrons from Si_i^- can escape via tunneling into the conduction band at high TIBB or, under illumination, via electron–hole recombination, both resulting in Si_d^+ being favorable. At low bias voltage, the Si atom does not switch its configuration due to the energy barrier that is in between the two charge states.

Chapter 6

Bistable Si: Single Atom Solid State Memory

In this chapter, the dynamic behavior of single bistable Si dopants in the GaAs (110) surface is investigated using a scanning tunneling microscope (STM). These dopants switch between a negative and positive charge state under influence of the STM tip. The Si atom switching frequency shows a clear dependence on the bias voltage and tunneling current, because these parameters influence the escape and capture processes of electrons. Our physical model for these processes matches well with the experimental data. By choosing the appropriate tunneling conditions, we show that a single dopant is employed as a non-volatile memory element. The STM tip serves both as an electrical gate to write and as a probe to read the information stored on that single Si atom.

6.1 Introduction

Moore's law [2] describes the tremendous downscaling of the size of a transistor in the past decades. An equal trend has affected other electronic components such as for instance a memory cell. Reducing the size of current flash memory further could potentially decrease the energy needed for operation and increase the read and write speed. It is an ultimate dream to realize charge-based electronic functionality such as non-volatile memory operations on a single atom that is locked into place in a semiconductor host [8]. Several examples of atomic-scale charge-based electronic device func-

---
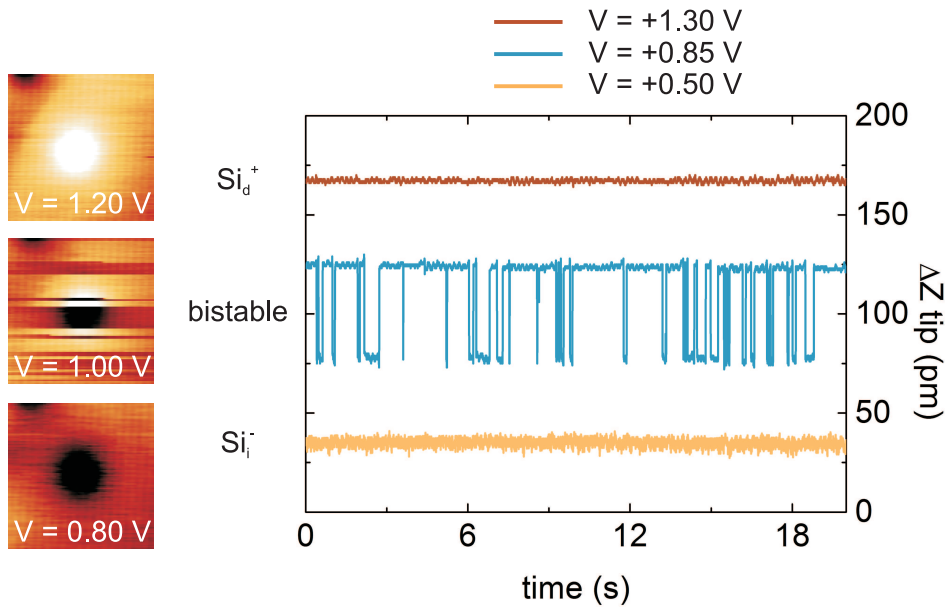
Figure 6.1: (left) 8×8 nm^2 STM topography images of a single bistable Si atom in the GaAs (110) surface, where the fast scan direction is left to right and the slow scan direction is bottom to top. $I = 70$ pA and $T = 5$ K. (right) STM tip height traces recorded in time, offset from each other for clarity. The top brown line corresponds to a stable Si_d^+ and the bottom orange line to a stable Si_i^-. The middle blue line shows the switching behavior in time as random telegraph noise. $I = 75$ pA and $T = 77$ K.

tionality have been demonstrated recently. For instance, on atomically flat surfaces, chains of atoms [115, 116] and dangling bonds [117, 118] were constructed that can be employed in logic operations. In other studies, charge manipulation on single dopants is reported that allows the tuning of the local electronic transport through transistor devices [10, 119]. Furthermore, purely mechanical bistable atomic–scale systems have been demonstrated in the form of molecule cascades [120], buckled dimers at the Si (100) surface [121] and atomic break–junction structures [122]. In this work, we investigate the dynamics of a single bistable Si dopant in the GaAs (110) surface with STM and connect the switching behavior with a physical model to the relevant tunneling barriers in the system. Furthermore, we show how a single Si dopant atom has been successfully used as a memory cell on which the information can be stored ≥ 25 s, albeit with switching times on the second timescale at $T = 5$ K. We suggest that there is no fundamental objection to transfer this approach to a device in the bulk because similar bistable behavior is well–known for the same Si dopant embedded in bulk AlGaAs, known as the DX^- center [109].

GaAs n–type wafers doped with a Si concentration of $\sim 2 \times 10^{18}$ cm^{-3} were used in the experiments. To obtain atomically flat and clean (110) surfaces, the samples were cleaved in ultra–high vacuum (UHV) under a pressure of $\leq 2 \times 10^{-11}$ mbar. The measurements were performed in an Omicron LT-STM operated at $T = 5$ and 77 K. Polycrystalline W wires were electrochemically etched to obtain tips with an atomically sharp apex. Tip heating and Ar sputtering were done under UHV conditions for improved stability.

Si in GaAs is a dopant that is well studied by STM [57, 58]. Recently, bistable behavior of Si atoms in the (110) surface layer of GaAs was observed during scanning with a STM tip, see Ref. [21] and Chap. 5. Fig. 6.1 illustrates this bistability with STM topographic images of the same Si dopant. The bright contrast, stable at relatively high bias voltage, resembles a positively charged Si donor coordinated on a Ga site in the lattice, which is relaxed inwards with respect to the surface, denoted as Si_d^+. A clear ionization disk can be observed around the dopant, that corresponds to the boundary between the neutral and positive charge state of the Si atom. The ionization occurs through the local presence of the tip due to tip induced band bending (TIBB) [69, 107]. Density functional theory (DFT) calculations confirm that the dark contrast, stable at relatively low bias voltage, corresponds to a negatively charged Si, denoted as Si_i^- [111]. It has moved slightly in the lattice, from the original relaxed Ga site to a position located more outwards with respect to the surface. Si_i^- is energetically the most favorable configuration in the (110) surface of GaAs. Both configurations are metastable, meaning that

an energy barrier E_{bar} has to be overcome to switch from one state to the other [108, 109]. If the TIBB is large, electrons from the dopant can escape into the conduction band of the semiconductor host, resulting in Si_d^+. The opposite process of electron capture depends on the current injected by the tip. If the TIBB is small, captured electrons remain bound to the dopant atom, resulting in Si_i^-. Continuous switching occurs when both processes are active. Although in principle the neutral charge state of the donor–like configuration is stable at low temperature, in the experiments presented in this work the TIBB of the STM tip located directly on top of a bistable Si always resulted in either the positive or the negative charge configuration.

In several experiments described in this work, the Z–position of the STM tip was recorded in time, giving information about the charge state of a bistable Si atom. These measurements were conducted while the tip was in tunneling contact in constant current mode, but was restricted to a single point exactly on top of a bistable Si. This measurement configuration allows the recording of random telegraph noise of the switching when specific tunnel–ing conditions are applied, see Fig. 6.1. The random telegraph signal noise data was taken at low temperature to limit both the horizontal and lateral drift of the tip and sample. The distance between tip and sample, which can only be estimated, is in the order of 1 nm. However, the tip height ΔZ is the exact distance with respect to a fixed reference level determined by the piezo motors of the STM. For every combination of bias voltage and tunneling cur–rent, the tip height changes accordingly. Therefore, in order to determine the Si charge state, a reference measurement on the surrounding GaAs material is needed. We recorded 2D topographic images to obtain the charge state of the Si atom for every applied tunneling condition. This information is then used to determine the charge state when the tip is restricted to a single point. In the figure, the middle blue line shows bistable behavior of a dopant at a critical bias voltage of $V = +0.85$ V. The switching frequency at these condi–tions is about 1 Hz. Si_d^+ appears as an elevation in the surface corresponding to a retracted tip, while Si_i^- shows up as a depression corresponding to an extended tip. The difference in tip-sample distance between Si_d^+ and Si_i^- is in the order of 50 pm, which is well above the Z-noise level of the STM of about 5 pm. The top brown line is taken on top of the same bistable Si atom and shows a stable charge level corresponding to Si_d^+. Similarly, the bottom orange line represents Si_i^-.

To test if the switching is a fully random process, histograms with the residence times of Si_i^- and Si_d^+ are displayed on a semi–logarithmic scale in Fig. 6.2. The data is fitted to a Poissonian distribution [40]:
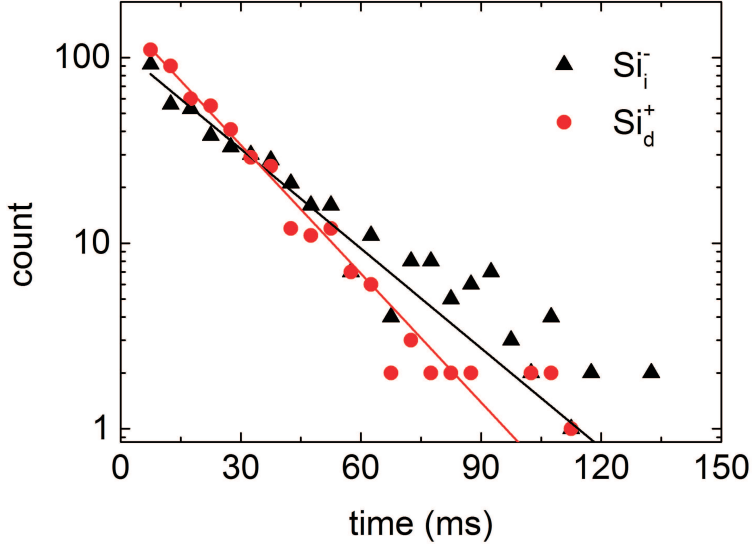
Figure 6.2: Residence time histograms of Si_i^- (red) and Si_d^+ (black) on a semi–logarithmic scale, $V = +0.98$ V, $I = 150$ pA. The fits are with Eq. 6.1.

$$P(t) = \frac{N}{2}p(1-p)^t, \tag{6.1}$$

with p the probability to switch to the other state, N the number of switching events and t the time. From the straight fits we conclude the switching follows Poissonian behavior and is therefore a random process. p can be expressed as an average switching probability per data point, which are recorded every 1 ms. In this case, for Si_i^-, $p = 0.052 \pm 0.001$ and for Si_d^+, $p = 0.040 \pm 0.002$. Both values are close to each other because the tunneling conditions were set to the critical bias voltage, where escape and capture of electrons occur roughly at the same rate.

6.2 Bistable Si Dynamics

In Fig. 6.3, various random telegraph noise measurements on single bistable Si dopants are presented that reveal the dynamic behavior of the switching process. For these measurements, analog electronics analyzing the tunnel–ing current were combined with the STM in order to evaluate the switching frequency and the occupation of the two charge states [44, 43].

In Fig. 6.3 (a–b) 2D maps on and around a bistable Si are depicted that
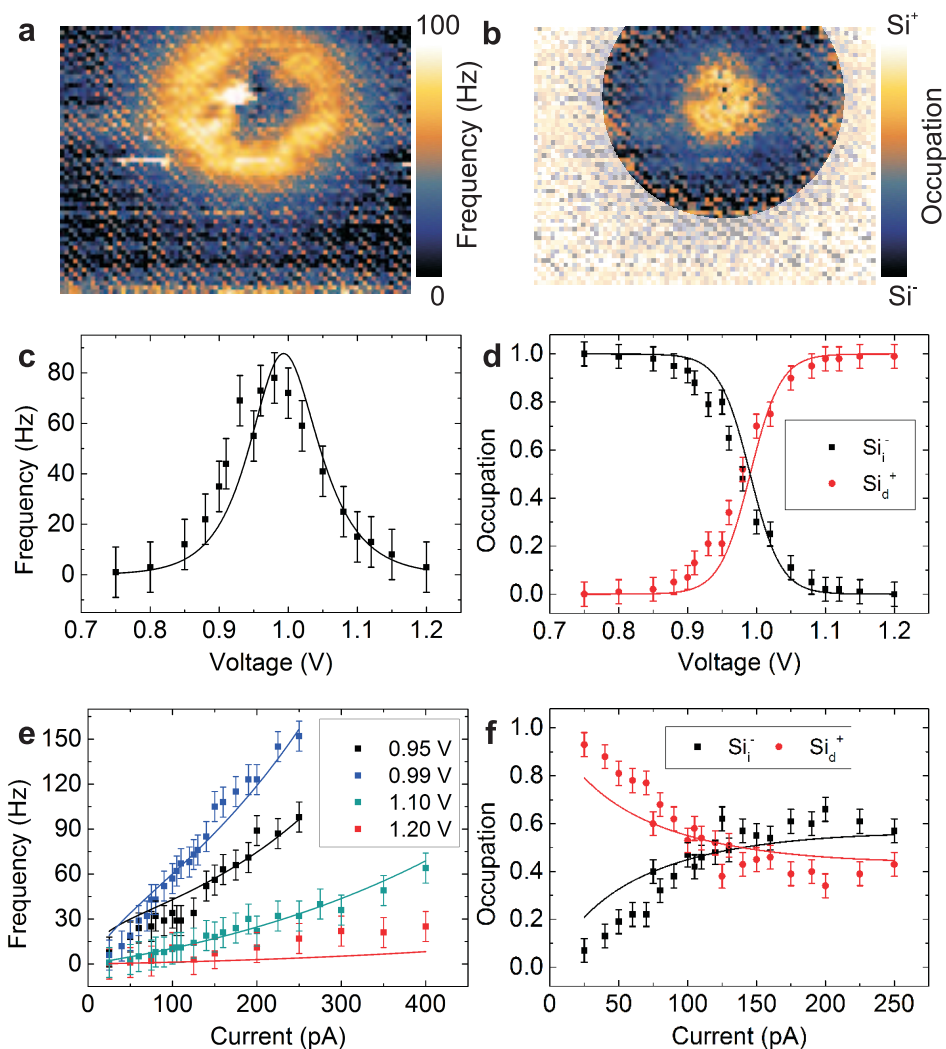
Figure 6.3: 2D maps of 8×6 nm^2, taken at $V = +0.75$ V and $I = 500$ pA, showing the spatial distribution of (a) the frequency and (b) the occupation of the positive and negative charge state, the latter within a circle of confidence. Switching frequency recorded at the center of the bistable dopant as a function of (c) bias voltage taken at $I = 150$ pA and (e) average tunneling current. Occupation of states as a function of (d) bias voltage taken at $T = 150$ pA and (f) average tunneling current taken at $V = +0.99$ V. Dots are the measurements, error bars originate from the noise in STM height data, lines are fits of the data with Eq. 6.4. Measurements were obtained at $T = 5$ K.
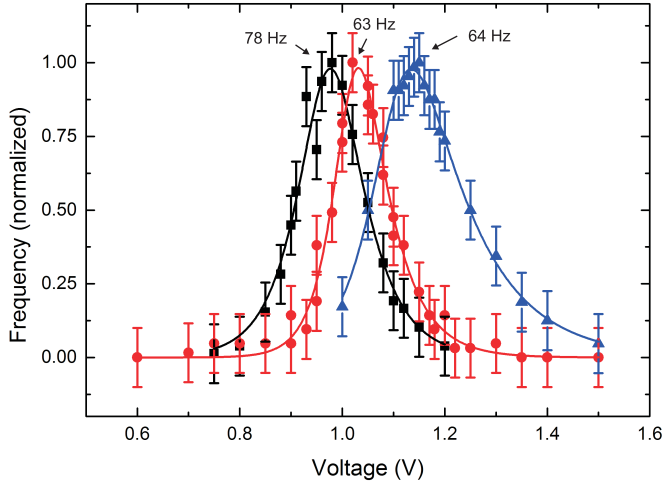
Figure 6.4: Comparison between three single bistable Si dopants of the switching frequency dependence on applied bias voltage. Measurements were taken with different tips at $I = 150$ pA (black), $I = 80$ pA (red) and $I = 95$ pA (blue). The data was normalized to the peak frequency, which is indicated for each curve. Dots are the measurements, error bars originate from the noise in STM height data, lines are fits of the data with Eq. 6.4. Measurements were obtained at $T = 5$ K.

represent the switching frequency and occupation of the positive charge state respectively. Depending on the exact location of the tip, the TIBB and current density at the location of the Si atom vary and thereby influence the dynamics of the dopant. When the tip is exactly on top of the Si, the positive charge state is dominant and the switching frequency is low. With the tip farther away, the negative charge state becomes more and more favored and the switching frequency increases. When the tip is even farther away, the negative charge state is dominant and the frequency drops again.

Measurements visible in Fig. 6.3 (c–f) were taken directly on top of another bistable Si for varying bias voltage and tunneling current, with the tip restricted to a single point. In this case, analysis was performed directly on the STM topographic height data, to appropriately take into account the changing height difference between the two charge states when varying the tunneling conditions. The observed switching frequency in (c) exhibits a maximum value around a critical bias voltage. This maximum coincides with an occupation of 0.50 for both configurations, visible in (d), indicating this is the point where escape and capture processes of electrons are of equal impor-

tance. Below the critical voltage, the escape rate of electrons is dominating, because that process is limiting the switching. Similarly, above the critical voltage, the capture rate of electrons is dominating. In (e) the switching frequency is depicted as a function of tunneling current for a few different bias voltages. Over the whole voltage range, the frequency scales roughly linear with the tunneling current. In (f), the occupation of the two charge states is shown on the same current scale. In this case, the occupation of the negative charge state increases gradually with the tunneling current. Both effects as function of current occur because more electrons are available for capture.

In Fig. 6.4 measurements on three different bistable Si are compared. The switching frequency data as function of bias voltage were obtained with different tips on similar samples. It is clear from the experiments that the maximum in the frequency is at a different bias voltage for each dopant and that the width of the distribution also changes. We expect the electron escape and capture processes of a bistable Si depend strongly on the local electrostatic environment in the sample [123] and on the TIBB that in turn depends on the exact work function of the tip [33].

6.3   Switching Model

To model the dynamic behavior of the charge switching, the escape and capture processes can be described independently. The average time to switch from Si_i^- to Si_d^+ and back is $<\tau> = <\tau_-> + <\tau_+>$, where $<\tau_->$ is the average time in Si_i^- and $<\tau_+>$ the average time in Si_d^+. The physical processes involved in the capture and escape are summarized in Fig. 6.5.

If the bias voltage V is increased at constant tunneling current I, or I is decreased at constant V, the vacuum barrier between the tip and the bistable dopant increases. This makes it harder for electrons with the same energy as the Si state to tunnel from the tip to the dopant level and be captured. We assume an exponential relation between the tunneling probability and V and I. Additionally, we expect that the switching is limited by the electron that brings the dopant from Si_d^+ to the neutral charge state at a shifted lattice position. The subsequent process of capturing another electron is fast and efficient. Therefore the capture process depends linearly on the tunneling current, which results in the following relation for the capture rate $f_{+|-}$:

$$f_{+|-} = <\tau_->^{-1} = a_1 \cdot e^{-\frac{V}{b_1} + \frac{I}{c_1}} \cdot I, \qquad (6.2)$$

where a_1, b_1 and c_1 are scaling coefficients.

For the opposite process of ionization a similar relation exists for the escape rate $f_{-|+}$, if we consider that it is easier for electrons to escape the
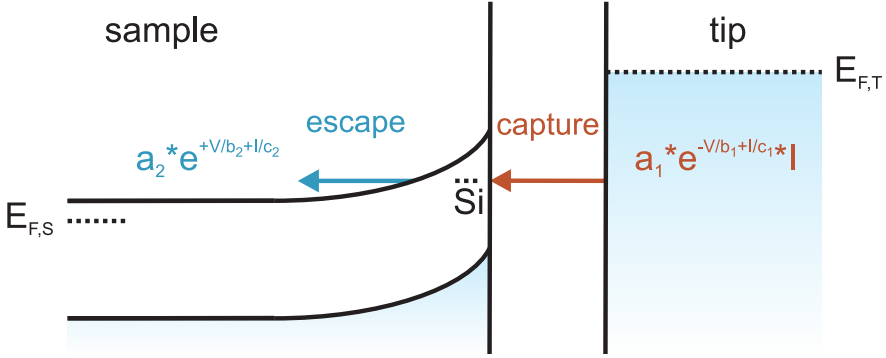
Figure 6.5: Energy diagram emphasizing the important physical processes involved in the switching.

dopant with increasing TIBB. This is included as an exponential growth factor in the model, because the width of the tunneling barrier in the sample between the Si state and the GaAs conduction band decreases with larger V, as well as with larger I. This results in:

$$f_{-|+} = <\tau_+>^{-1} = a_2 \cdot e^{+\frac{V}{b_2}+\frac{I}{c_2}},$$ (6.3)

where a_2, b_2 and c_2 are scaling coefficients.

The switching frequency f, the negative charge state occupation n_- and the positive charge state occupation n_+ that are observed in the measurement are expressed as:

$$\begin{aligned}
f &= <\tau>^{-1} = \frac{f_{+|-} \cdot f_{-|+}}{f_{+|-} + f_{-|+}}, \\
n_- &= f_{-|+}^{-1} \cdot f, \\
n_+ &= f_{+|-}^{-1} \cdot f.
\end{aligned}$$ (6.4)

The data recorded on a single dopant shown in Fig. 6.3 (c–f) was fitted with the physical model using Eq. 6.4. The following fitting procedure was used. The parameters b_1 and b_2 were estimated from the f vs V data. Using this as input, the f vs I data sets yielded the starting point for parameters c_1 and c_2. The occupation data then served as a further optimization and gave the range for parameters a_1 and a_2. In the final step, the fits on the full data set were optimized to find the best global match. We find $a_1 = 1.3$ GHz/pA,
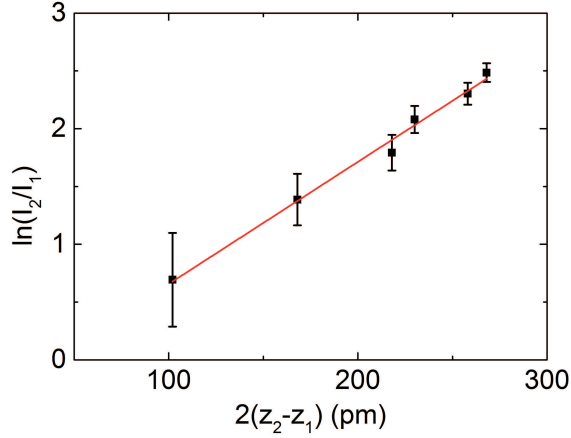
Figure 6.6: Logarithmic current ratio as a function of tip height difference, taken from the data shown in Fig. 6.3 (c–f), which allows the extraction of the decay length κ. Black dots are the data, red line is a linear fit using Eq. 2.3.

$a_2 = 4.7$ μHz, $b_1 = 47$ mV, $b_2 = 42$ mV, $c_1 = 0.60$ nA and $c_2 = 0.20$ nA. The large difference in order of magnitude between a_1 and a_2 is there because the offset for the frequency distribution maximum in terms of V is part of the prefactors. Moreover, the exponents contain both positive and negative contributions, further enhancing the difference between a_1 and a_2. The fits demonstrate that both the voltage and current dependence of the model are in good agreement with the experimental data. The switching frequencies in the order of ~ 100 Hz observed here are orders of magnitude lower than for example the $\sim 10^6$ Hz seen in the hopping of CO molecules on Cu (111), described in Ref. [120]. Moreover, tunneling currents of ~ 200 pA used in the experiments correspond to $\sim 10^9$ electrons s^{-1}, which implies that at $T = 5$ K only 1 in 10^7 electrons is captured on the dopant atom when the tip is located directly on top.

We estimate the effect of TIBB for the data shown in Fig. 6.3 (c–f) by determining the band bending at the surface from $I(Z)$ data [68, 33]. By using Eq. 2.3 and measuring the topographic height for various setpoint currents, we can extract the decay length κ. In Fig. 6.6, the logarithmic current ratio between two tunneling conditions is displayed against the tip height differ-ence for the same two settings. The slope of the linear fit yields a decay length of $\kappa = 10.6 \pm 0.5$ nm^{-1}. This quantity is converted to an effective barrier height Φ_B by:

$$\Phi_B = \frac{\kappa^2 \hbar^2}{2m_0},$$ (6.5)

in which $\hbar$ is the reduced Planck's constant and m_0 the electron rest mass. This gives $\Phi_B = 4.3 \pm 0.4$ eV. By using the calculation model from Ref. [67], which solves the Poisson equation iteratively, the flatband condition V_{FB} can be determined, which is the applied bias voltage at which there is no band bending at the semiconductor surface. Additionally, from this information the band bending energy at the surface E_{BB} can be calculated for every applied bias voltage. We obtain $V_{FB} = -0.9 \pm 0.7$ V. The switching frequency has a maximum at $V = +0.98$ V, which results in a TIBB of $E_{BB} = 0.4 \pm 0.2$ eV. These values demonstrate that there is positive band bending for all applied tunneling conditions, as is assumed in the analysis of this work. Furthermore, because we observe that the switching process starts roughly above $V = +0.80$ V, the corresponding TIBB of $E_{BB} = 0.3 \pm 0.1$ eV is an estimate of the binding energy of the Si_i^- state. This corresponds to DFT calculations that predict that this state is located much deeper in the bandgap than the donor state [110, 111].

6.4 Single Atom Memory

Through understanding of the dynamic behavior of the Si dopant, we can choose the tunneling conditions such that it can be employed for demonstrating memory operations on a single atom. The Si charge state is non–volatile at low temperatures, which enables the storage of information, see Chap. 5. For memory operation, three separate conditions need to be distinguished: (a) setting the system to Si_i^-, (b) setting it to Si_d^+ and (c) detecting the charge state. The two states can be set by choosing the bias voltage either relatively low or high respectively. If the energy eV of the STM–injected electrons is lower than the energy barrier between the two configurations, the switching can no longer take place, which allows the determination of the charge state without the STM tip affecting it.

Fig. 6.7 shows experimental results where the bistability of Si was used for performing non–volatile memory operations. In this measurement, the STM recorded data points at 1 kHz and every tunneling condition was set for 25 s. Three different tunneling conditions were applied in sequence and the recorded pattern was repeated four times to show the reproducibility. We demonstrate the single atom memory is stable for at least 25 s.

A relatively high bias voltage of $V = +1.50$ V and a high tunneling current of $I = 500$ pA favor the occupation of Si_d^+, because the electrons on the

Si atom can tunnel into the conduction band due to the large enough TIBB. We see no noticeable delay time in the change from negative to positive charge. In the figure we observe this "write (1)" condition as the regions with the largest tip height. The high voltage setting is the most flexible and stable of the three read and write conditions and works from about $V = +1.25$ V up to higher values. Below that the Si atom becomes bistable.

At an intermediate bias voltage of $V = +0.60$ V the Si atom switches to the negative charge state. Here the switching time is on average 1 s, which can be seen in the data as a small plateau at a larger tip height level for a short time, after which the atom switches to Si_i^-. The relatively long delay time for the "write (0)" condition is very different from that of the opposite process. For writing a (1), electrons need to escape into the conduction band, and at high TIBB this occurs very quickly. For writing a (0), two electrons supplied by the STM tip need to be captured by the Si atom and the chance for this is apparently small. The switching frequency increases with increasing tunneling current, but in this experiment $I = 500$ pA was the highest current we could apply without crashing the tip into the surface. The voltage condition corresponding to electron capture is quite critical, because a too high voltage leads to random switching and a lower voltage extends the write delay considerably.

A low bias voltage of $V = +0.40$ V does not influence the system and allows a "read out" of the Si charge state. To test for any hysteresis in the system, we applied several high and intermediate voltages in sequence, followed by a read out at low voltage. The read out always depended on the last write step only. The low current of $I = 5$ pA was chosen to stabilize the read out condition. A higher voltage increases the chance at writing a (0) and a lower voltage leads to more tip instability because it is tunneling closer to the bandgap.

We postulate that Coulomb interaction between bistable Si atoms can be used to build logic operators [124]. For this it is essential that the Si dopants can be positioned with atomic scale precision in the surface. Several methods have already been employed in other studies to embed dopants with high spatial accuracy [35, 10]. A charged Si dopant changes its surrounding potential landscape and therefore influences another Si dopant that is close enough. For instance if a Si is negatively charged, the local upward band bending will make it easier for neighboring Si to switch to the positive charge state. In this approach we expect that one can construct logic gates with multiple bistable Si atoms. Control over the charge state at the surface can be achieved by local gates and scanning probe techniques such as STM [69, 125] and atomic force microscopy (AFM) [115, 126].
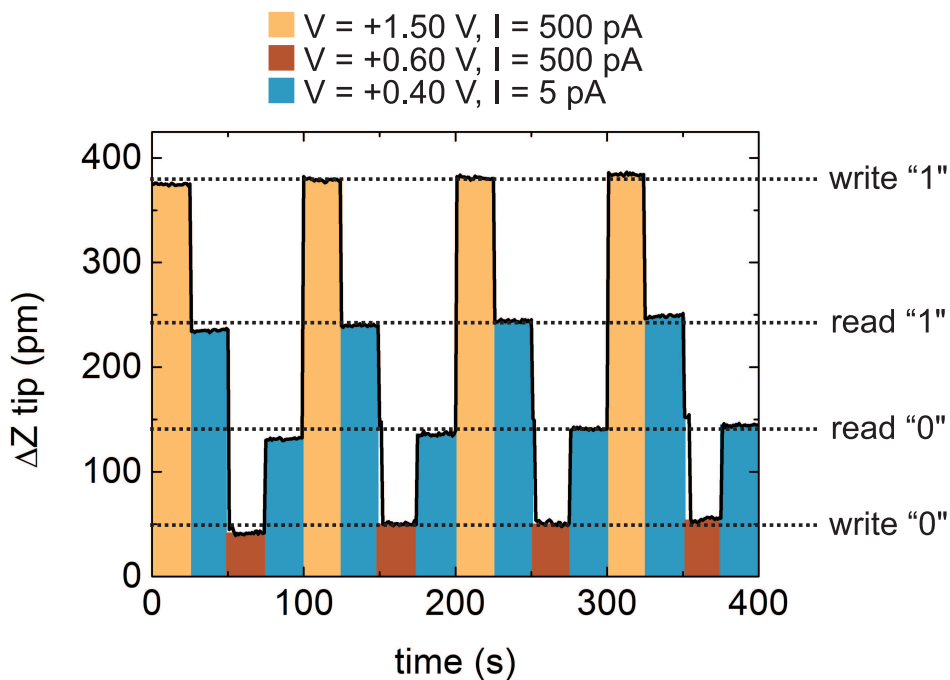
Figure 6.7: The solid line is a measurement of the STM tip height in time showing the repeated operation on an Si atom acting as a memory element, where Si_i^- is state (0) and Si_d^+ is state (1). The colors indicate different applied tunneling conditions and the dotted lines the resulting STM tip height levels. $T = 5$ K.
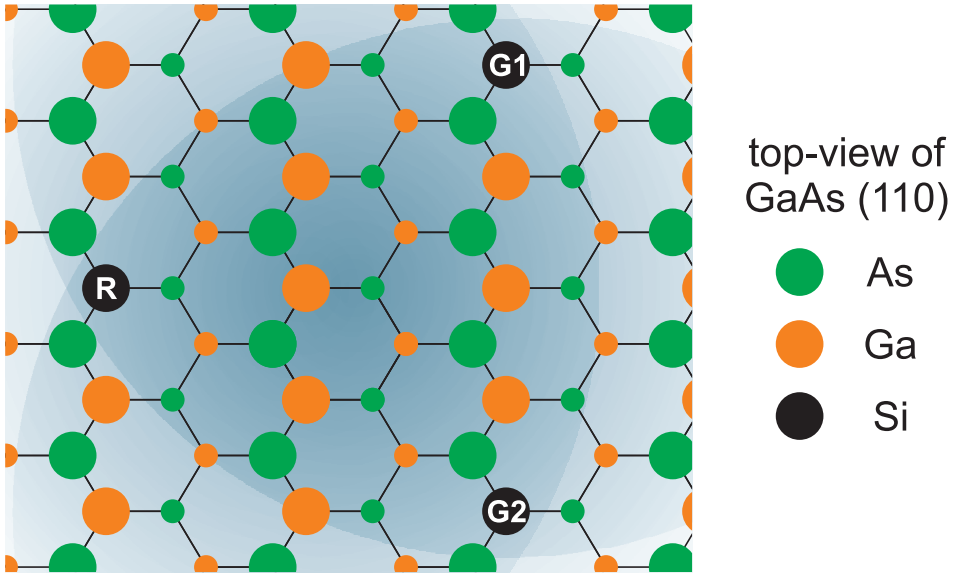
Figure 6.8: Visualization of three bistable Si in the GaAs surface used as a logic gate, where the disks around the dopants indicate the Coulomb effect they exhibit on their surrounding. The two gates $G1$ and $G2$ are manipulated by a scanning probe method and result in setting the result dopant R. This configuration would allow for example NAND or NOR operation, depending on the distance of the dopants to each other.

In Fig. 6.8 a visualization is depicted of three bistable Si that influence each other through Coulomb effects, allowing the construction of logic operators. If the Si are relatively far from each other, for example two input (1) states are needed to switch the output to (0), which effectively results in a NAND gate. Putting them closer together would then result in a NOR gate, because then only a change in one input is needed to switch the output state.

The application of embedded dopants as functional elements in a host material allows device operation outside UHV. The well-known bistable DX^- center in bulk [109], associated with for instance a single Si dopant in AlGaAs, can be utilized in similar manner as the presently studied Si in the GaAs surface. If the precise location of Si atoms embedded in bulk AlGaAs can be controlled or known, local nanoscale contacts and gates can be used to manipulate and probe a single Si DX^- center. This approach should thus allow for the creation of atomic-size charge-based devices, for instance memory cells or tunnel field-effect transistors (TFETs) [127]. Such devices can operate outside of UHV conditions and enable integration into more advanced electronic structures. Important prerequisites for real devices are the stability of the charge configurations at room temperature as well as the ability to write and read out at frequencies much higher than the dynamic range studied in this work.

6.5   Conclusion

In conclusion, the experiments and modeling of the switching dynamics of bistable Si atoms in the GaAs (110) surface reveal that electron escape and capture processes depend strongly on the applied tunneling conditions. We have demonstrated memory operations on a bistable Si dopant, where the STM tip acts as a gate for reading and writing the information.

Scanning Tunneling Luminescence on Si Dopants in GaAs

The scanning tunneling microscope (STM) probes the local electronic prop-erties of a surface with atomic resolution. This opens up the possibility to investigate other features on the same scale, for example luminescence. In optical experiments the spatial resolution is normally connected to the wave-length of the light and limited to λ/2. When a semiconductor is probed with scanning tunneling luminescence (STL), minority charge carriers injected by the STM tip recombine locally with majority charge carriers in the sample and photons are emitted, allowing a higher spatial resolution. In this chapter, optical properties of doped semiconductor surfaces are investigated with STL. The lateral variation of the observed integrated intensity is linked to the local density of states (LDOS) of the sample. The local effect of dopant atoms on the integrated luminescence is explained by considering the change in tip induced band bending (TIBB) with respect to the surrounding semiconductor host material.

7.1 Introduction

On metallic substrates, in many cases a high spatial resolution has been achieved in the mapping of the STL signal [26, 128]. On semiconductors, lat-eral contrast in the local luminescence has been observed from cross-sectional (X-)STM on heterostructures [45, 129] and from plane-view STM on quantum dots (QDs) [130, 49, 131]. Recently, atomic resolution in the STL intensity was obtained on an n-type GaAs (110) surface at low temperature, demon-strated in Ref. [27]. The authors argue the origin of the optically resolved
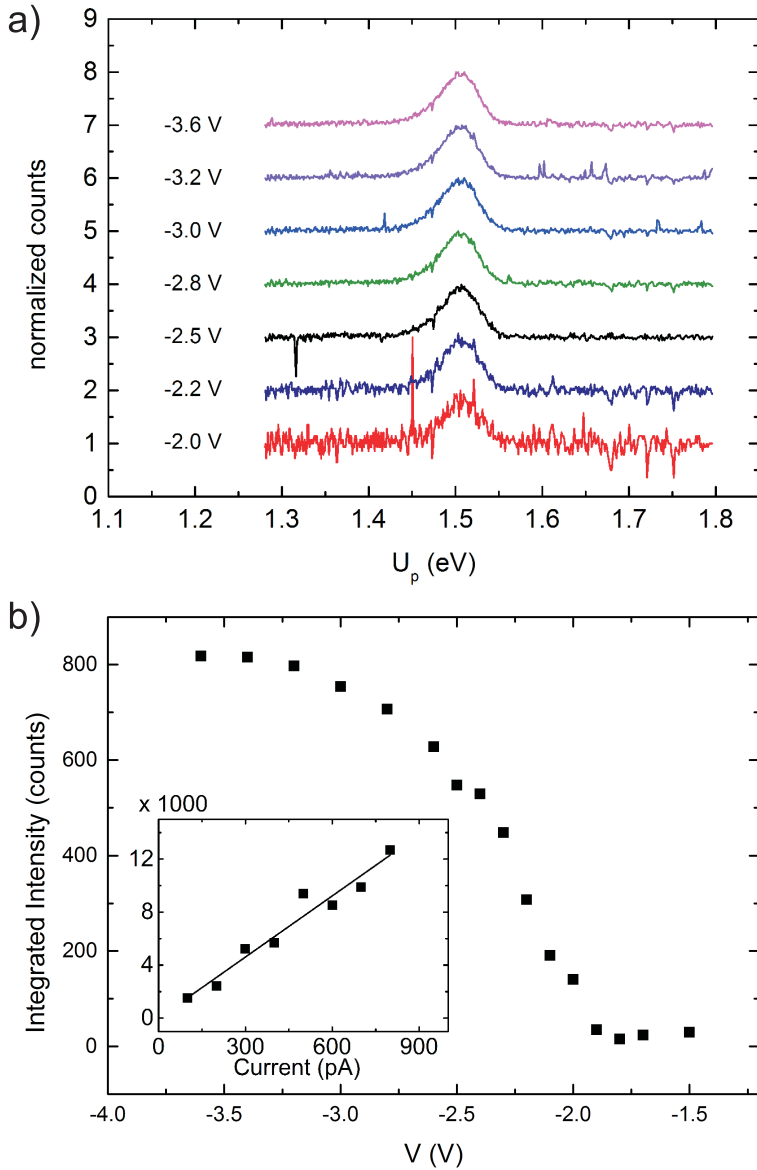
Figure 7.1: (a) STL spectra on n–type GaAs for different voltages normalized to their peak intensity, not smoothed, $I = 800$ pA, $t_{int} = 5$ min. (b) The integrated luminescence intensity as a function of applied bias voltage, smoothed, $I = 800$ pA, $t_{int} = 5$ min. The inset shows the integrated luminescence intensity as a function of the tunneling current obtained with a different tip, fitted with a linear function, $V = -3.50$ V, $t_{int} = 2$ min.

n–type GaAs lattice is linked to the ratio between radiative and non–radiative tunneling channels. Although this model accurately explains the atomic–scale variation in the STL intensity and describes the effect of a Si donor below the surface, it does not properly account for the influence of both donor and acceptor atoms on the luminescence that we observe in our measurements. In the current work, we present a different explanation for the high lateral resolution in luminescence intensity. STL measurements were conducted on single Si donors and acceptors in GaAs. The luminescence intensity is shown to consistently depend on the tip–sample distance. Therefore we conclude that for a fixed tunneling current the change in accumulated charge carriers in the sample directly below the tip is responsible for the intensity variation in the STL signal. The proposed mechanism explains both the atomic–scale variation in the luminescence intensity as well as the influence from single dopant atoms.

The STL measurements were performed on {110} surfaces of GaAs wafers n–doped with $\sim 2 \times 10^{18}$ cm^{-3} Si. An Omicron LT–STM was used for the experiments, operated at $T = 5$ K. Polycrystalline W tips were electrochemically etched and further prepared under ultra–high vacuum (UHV) conditions. Luminescence from the sample surface is collected by a lens that is built into the vacuum, transmitted through an optical fiber that is located outside UHV to a monochromator and recorded by a liquid N_2 cooled Si CCD camera. The details of the STL setup are described in Sec. 2.4 and Ref. [47].

7.2   Si Dopants in GaAs

Spectra on n–type GaAs normalized to their peak intensity are shown in Fig. 7.1 (a) as a function of photon energy U_p, for a range of applied bias voltages. The STL peak appears at the bandgap of GaAs, which is $E_g = 1.52$ eV in the case of GaAs at $T = 5$ K. There is no variation in the spectral shape over the whole voltage range. However, the total integrated intensity of the spectra shows a clear increase for larger negative voltage, as is displayed in (b). From the spectra, first a background is subtracted, followed by the application of a smoothing function to filter out any cosmic ray–induced peaks in the photomultiplier voltage. Then a numerical integration is performed. The observed increase with voltage originates from the onset of electron–hole recombination, which can only occur if the minority holes are injected into the valence band of the n–type semiconductor. For bias voltages below the onset, the tunneling current primarily originates from electrons in the conduction band tunneling into the tip. In this case, we estimate the onset of recombination at $V = -1.80$ V. There is a large voltage range, roughly be-
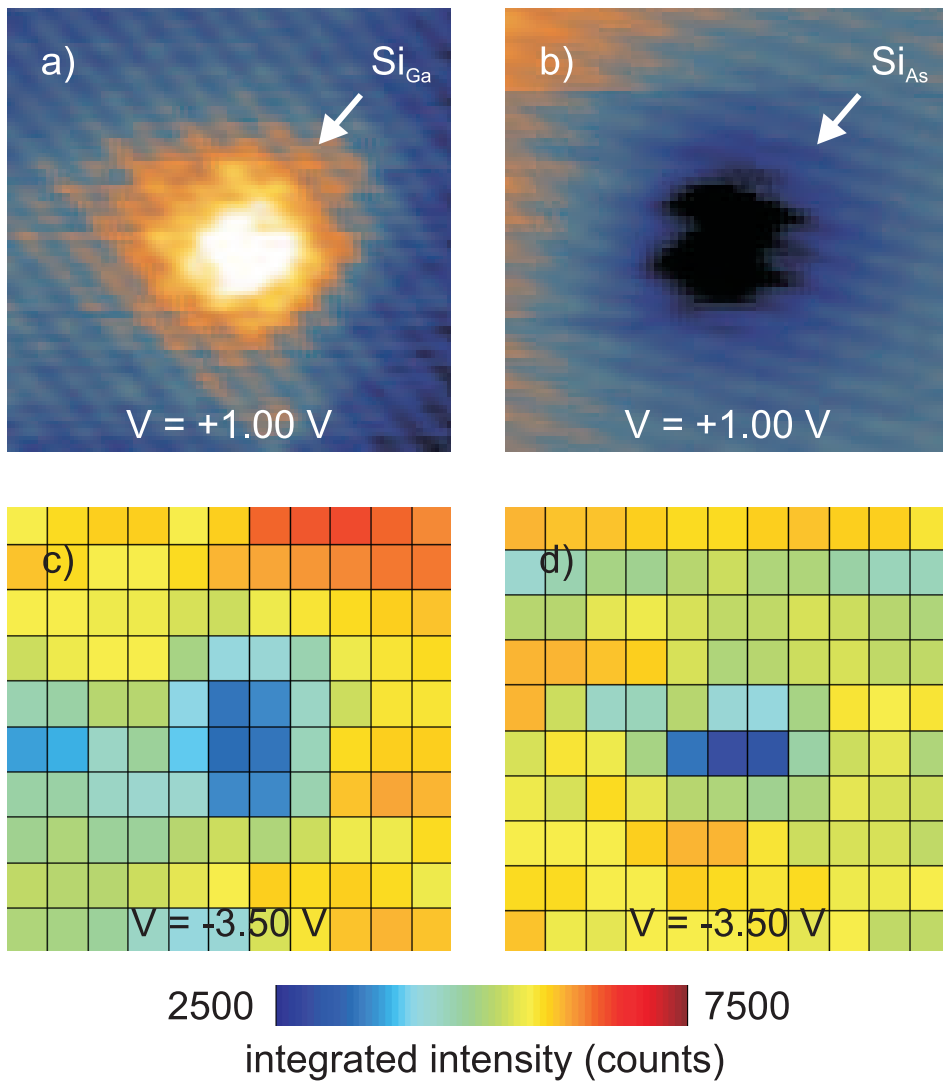
Figure 7.2: STM topography images of (a) a Si donor and (b) a Si acceptor in GaAs, 5×5 nm^2, $V = +1.00$ V, $I = 50$ pA. Integrated intensity maps of the corresponding STL signal for (c) the donor and (d) the acceptor, $V = -3.50$ V, $I = 800$ pA, $t_{int} = 42$ s.

tween $V = -1.80$ and -3.30 V, that shows a gradual increase of the STL intensity, until it reaches a stable plateau, similar to results in for example Ref. [132] and [133]. The rise is explained by the larger total energy range in the valence band that is accessible for the holes that are injected by the tip. For larger negative bias voltage, the contribution to the tunneling current from the accumulated electrons becomes smaller and that of the injected holes becomes larger. This means the local concentration of holes n_h is increased in the surface, allowing more recombination to take place. A plateau is reached for large negative voltage because then the current is dominated by the holes tunneling into the valence band and a further increase of the voltage does not introduce additional holes. The experimental data taken at a high negative bias voltage presented in the inset in (b) reveals that the STL intensity has a linear dependence on the tunneling current. This is because the rate of injected holes becomes larger for higher currents, resulting in more recombination.

The topography and the simultaneously recorded STL integrated intensity of a Si donor and a Si acceptor in n–type GaAs are presented as 2D maps in Fig. 7.2. The empty state topography images are recorded at a positive bias voltage and show a positively charged donor (a) and a negatively charged acceptor (b) giving rise to a dark and a bright contrast respectively. The variation in intensity of the STL signal in (c) and (d), at the same locations as (a) and (b) respectively, follows the extent of the dopant contrast in the surface. The luminescence intensity recorded on the dopants is roughly half compared to that on the surrounding GaAs and these changes occur within 1 nm. From the stronger contrast in the topography we deduce that the position of the donor in (a, c) is slightly closer to the surface layer than the acceptor in (b, d), which explains why the variation in STL intensity is weaker and more localized in the latter case. The experiment demonstrates that we can probe the optical properties of the surface and dopants with sub–nanometer resolution.

In Fig. 7.3 the STL integrated intensity is displayed taken over two line scans on GaAs intersecting with a Si donor in (a) and a Si acceptor in (b). The top of the figure shows the filled state topography image of the semiconductor. The green arrows indicate along which paths the STL spectra were taken. At the applied tunneling conditions, an elevation in the STM topography is visible for both the donor and the acceptor. The Si donor is neutral and has an additional state through which the charge carriers can tunnel. The Si acceptor is negatively charged, resulting in a Coulomb profile around the dopant. Both give rise to an enhanced topographic contrast in the surface [107], which means the STM tip retracts. We differentiate between the donor and acceptor
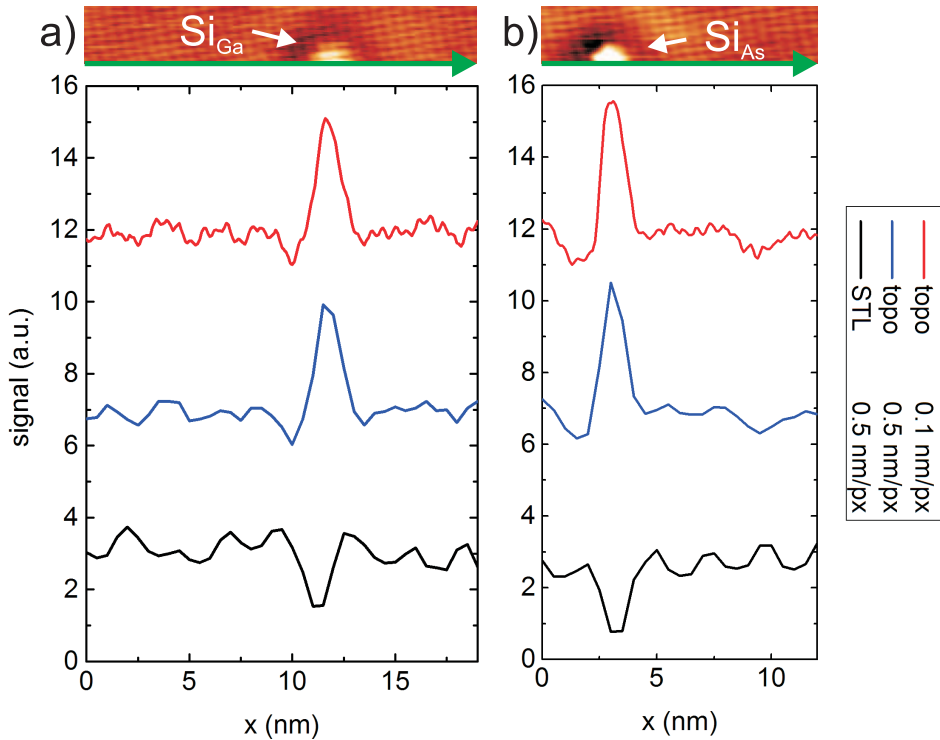
Figure 7.3: (top) STM topography images of GaAs with (a) a Si donor, 19×4 nm^2, and (b) a Si acceptor, 12×4 nm^2. The STL line trace are obtained over the indicated green arrows. (bottom) Line traces showing the topography (red), the same lines but using only the points where scanning was interrupted to collect the luminescence (blue) and the integrated STL intensity traces (black). $V = -3.00$ V, $I = 500$ pA, $t_{int} = 3$ min.

by measuring also at positive voltage (not shown), where donors appear bright and acceptors appear dark, see Fig. 7.2. Because the STL spectra were taken at every 5 points in the topography, a "reduced" lateral resolution height profile is shown that corresponds only to the points measured at those locations where the luminescence was recorded.

The fast and slow scan directions of the STM tip do not coincide exactly with the imaged crystal directions. This means that the atomic corrugations from both perpendicular crystal directions appear in the line trace of the full resolution line trace, one with a small sub–nm and the other with a few–nm periodicity. Only the larger–scale periodicity is visible in the reduced resolution line trace and the luminescence signal. Similar to Ref. [27], we observe an anti–correlation between the STL integrated intensity profile and the topography profile. In the STL signal, the two dopants both appear with a reduced luminescence intensity. The lateral extent of the variation in the local luminescence intensity is comparable to the contrast of the dopants that are visible in the topography.

7.3   Accumulated Charge Carriers

Based on our observations, in Fig. 7.4 we propose a model for the relevant processes for STL generation in the surface of an n–type semiconductor. The model is based on accumulated electrons in the sample surface below the STM tip, which are directly available for recombination with the injected holes. Electrons accumulate because at high enough negative bias voltage the local electric field of the STM tip results in a downward tip induced band bending (TIBB), see (a–b). A distinction between the two subfigures is made to differentiate between the situations where (a) the bias voltage is set to a value between the onset of recombination and the saturation plateau, visible in Fig. 7.1, and (b) to a value at the plateau, resulting in the maximum amount of electron–hole recombination. Together with the injected holes, accumulated electrons are responsible for the generated luminescence that is observed. We therefore assume the total STL intensity is a function that increases with the local concentrations of both holes and electrons, $f(n_h, n_e)$, integrated over the sample volume where the electrons are confined due to TIBB. If the bias voltage and tunneling current are kept constant, but the tip height changes during scanning, the luminescence intensity varies. This is because when the tip retracts due to a localized topographic feature, e.g. an increased local density of states (LDOS), the local TIBB decreases. The result is that less electrons accumulate in the surface below the tip and less electron–hole recombination takes place.
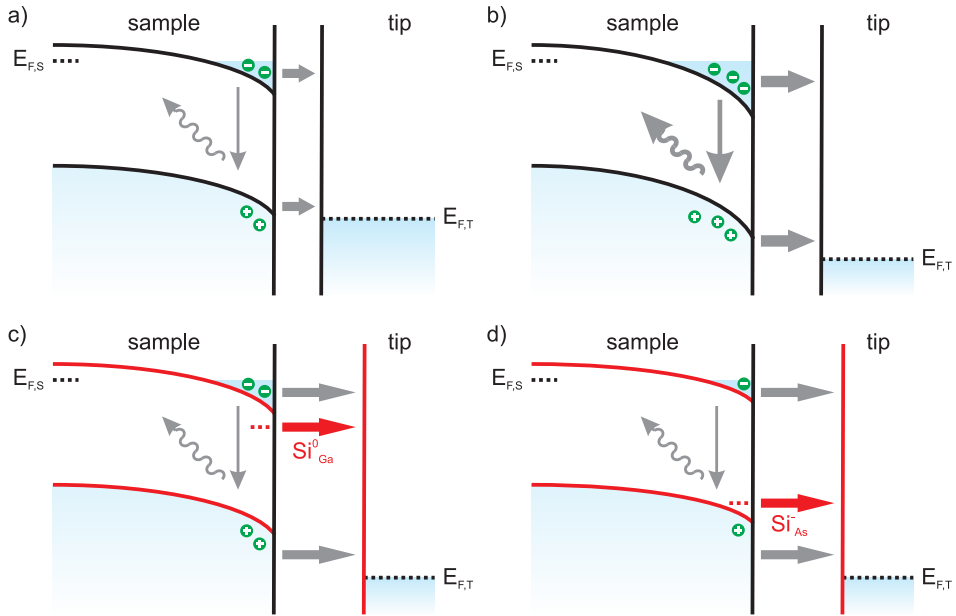
Figure 7.4: Relevant processes for the generation of a STL signal for (a–b) plain n–type GaAs, (c) a Si donor in the surface and (d) a Si acceptor in the surface. In (a) the bias voltage is set to a value between the onset of recombination and the saturation plateau visible in Fig. 7.1, while in (b) the bias voltage is set to a value at the plateau, resulting in the maximum amount of electron–hole recombination. The red color emphasizes the differences in (c–d) from the situation in (b). The additional tunneling channel provided by the dopant atoms lead to an increased tip–sample distance. As a result, the TIBB is reduced and less electrons accumulate near the sample surface, lowering the STL intensity. The horizontal arrows represent the tunneling paths for electrons. The arrows in the bandgap illustrate the recombination process.

The model we propose explains the observations on the dopant atoms. In Fig. 7.3 the topographic line trace reveals that both the donor and acceptor Si appear bright at high negative voltage, related to the enhanced LDOS at the location of the dopants. This results in a retraction of the tip, which leads to a reduced number of total accumulated electrons near the surface, see Fig. 7.4 (c–d), limiting the STL signal when tunneling on the donor and acceptor. At the applied tunneling conditions, the donor is neutral most of the time and the acceptor is primarily negatively charged, because the Fermi energy of the bulk semiconductor is higher than the dopant levels that are bended downwards near the surface. The negatively charged acceptor therefore has a Coulomb field around it, locally bending the bands back up a bit and further reducing the STL intensity. Moreover, the dependence on accumulated electrons also explains the atomic corrugation that is visible in the STL intensity. Similar to the dopant atoms but now on a smaller height scale, an anti-correlation between topography and STL intensity is present in the atomic corrugation. This is because less accumulated electrons are available for recombination with injected holes when the STM tip is on top of an As atom, when it is slightly higher than on top of a Ga atom.

An observation that supports our model of accumulated charge carriers is visible in the spectra displayed in Fig. 7.1 (a). The luminescence peak has its maximum at the bandgap energy, but broadens roughly 100 meV towards lower energies and 50 meV towards higher energies. We correlate the large low-energy tail with the Franz-Keldysh effect, which promotes below-bandgap excitation when an electric field is applied, similar to what is described in Sec. 5.3. The TIBB allows charge carriers that are slightly spatially separated to recombine at lower energies. This means that the electrons close to the surface can recombine with the holes deeper down. The high-energy tail can be explained by considering recombination between injected holes and accumulated electrons higher in the conduction band.

The model we put forward differs from that proposed in Ref. [27]. They connect the atomic resolution in the STL intensity to the ratio between the two main tunneling channels. The accumulated electron current from the conduction band results in a non-radiative path for the charge carriers and the injected hole current into the valence band constitutes a radiative tunneling channel. On the atomic Ga site, due to the empty dangling bonds, the conduction band current is considered to be dominant, which reduces the STL signal. On the atomic As site, the filled state current connected to the valence band contributes more, which results locally in a higher integrated intensity. Although their model explains the atomic corrugation in the STL intensity, it can not account for the dip we observe around a Si acceptor. Our model
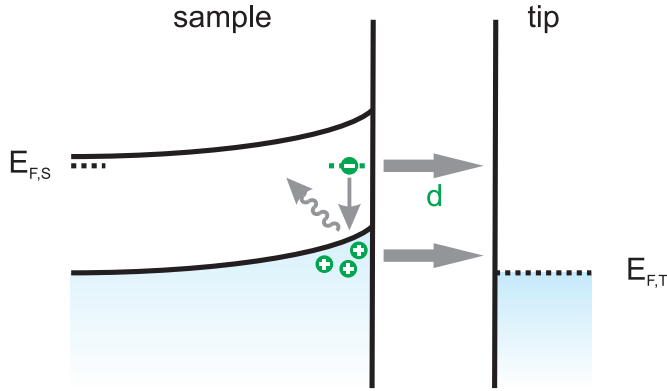
Figure 7.5: Relevant processes for the generation of a STL signal optimized for detecting the luminescence from a donor in the surface. This situation is created by choosing a tip made from a material with a large work function, e.g. Ni or Ir. The horizontal arrows represent the tunneling paths for electrons. The arrows in the bandgap illustrate the recombination process.

relates the total amount of accumulated charge carriers to the luminescence intensity and can in this way explain all the experimental observations.

Our observations and model suggest that the STL signal originates from a small sample volume directly below the tip and therefore contains optical information at the nm scale. In this study we have not observed any variation in the spectral information while scanning over the surface and the dopant atoms. However, in previous studies on QDs, STL emission from nanoscale structures was recorded spectrally [130, 49, 131]. Further investigations of single dopant atoms in semiconductors with STL should reveal whether local spectral information can indeed be obtained on the atomic scale. To optimize the luminescence intensity coming from a single dopant, the local minority carrier concentration should be enhanced. For example in the case of a donor, this could be accomplished by creating positive band bending conditions at negative bias voltage. The situation is illustrated in Fig. 7.5. The injected holes accumulate in the the neighborhood of the dopant atom directly below the tip, increasing the chance at recombination with an electron occupying the donor. Furthermore, the accumulation of electrons in the conduction band is suppressed, meaning the luminescence is mainly generated on the donor. Important here is that the donor level should be equal to or lower than the Fermi energy of the sample and the valence band onset at the surface should be equal to or higher than the Fermi energy of the tip. For this purpose, a tip with a large work function could be employed, for example made from Ni

or Ir [134]. Similarly, for an acceptor, negative band bending conditions at positive bias voltage would enhance the STL signal from that single dopant, for which tips with a small work function are preferred, for example made from Ag.

7.4 Conclusion

In summary, we have investigated the STL signal from an n–type GaAs surface and the effect of single dopants. The integrated intensity of the luminescence varies on the atomic scale, which can be attributed to the accumulation of charge carriers in the sample surface below the STM tip. At negative bias voltage, both Si donors and acceptors introduce protrusions in the topography, which means the STM tip slightly retracts in the case of constant current. Therefore, this reduces the amount of accumulated electrons available for recombination, which leads to a lower STL signal at the location of the dopants. Although these are in principle electronic effects related to the tunneling process, the luminescence signal originates from the local TIBB volume and therefore the technique can potentially be used to probe the optical properties of single dopants in semiconductors.

Electronic and Magnetic Properties of MnAs/GaAs Nanoclusters

In this chapter, the electronic and magnetic properties of MnAs nanoclusters in GaAs are investigated with cross-sectional scanning tunneling microscopy (X-STM). Together with structural information about the nanoscale clusters, this technique provides information about the local density of states (LDOS) and reveals the metallic character of MnAs in GaAs. When the bandgap of an cluster is probed with spectroscopy, a Coulomb blockade effect is observed that correlates with the size of the cluster. The smaller islands exhibit super-paramagnetic switching between two distinct magnetic states at $T = 77$ K, while the larger islands do not change their magnetic state and therefore are superferromagnetic at this temperature. This is demonstrated using antifer-romagnetic Cr tips to conduct spin-polarized (SP-)STM.

8.1 Introduction

Dilute magnetic semiconductors such as (Ga,Mn)As are interesting candi-dates for providing room-temperature ferromagnetism [135, 136, 137, 138]. However, these materials have only been grown with a Curie temperature up to $T_C = 185$ K [139], which is still far below room-temperature. An alterna-tive approach is the use of nm-sized ferromagnetic islands in a semiconductor host, e.g. MnAs nanoclusters in GaAs [140, 141]. This material has recently been demonstrated to be ferromagnetic well above room-temperature [142] and the MnAs clusters have been shown to exhibit metallic behavior [143]. In this work, the aim is to investigate the MnAs nanoclusters in detail with X-STM and confirm their metallic and magnetic properties at the nanoscale.

For this purpose, the electronic band structure and the magnetic switching of single MnAs clusters are probed with X–STM.

The samples for X–STM were grown by molecular beam epitaxy (MBE) by D. W. Rench at Penn State University. On a [001] oriented n–doped GaAs substrate, first a 100 nm Be-doped buffer layer was grown, with a Be concentration of around $\sim 1 \times 10^{18}$ cm^{-3}. This is followed by a low-temperature 120 nm Be:Ga$_{1-x}$Mn$_x$As layer grown at $T = 245$ °C. The final 2 nm high–temperature capping layer consists of Be:GaAs and is grown at $T = 600$ °C. We note here that the Be effusion cell temperature used for the low–temperature Be:Ga$_{1-x}$Mn$_x$As layer was 40 °C higher than that used for the high–temperature buffer and capping layers. This was done to keep the carrier concentration in all layers as similar as possible by compensating for the known double–donor effect caused by As anti–sites in low–temperature (Ga,Mn)As [144]. The last annealing step is crucial for obtaining the MnAs nanoclusters and the desired magnetic behavior. The high temperature favors the migration of Mn atoms away from interstitial and substitutional sites to be incorporated into the clusters as MnAs.

As outlined in Ref. [142], depending on the Mn concentration, the samples exhibit different magnetic behavior that can be linked to the size of the clusters. For a low Mn concentration of $x \leq 7.5$ %, the cluster diameters are small, ~ 6 nm, and have a zinc–blende crystal phase like the surrounding GaAs. The material has a low blocking temperature of $T_B = 10$ K. The blocking temperature characterizes the magnetic transition between two cluster states, i.e. superparamagnetism (the clusters are small ferromagnets, but they have a random magnetic moment orientation with respect to each other) and superferromagnetism (the ferromagnetic clusters have the same magnetic moment orientation). The high Mn concentration $x > 7.5$ % material contains the same small clusters, but also larger–sized clusters with diameters of roughly ~ 25 nm, that have a hexagonal NiAs crystal phase. T_B is well above room–temperature in this case. In the X–STM sample, $x = 7.5$ %, which puts the average cluster size and the magnetic character of the material in between the two types.

The X–STM measurements were performed on {110} GaAs surfaces in an Omicron LT–STM at $T = 77$ K operated under ultra–high vacuum (UHV) conditions with a base pressure of $p \leq 3 \cdot 10^{-11}$ mbar. The tips were prepared each starting from a thin Cr rod that was electrochemically etched to obtain an atomically sharp apex. The tips were subsequently prepared in UHV by heating and Ar sputtering to remove contaminants and create more stability during measurements. Cr is antiferromagnetic, which makes tips of this material ideal for SP-STM, because they do not have a stray magnetic
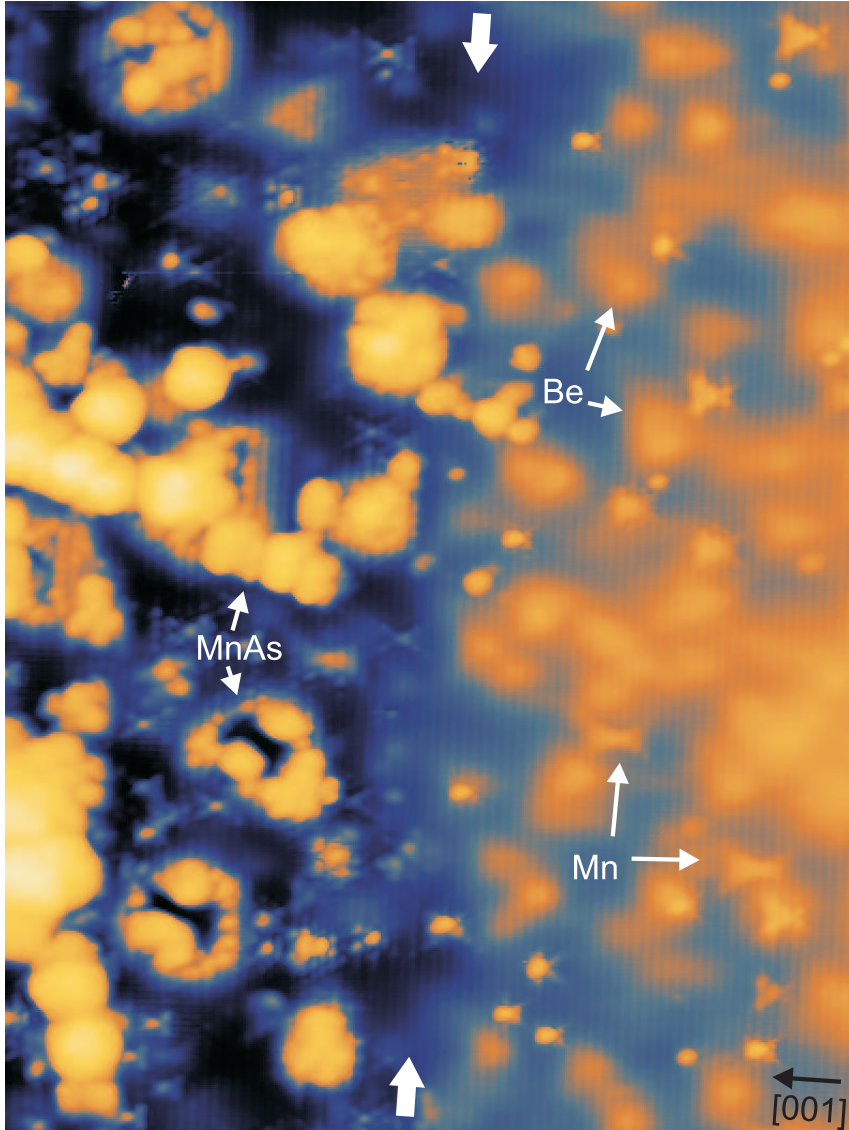
Figure 8.1: 40×53 nm^2 X-STM topography of MnAs nanoclusters in GaAs, $V = +1.25$ V, $I = 100$ pA. Two large white arrows indicate the boundary between the Be-doped buffer layer and the Be:Ga$_{1-x}$Mn$_x$As layer. Typical example of Be, Mn and MnAs are indicated by the small white arrows. The growth direction is represented by the small black arrow.
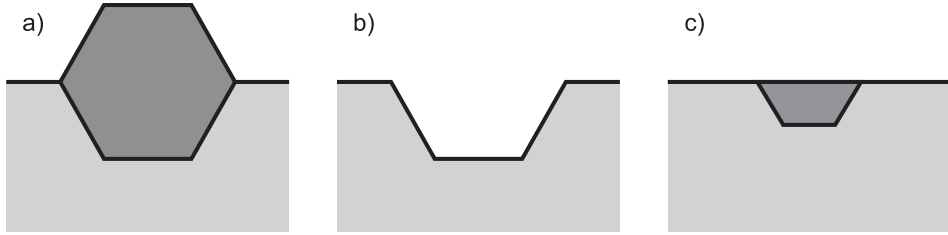
Figure 8.2: Illustration of the MnAs clusters in GaAs after the cleaving process. Large clusters with the hexagonal NiAs crystal phase either (a) are left behind protruding from the surface or (b) are ripped out of the surface. (c) Small clusters with the zinc–blende crystal phase cleave along a {110} plane lined up with the surrounding GaAs.

field but still show good magnetic sensitivity [76, 77]. The electronic measurements of the band structure were performed by directly taking IV–curves on the sample surface. The observations of magnetic switching were enabled by using a Ametek 5210 Dual Phase lock–in amplifier to obtain high–quality dI/dV information to probe the LDOS of the sample surface at a specific bias voltage.

8.2   Structural Analysis

In Fig. 8.1 a typical X–STM topography map is depicted of MnAs clusters in GaAs, grown on top of the Be–doped buffer layer. The chosen bias voltage of $V = +1.25$ V clearly reveals the difference between Be and Mn dopants. The Be appear as faint triangular shapes [55], while the Mn shows up as bow–tie or crab–like features [17]. Compared to (Ga,Mn)As layers grown under similar conditions, there are less As_{Ga} antisites present in the material [145]. The Mn wavefunctions are more cross–like when they sit close to a MnAs cluster, which probably relates to the Fermi level position in the GaAs host [146, 147].

The MnAs clusters give rise to both bright and dark contrasts with respect to the GaAs lattice. Because the metallic character corresponds to a good electrical conductivity, the MnAs appears brighter than the GaAs semiconductor in X–STM measurements. Besides that, in the case of the large–sized clusters both protrusions and depressions arise because material is either left behind on or ripped out of the surface during the cleaving process, see Fig. 8.2 (a–b) [148]. This occurs for example in areas where the crystal orientations of the materials do not match, as is expected for the MnAs in their hexagonal NiAs crystal phase. There is little outward relaxation visible in the
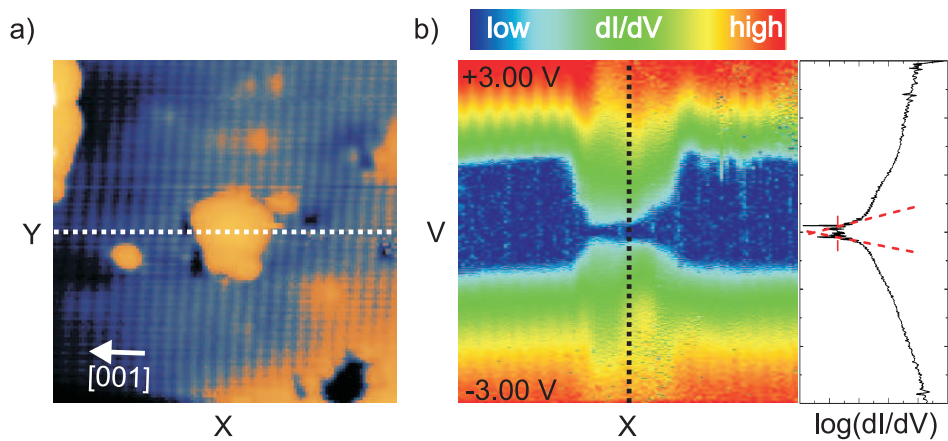
Figure 8.3: (a) 12×12 nm^2 X–STM topography of a nanoscale MnAs cluster in GaAs, $V = -3.00$ V, $I = 100$ pA. The white arrow indicates the growth direction. (b) An IV–spectroscopy line spectrum, taken over the dashed white line indicated in the topography, 10 mV steps. The dI/dV is color–coded from blue (low) to red (high). The single dI/dV–spectrum is taken at the position indicated by the dashed black line and is displayed on a semi–logarithmic scale. The estimation of the bandgap is indicated by the dashed red lines.

GaAs directly surrounding the clusters, from which we conclude that there is a low amount of strain between the two materials. The combination of different crystal structures and low strain suggests a mechanical decoupling of GaAs and MnAs in the case of the large–sized clusters. Furthermore, neither structural defects in or near the MnAs material nor lattice deformations are visible, indicating that full relaxation occurs at the interfaces. For the small–sized clusters, in some cases the zinc–blende crystal lattice structure is visible also in the MnAs and no protrusions or depressions related to the cleaving process are observed, see Fig. 8.2 (c). From Ref. [142] the zinc–blende phase is expected to arise in the smaller nanostructures, which matches with the trend observed in the 2 μm long interface region that was imaged by X–STM. The larger clusters do not show atomic corrugation and also appear with larger height variations. We therefore assume that these larger clusters have the hexagonal NiAs phase.

8.3 Electronic and Magnetic Properties

In Fig. 8.3 the electronic band structure of a MnAs nanocluster is compared to the surrounding GaAs by plotting the dI/dV along the dashed white line visible in the corresponding topography image. The measurements were performed on a sample with a Mn concentration of $x = 7.5$ %. At the applied tunneling conditions, the contrast from electronic effects is suppressed in the height profile of the surface. This setting is therefore an appropriate starting condition for IV-spectroscopy, because it avoids cross–talk with the topography. Although MnAs is metallic, the nm size of the clusters results in a Coulomb blockade effect with an effective energy gap due to the charging of the cluster [143]. From the spectroscopic data, the charging energy can be estimated by intersecting the valence and conduction band edges with the electrical noise level on a semi–logarithmic scale. The charging energy of MnAs, $E_g = 0.20$ eV, is much smaller than the bandgap of GaAs, $E_g = 1.52$ eV. The electrostatic energy of a nanocapacitor is $e^2/2C$, where the capacitance is given by $C = 4\pi\epsilon_0\epsilon R$, with ϵ_0 the vacuum permittivity and $\epsilon = 1$ the relative permittivity. The radius of the nanocluster is approximated at $R = 3.6$ nm, which matches well with the size observed in the topography measurement. Note that the value for ϵ takes into account only the MnAs–vacuum interface, while the effect of the GaAs host is neglected. Furthermore, the STM electronic noise level of ~ 1 pA results in a possible overestimation of the charging energy. The uncertainties in these two parameters have opposite effects: a larger effective ϵ decreases the estimated radius, while a lower STM electronic noise level could increase it.
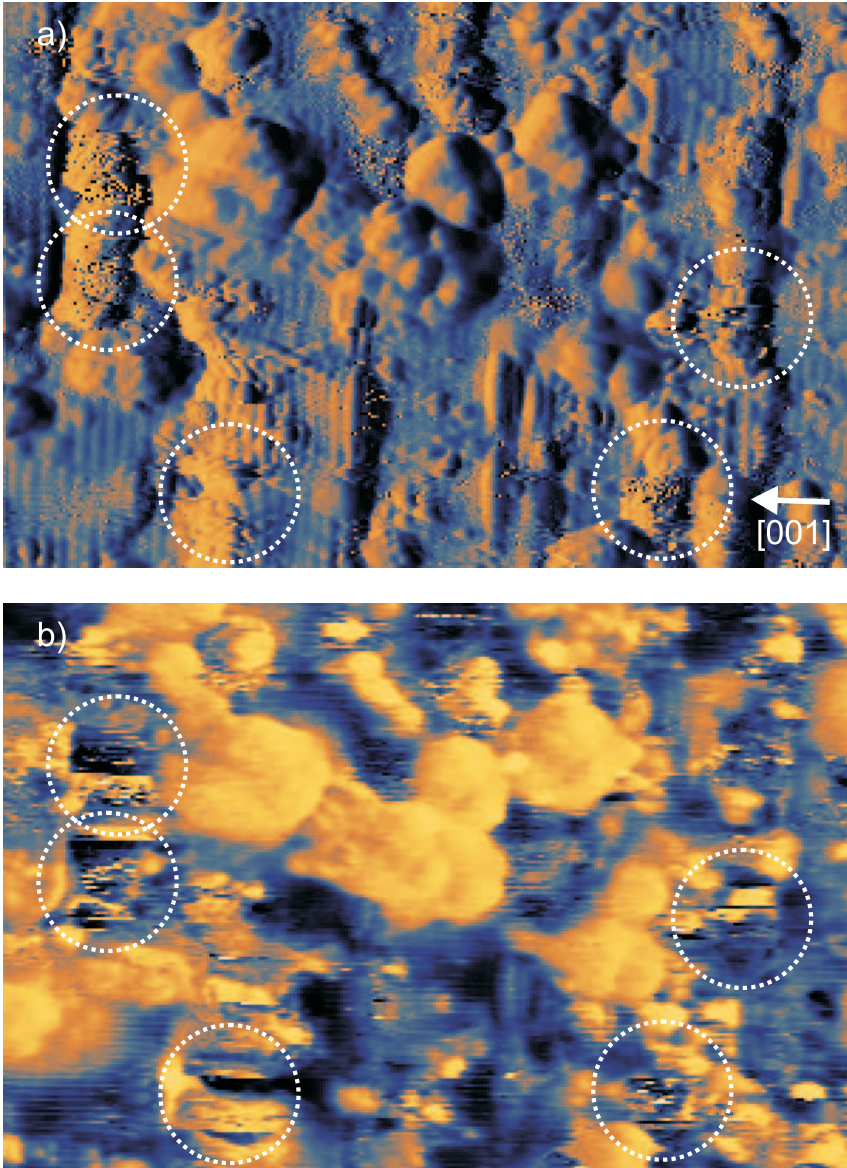
Figure 8.4: 30×20 nm^2 maps of (a) current and (b) dI/dV of switching MnAs clusters in GaAs, $V = +1.25$ V, $I = 100$ pA, $V_{osc} = 35$ mV, $f_{osc} = 858$ Hz, $\tau_{osc} = 3$ ms. The fast scan direction is left to right, the slow scan direction is bottom to top. The white arrow indicates the growth direction. The dotted white circles indicate the position of switching clusters.
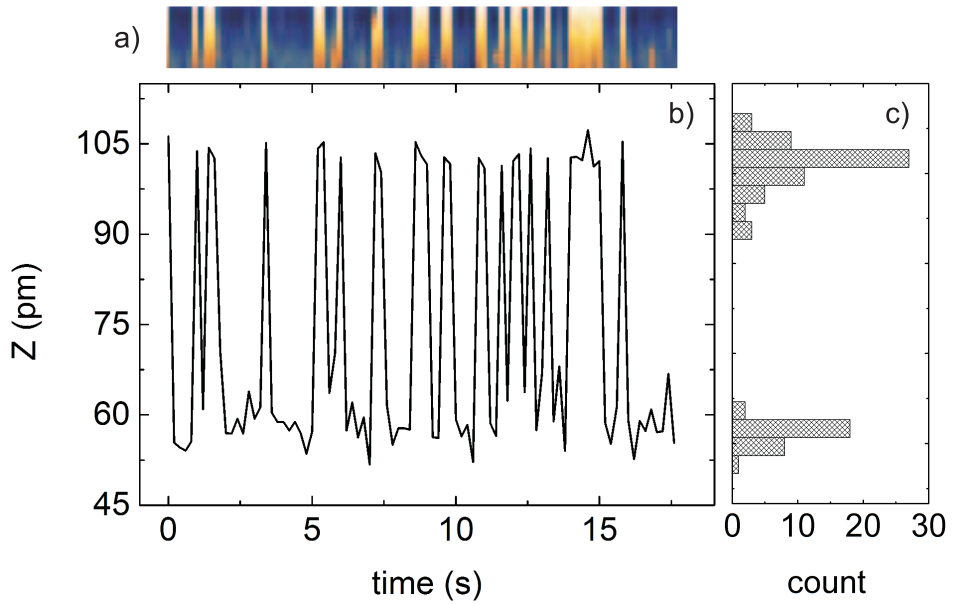
Figure 8.5: The graph shows the random telegraph noise signal of a MnAs nanocluster in GaAs, $V = +1.75$ V, $I = 25$ pA. The corresponding 2 nm wide part of the topographic line trace is displayed on top. On the right, a histogram is shown of the tip height distribution during this measurement recorded in time, demonstrating the switching between two distinct states.

The spin–polarized Cr tips that are used in the X–STM measurements have a magnetic sensitivity that is most apparent when recording dI/dV spectra. The switching of a MnAs cluster between two magnetizations is displayed in Fig. 8.4. Because the current in this STM measurement is constant, only large abrupt changes are recorded in the signal, because in that case the feedback is too slow to adjust the tip height immediately. In our measurement we observe a strong instability in the current at the position of the smaller–sized clusters. In the dI/dV signal these regions correspond to areas where two distinct contrasts are observed. The signal switches between a dark and a bright contrast at random positions during scanning with the tip, similar to the bistability of the Si charge state in the GaAs surface observed in Chap. 5 and 6.

We argue that the two states in the dI/dV map correspond to two magnetic moments of the cluster, both along its magnetic easy axis but with opposite sign. The bistability originates from the magnetization reversal of a complete cluster, similar to Co islands on a Cu surface described in Ref. [74]. In (Ga,Mn)As samples, resistance noise measurements have been shown to exhibit random telegraph noise, corresponding to MnAs clusters with a magnetic moment of $m \sim 20\mu_B$ [149]. The magnetization direction of the magnetic cluster is more parallel to that of the tip apex in the case of the bright contrast, and more anti–parallel when a dark contrast is observed [22]. The switching occurs only for the smaller sized clusters, while the larger clusters remain stable. This suggests that the smaller clusters are superparamagnetic and do not contribute to the ferromagnetic state of the material. The larger clusters are not switching, suggesting superferromagnetic behavior under these conditions. This corresponds to the observations in Ref. [142], where the measured blocking temperature for material with on average smaller clusters is $T_B = 10$ K and that for material with on average larger clusters is above room–temperature. We chose the experimental temperature of $T = 77$ K in the X–STM measurements to verify the different magnetic behavior for the smaller and larger nanoclusters.

The magnetic sensitivity is most apparent in the dI/dV signal, but also translates into changes in the topography. Random telegraph noise of a single switching cluster observed in the topography is shown in Fig. 8.5. In this experiment, the tip was restricted to scan over a single line of 10 nm wide repetitively. From the resulting data set, the tip height in the center of a MnAs cluster is extracted as a function of time. The relative tip–sample distance for the two magnetic states with these tunneling conditions is on the order of 50 pm, which is well above the electrical and vibrational noise level of about 5 pm. A detailed study of the dynamical behavior of the switching

is possible by varying the tunneling conditions, similar to that performed in Chap. 6, but this is outside of the scope of this work.

8.4   Conclusion

MnAs nanoclusters in GaAs represent a material that has interesting magnetic properties. The Coulomb blockade effect observed in a small cluster matches with the size of the cluster and confirms the metallic character. The SP–STM measurements reveal that the smaller clusters switch between two distinct magnetic states, which means that they are superparamagnetic at $T = 77$ K, while the larger clusters do not switch and are superferromagnetic. This supports the view that larger sized clusters are needed to create stable ferromagnetism at room–temperature.

Chapter 9

Outlook

This thesis focuses on various nanostructures and dopants in GaAs that were probed with scanning tunneling microscopy (STM). This chapter is aimed at giving a short overview of the work that has been done and what possible future experiments could be performed.

GaSb QDs in a GaAs host are discussed in Chap. 3 and 4. It is shown that depending on the exact growth conditions, the nanostructures remain pure and intact during overgrowth or they are disintegrated into various shapes upon capping. Although good quality QDs can be achieved using the right growth conditions, the challenge that remains is to improve the hole localization energy even further to aid the development of opto-electronic devices like flash memory and solar cells. In this thesis a first step in this direction is taken by studying the nanostructures capped with various Al-rich materials. The Al has a double advantage. First of all, it successfully protects the GaSb nanostructures during capping, which leads to more intact QDs in the final material. Also, the band gap of AlGaAs is larger than that of GaAs, effectively increasing the hole localization barrier. However, as it turns out, the high amount of strain in the material, which is no longer driving the disintegration, now results in stacking faults around the nanostructures. These structural defects degrade the optical quality of the material and should thus be avoided. A solution for this might be the growth of smaller QDs, reducing the associated strain and preventing the formation of the stacking faults. Another approach to limit strain would be to grow intermixed GaAsSb dots or to mix in some Sb in the capping layer. STM could, similar to the work in this thesis, be a helpful tool to determine the morphology of these nanostructures and reveal what is going on at the atomic scale.

The bistable behavior of the Si charge state in the surface layer of GaAs

(110) is treated in Chap. 5 and 6. The optical switching of the dopant atom from negative to positive occurs because of recombination between the bound electrons with photoexcited holes. The possibility for electrons to escape or be captured is an important aspect of the switching mechanism. Therefore, the switching dynamics were studied to investigate these processes in more detail. The lateral position of the tip, the bias voltage and the tunneling current all influence the switching frequency and charge state occupation. A physical model taking into account the relevant tunneling barriers can explain the observed phenomena. As a further investigation, a study of different dopant atoms in various host materials could be done to show the generality of the bistable switching at the surface. Similar to the DX^- center, the expected bistable behavior arises typically when a highly localized deep state, associated with a lattice relaxation, sits in energy below a more delocalized shallow state, with the dopant on a substitutional site. Examples are the donors Te in GaAsP, S in GaInP and Te in AlGaSb, but there are many others [150]. Various dopants with a DX^-–like state at the surface could be compared to confirm the physical principles observed and modeled in this thesis. Furthermore, as the energy barrier can be rather different for each of these systems, it might allow the switching to occur on much faster or slower timescales, which is interesting for possible device applications. Another idea is to position Si dopants with the STM tip to form simple logical structures, for example a NOR or a NAND gate, illustrated in Fig. 6.8, to demonstrate the combined functional use of multiple dopant atoms in devices. The dopants could be deposited on the surface by means of an evaporation cell that was installed recently in our low–temperature STM. Manipulation with the tip could then provide the positioning and embedding of dopants in the surface, allowing the construction of ordered structures with multiple dopants.

In the optical absorption experiments discussed in Chap. 5, the tip in–duced band bending (TIBB) was not affected by the laser illumination. This was checked by looking at the extent of the charge disks of Si donors for a range of laser powers, which did not change during the experiment. The effect of illumination on the TIBB is inversely proportional to the doping den–sity, which is a relatively high $\sim 2 \times 10^{18}$ cm^{-2} in this case. Samples with a lower doping concentration clearly show a shift in I(V) curves under illumi–nation (measurements not shown), which relates directly to the presence of a photovoltage [50]. We expect that this effect might be a useful tool to de–termine the TIBB at the surface more accurately than other purely electronic methods can do [67, 68]. An experiment that can be done is to stop the current feedback loop of the STM and illuminate the sample with a laser pulse, while recording the tunneling current. The photoexcited carriers create a photovolt–

age, which compensates the TIBB at the surface. This means that a positive contribution of the light to the tunneling current indicates that there is a negative TIBB at the surface and vice verse. A measurement for a range of bias voltages and laser powers would therefore give a fairly accurate ~ 10 meV estimate of the flatband condition of the tip–sample system. It is therefore a potential method to determine the TIBB with a similar precision, which is often a much more uncertain quantity in many STM experiments. The pulsed laser approach is preferred, to limit as much as possible any heating effects of the sample because of illumination. Of course, a relatively low–doped sample is needed for this measurement, which might not be practical for all STM experiments.

In the experiments outlined in Chap. 7, scanning tunneling luminescence (STL) is employed to map out the effects of single dopants and atomic corrugation on the integrated intensity of the optical spectra. The variation can be understood in terms of accumulated charge carriers of which the volume and density changes with the variation in topographic height and thus the associated TIBB. As a next step, the spectral signatures of single nanostructures and dopants could be investigated with STL on cross–sectional surfaces. For this to work, it is important that the luminescence originating from these structures is dominant over that from the surrounding host material. This was not the case in the experiments presented in this thesis, or in other words no difference is observed between the spectra other than their total integrated intensity. A solution for improving this is the application of tips with a different work function, illustrated in Fig. 7.5, reversing the sign of the TIBB for the same tunneling condition compared to the W tips. This in principle favors the recombination with the minority charge carriers in the nanostructures or dopants instead of with the majority charge carriers in the host material, because the latter experience Coulomb repulsion in the area. It might be that the recombination rate from nanoscale systems alone is too low to be recorded by the LN–cooled Si detector, but even a factor of 10 lower in total intensity would still be measurable. A successful measurement would allow access to spectral information on the atomic scale.

Metallic MnAs nanoclusters in GaAs are the topic of Chap. 8. Electronic dI/dV measurements with scanning tunneling spectroscopy (STS) reveal that a single MnAs island has a small bandgap. This can be understood from the Coulomb charging of the nanostructure, effectively creating an energy cost for charge carriers to tunnel into the island. The observed bandgap nicely corresponds with the radius R of the nanocluster. The magnetic state of MnAs nanoclusters can be reversed through the injection of current by an STM tip, which was shown with spin–polarized (SP–)STM. Further work

could be done on measuring the bandgap of several MnAs nanoclusters to quantitatively show the $1/R$ correlation between bandgap and radius, giving more information about the local electronic structure of the material. Also, the dynamics of the magnetic state of single MnAs nanoclusters could be studied, similar to what is done in Chap. 6, to observe the typical time–scales of the bistable behavior and to correlate the switching frequency to the size of the islands.

Bibliography

[1] R. P. Feynman, "There's Plenty of Room at the Bottom." APS lecture, 1959.

[2] G. E. Moore, "Cramming more components onto integrated circuits," *Electronics*, vol. 38, no. 8, p. 114, 1965.

[3] G. Binnig, H. Rohrer, C. Gerber, and E. Weibel, "Surface studies by scanning tunneling microscopy," *Phys. Rev. Lett.*, vol. 49, p. 57, 1982.

[4] G. Binnig, H. Rohrer, C. Gerber, and E. Weibel, "7 × 7 Reconstruction on Si(111) resolved in real space," *Phys. Rev. Lett.*, vol. 50, p. 120, 1983.

[5] D. M. Eigler and E. K. Schweizer, "Positioning single atoms with a scanning tunneling microscope," *Nature*, vol. 344, p. 524, 1990.

[6] R. Nötzel, "Self-organized growth of quantum-dot structures," *Semicond. Sci. Technol.*, vol. 11, no. 10, p. 1365, 1996.

[7] R. J. Warburton, "Self-assembled semiconductor quantum dots," *Contemp. Phys.*, vol. 43, no. 5, p. 351, 2002.

[8] P. M. Koenraad and M. E. Flatté, "Single dopants in semiconductors," *Nat. Mater.*, vol. 10, no. 2, p. 91, 2011.

[9] A. Heinrich and S. Loth, "A logical use for atoms," *Science*, vol. 332, no. 6033, p. 1039, 2011.

[10] M. Fuechsle, J. Miwa, S. Mahapatra, H. Ryu, S. Lee, O. Warschkow, L. C. L. Hollenberg, G. Klimeck, and M. Y. Simmons, "A single-atom transistor," *Nat. Nanotechnol.*, vol. 7, p. 242, Feb 2012.

[11] J. Verduijn, G. C. Tettamanzi, and S. Rogge, "Wave function control over a single donor atom," *Nano Lett.*, vol. 13, no. 4, p. 1476, 2013.

[12] D. M. Bruls, J. W. A. M. Vugs, P. M. Koenraad, H. W. M. Salemink, J. H. Wolter, M. Hopkinson, M. S. Skolnick, F. Long, and S. P. A. Gill, "Determination of the shape and indium distribution of low-growth-rate InAs quantum dots by cross-sectional scanning tunneling microscopy," *Appl. Phys. Lett.*, vol. 81, no. 9, p. 1708, 2002.

[13] J. G. Keizer, J. Bocquel, P. M. Koenraad, T. Mano, T. Noda, and K. Sakoda, "Atomic scale analysis of self assembled GaAs/AlGaAs quantum dots grown by droplet epitaxy," *Appl. Phys. Lett.*, vol. 96, no. 6, p. 062101, 2010.

[14] J. G. Keizer, P. M. Koenraad, P. Smereka, J. M. Ulloa, A. Guzman, and A. Hierro, "Kinetic Monte Carlo simulations and cross-sectional scanning tunneling microscopy as tools to investigate the heteroepitaxial capping of self-assembled quantum dots," *Phys. Rev. B*, vol. 85, p. 155326, 2012.

[15] M. C. M. M. Van Der Wielen, A. J. A. Van Roij, and H. Van Kempen, "Direct observation of Friedel oscillations around incorporated Si_{Ga} dopants in GaAs by low-temperature scanning tunneling microscopy," *Phys. Rev. Lett.*, vol. 76, p. 1075, 1996.

[16] A. P. Wijnheijmer, J. K. Garleff, K. Teichmann, M. Wenderoth, S. Loth, R. G. Ulbrich, P. A. Maksym, M. Roy, and P. M. Koenraad, "Enhanced donor binding energy close to a semiconductor surface," *Phys. Rev. Lett.*, vol. 102, no. 16, p. 166101, 2009.

[17] C. Çelebi, J. K. Garleff, A. Y. Silov, A. M. Yakunin, P. M. Koenraad, W. Van Roy, J.-M. Tang, and M. E. Flatté, "Surface induced asymmetry of acceptor wave functions," *Phys. Rev. Lett.*, vol. 104, p. 086404, 2010.

[18] M. Bozkurt, M. R. Mahani, P. Studer, J.-M. Tang, S. R. Schofield, N. J. Curson, M. E. Flatté, A. Y. Silov, C. F. Hirjibehedin, C. M. Canali, and P. M. Koenraad, "Magnetic anisotropy of single Mn acceptors in GaAs in an external magnetic field," *Phys. Rev. B*, vol. 88, p. 205203, 2013.

[19] A. Marent, M. Geller, and D. Bimberg, "A novel nonvolatile memory based on self-organized quantum dots," *Microelectr. J.*, vol. 40, no. 3, p. 492, 2009.

[20] A. Marent, T. Nowozin, M. Geller, and D. Bimberg, "The QD-flash: A quantum dot-based memory device," *Semicond. Sci. Tech.*, vol. 26, no. 1, p. 014026, 2011.

[21] J. K. Garleff, A. P. Wijnheijmer, C. N. Van Den Enden, and P. M. Koenraad, "Bistable behavior of silicon atoms in the (110) surface of gallium arsenide," *Phys. Rev. B*, vol. 84, no. 7, p. 075459, 2011.

[22] R. Wiesendanger, H.-J. Güntherodt, G. Güntherodt, R. J. Gambino, and R. Ruf, "Observation of vacuum tunneling of spin-polarized electrons with the scanning tunneling microscope," *Phys. Rev. Lett.*, vol. 65, p. 247, 1990.

[23] A. A. Khajetoorians, B. Chilian, J. Wiebe, S. Schuwalow, F. Lechermann, and R. Wiesendanger, "Detecting excitation and magnetization of individual dopants in a semiconductor," *Nature*, vol. 467, p. 1084, 2010.

[24] R. Wiesendanger, "Single-atom magnetometry," *Curr. Opin. Solid State Mater. Sci.*, vol. 15, no. 1, p. 1, 2011.

[25] J. Gimzewski, B. Reihl, J. Coombs, and R. Schlittler, "Photon emission with the scanning tunneling microscope," *Z. Phys. B*, vol. 72, no. 4, p. 497, 1988.

[26] R. Berndt, R. Gaisch, W. D. Schneider, J. K. Gimzewski, B. Reihl, R. R. Schlittler, and M. Tschudy, "Atomic resolution in photon emission induced by a scanning tunneling microscope," *Phys. Rev. Lett.*, vol. 74, p. 102, 1995.

[27] M. Reinhardt, G. Schull, P. Ebert, and R. Berndt, "Atomic resolution in tunneling induced light emission from GaAs(110)," *Appl. Phys. Lett.*, vol. 96, no. 15, p. 152107, 2010.

[28] J. Bardeen, "Tunnelling from a many-particle point of view," *Phys. Rev. Lett.*, vol. 6, p. 57, 1961.

[29] J. Tersoff and D. R. Hamann, "Theory and application for the scanning tunneling microscope," *Phys. Rev. Lett.*, vol. 50, p. 1998, 1983.

[30] J. Tersoff and D. R. Hamann, "Theory of the scanning tunneling microscope," *Phys. Rev. B*, vol. 31, p. 805, 1985.

[31] C. Chen, *Introduction to scanning tunneling microscopy*. Oxford University Press, 1993.

[32] R. M. Feenstra and J. A. Stroscio, "Tunneling spectroscopy of the GaAs(110) surface," *J. Vac. Sci. & Technol. B*, vol. 5, no. 4, p. 923, 1987.

[33] A. P. Wijnheijmer, J. K. Garleff, M. A. Van Der Heijden, and P. M. Koenraad, "Influence of the tip work function on scanning tunneling microscopy and spectroscopy on zinc doped GaAs," *J. Vac. Sci. Technol. B*, vol. 28, no. 6, p. 1086, 2010.

[34] S. Loth, S. Baumann, C. P. Lutz, D. M. Eigler, and A. J. Heinrich, "Bistability in atomic-scale antiferromagnets," *Science*, vol. 335, no. 6065, p. 196, 2012.

[35] D. Kitchen, A. Richardella, J.-M. Tang, M. E. Flatté, and A. Yazdani, "Atom-by-atom substitution of Mn in GaAs and visualization of their hole-mediated interactions," *Nature*, vol. 442, no. 7101, p. 436, 2006.

[36] J. K. Garleff, C. Çelebi, W. Van Roy, J.-M. Tang, M. E. Flatté, and P. M. Koenraad, "Atomically precise impurity identification and modification on the manganese doped GaAs(110) surface with scanning tunneling microscopy," *Phys. Rev. B*, vol. 78, p. 075313, 2008.

[37] J. K. Garleff, M. Wenderoth, K. Sauthoff, R. G. Ulbrich, and M. Rohlfing, "2 × 1 reconstructed Si(111) surface: STM experiments versus ab initio calculations," *Phys. Rev. B*, vol. 70, no. 24, p. 245424, 2004.

[38] D. W. Pohl and R. Möller, ""Tracking" tunneling microscopy," *Rev. Sci. Instrum.*, vol. 59, no. 6, p. 840, 1988.

[39] M. J. Rost, L. Crama, P. Schakel, E. Van Tol, G. B. E. M. Van Velzen-Williams, C. F. Overgauw, H. Ter Horst, H. Dekker, B. Okhuijsen, M. Seynen, A. Vijftigschild, P. Han, A. J. Katan, K. Schoots, R. Schumm, W. Van Loo, T. H. Oosterkamp, and J. W. M. Frenken, "Scanning probe microscopes go video rate and beyond," *Rev. Sci. Instrum.*, vol. 76, no. 5, p. 053710, 2005.

[40] A. Van Houselt and H. J. W. Zandvliet, "Colloquium: Time–resolved scanning tunneling microscopy," *Rev. Mod. Phys.*, vol. 82, no. 2, p. 1593, 2010.

[41] S. Loth, M. Etzkorn, C. P. Lutz, D. M. Eigler, and A. J. Heinrich, "Measurement of fast electron spin relaxation times with atomic resolution," *Science*, vol. 329, no. 5999, p. 1628, 2010.

[42] I. Moult, M. Herve, and Y. Pennec, "Ultrafast spectroscopy with a scanning tunneling microscope," *Appl. Phys. Lett.*, vol. 98, no. 23, p. 233103, 2011.

[43] J. Schaffert, M. C. Cottin, A. Sonntag, H. Karacuban, D. Utzat, C. A. Bobisch, and R. Möller, "Scanning noise microscopy," *Rev. Sci. Instrum.*, vol. 84, no. 4, p. 043702, 2013.

[44] J. Schaffert, M. C. Cottin, A. Sonntag, H. Karacuban, C. A. Bobisch, N. Lorente, J.-P. Gauyacq, and R. Möller, "Imaging the dynamics of individually adsorbed molecules," *Nat. Mater.*, vol. 12, no. 3, p. 223, 2013.

[45] D. L. Abraham, A. Veider, C. Schönenberger, H. P. Meier, D. J. Arent, and S. F. Alvarado, "Nanometer resolution in luminescence microscopy of III-V heterostructures," *Appl. Phys. Lett.*, vol. 56, no. 16, p. 1564, 1990.

[46] S. F. Alvarado and P. Renaud, "Observation of spin–polarized–electron tunneling from a ferromagnet into GaAs," *Phys. Rev. Lett.*, vol. 68, p. 1387, 1992.

[47] J. G. Keizer, J. K. Garleff, and P. M. Koenraad, "Simple and efficient scanning tunneling luminescence detection at low–temperature," *Rev. Sci. Instrum.*, vol. 80, no. 12, p. 123704, 2009.

[48] M. Sakurai, C. Thirstrup, and M. Aono, "New aspects of light emission from STM," *Appl. Phys. A*, vol. 80, no. 6, p. 1153, 2005.

[49] S. E. J. Jacobs, M. Kemerink, P. M. Koenraad, M. Hopkinson, H. W. M. Salemink, and J. H. Wolter, "Spatially resolved scanning tunneling luminescence on self–assembled InGaAs/GaAs quantum dots," *Appl. Phys. Lett.*, vol. 83, no. 2, p. 290, 2003.

[50] S. Grafström, "Photoassisted scanning tunneling microscopy," *J. App. Phys.*, vol. 91, no. 4, p. 1717, 2002.

[51] R. M. Feenstra, J. A. Stroscio, J. Tersoff, and A. P. Fein, "Atom–selective imaging of the GaAs(110) surface," *Phys. Rev. Lett.*, vol. 58, p. 1192, 1987.

[52] G. J. De Raad, D. M. Bruls, P. M. Koenraad, and J. H. Wolter, "STM observations of GaAs(110) showing the top and bottom zig-zag rows of the surface," *Phys. Rev. B*, vol. 64, p. 075314, 2001.

[53] S. Y. Tong, A. R. Lubinsky, B. J. Mrstik, and M. A. Van Hove, "Surface bond angle and bond lengths of rearranged As and Ga atoms on GaAs(110)," *Phys. Rev. B*, vol. 17, p. 3303, 1978.

[54] M. D. Pashley, K. W. Haberern, R. M. Feenstra, and P. D. Kirchner, "Different Fermi–level pinning behavior on n- and p-type GaAs(001)," *Phys. Rev. B*, vol. 48, p. 4612, 1993.

[55] M. B. Johnson, O. Albrektsen, R. M. Feenstra, and H. W. M. Salemink, "Direct imaging of dopants in GaAs with cross-sectional scanning tunneling microscopy," *Appl. Phys. Lett.*, vol. 63, no. 21, p. 2923, 1993.

[56] P. Ebert, "Nano-scale properties of defects in compound semiconductor surfaces," *Surf. Sci. Rep.*, vol. 33, no. 4, p. 121, 1999.

[57] J. F. Zheng, X. Liu, N. Newman, E. R. Weber, D. F. Ogletree, and M. Salmeron, "Scanning tunneling microscopy studies of Si donors (Si_{Ga}) in GaAs," *Phys. Rev. Lett.*, vol. 72, no. 10, p. 1490, 1994.

[58] R. M. Feenstra, G. Meyer, F. Moresco, and K. H. Rieder, "Low-temperature scanning tunneling spectroscopy of n-type GaAs(110) surfaces," *Phys. Rev. B*, vol. 66, no. 16, p. 165204, 2002.

[59] C. Domke, P. Ebert, and K. Urban, "Atomic-scale properties of the amphoteric dopant Si in GaAs(110) surfaces," *Surf. Sci.*, vol. 415, no. 3, p. 285, 1998.

[60] S. Loth, M. Wenderoth, K. Teichmann, and R. G. Ulbrich, "Band structure related wave-function symmetry of amphoteric Si dopants in GaAs," *Solid State Commun.*, vol. 145, no. 11, p. 551, 2008.

[61] A. M. Yakunin, A. Y. Silov, P. M. Koenraad, J. H. Wolter, W. Van Roy, J. De Boeck, J.-M. Tang, and M. E. Flatté, "Spatial structure of an individual Mn acceptor in GaAs," *Phys. Rev. Lett.*, vol. 92, no. 21, p. 216806, 2004.

[62] A. Depuydt, C. Van Haesendonck, N. S. Maslova, V. I. Panov, S. V. Savinov, and P. I. Arseev, "Scanning tunneling microscopy and spectroscopy at low temperatures of the (110) surface of Te-doped GaAs single crystals," *Phys. Rev. B*, vol. 60, p. 2619, 1999.

[63] J. Bocquel, V. R. Kortan, C. Şahin, R. P. Campion, B. L. Gallagher, M. E. Flatté, and P. M. Koenraad, "Core-state manipulation of single Fe impurities in GaAs with a scanning tunneling microscope," *Phys. Rev. B*, vol. 87, p. 075421, 2013.

[64] J. K. Garleff, A. P. Wijnheijmer, A. Y. Silov, J. van Bree, W. Van Roy, J.-M. Tang, M. E. Flatté, and P. M. Koenraad, "Enhanced binding energy of manganese acceptors close to the GaAs(110) surface," *Phys. Rev. B*, vol. 82, p. 035303, 2010.

[65] R. M. Feenstra, J. M. Woodall, and G. D. Pettit, "Observation of bulk defects by scanning tunneling microscopy and spectroscopy: Arsenic antisite defects in GaAs," *Phys. Rev. Lett.*, vol. 71, p. 1176, 1993.

[66] G. Münnich, A. Donarini, M. Wenderoth, and J. Repp, "Fixing the energy scale in scanning tunneling microscopy on semiconductor surfaces," *Phys. Rev. Lett.*, vol. 111, p. 216802, 2013.

[67] R. M. Feenstra, "Electrostatic potential for a hyperbolic probe tip near a semiconductor," *J. Vac. Sci. Technol. B*, vol. 21, no. 5, p. 2080, 2003.

[68] S. Loth, M. Wenderoth, R. G. Ulbrich, S. Malzer, and G. H. Döhler, "Connection of anisotropic conductivity to tip-induced space-charge layers in scanning tunneling spectroscopy of p-doped GaAs," *Phys. Rev. B*, vol. 76, no. 23, p. 235318, 2007.

[69] K. Teichmann, M. Wenderoth, S. Loth, R. G. Ulbrich, J. K. Garleff, A. P. Wijnheijmer, and P. M. Koenraad, "Controlled charge switching on a single donor with a scanning tunneling microscope," *Phys. Rev. Lett.*, vol. 101, no. 7, p. 076103, 2008.

[70] A. D. Giddings, J. G. Keizer, M. Hara, G. J. Hamhuis, H. Yuasa, H. Fukuzawa, and P. M. Koenraad, "Composition profiling of InAs quantum dots and wetting layers by atom probe tomography and cross-sectional scanning tunneling microscopy," *Phys. Rev. B*, vol. 83, p. 205308, 2011.

[71] C. Sun, G. Wang, J. E. Bowers, B. Brar, H. Blank, H. Kroemer, and M. H. Pilkuhn, "Optical investigations of the dynamic behavior of GaSb/GaAs quantum dots," *Appl. Phys. Lett.*, vol. 68, no. 11, p. 1543, 1996.

[72] B. Grandidier, Y. M. Niquet, B. Legrand, J. P. Nys, C. Priester, D. Stiévenard, J. M. Gérard, and V. Thierry-Mieg, "Imaging the Wave-function amplitudes in cleaved semiconductor quantum boxes," *Phys. Rev. Lett.*, vol. 85, p. 1068, 2000.

[73] K. Teichmann, M. Wenderoth, H. Prüser, K. Pierz, H. W. Schumacher, and R. G. Ulbrich, "Harmonic oscillator wave functions of a self-assembled InAs quantum dot measured by scanning tunneling microscopy," *Nano Lett.*, vol. 13, no. 8, p. 3571, 2013.

[74] S. Krause, L. Berbil-Bautista, G. Herzog, M. Bode, and R. Wiesendanger, "Current-induced magnetization switching with a spin-polarized scanning tunneling microscope," *Science*, vol. 317, no. 5844, p. 1537, 2007.

[75] A. A. Khajetoorians, J. Wiebe, B. Chilian, and R. Wiesendanger, "Realizing all-spin-based logic operations atom by atom," *Science*, vol. 332, no. 6033, p. 1062, 2011.

[76] A. Li Bassi, C. S. Casari, D. Cattaneo, F. Donati, S. Foglio, M. Passoni, C. E. Bottani, P. Biagioni, A. Brambilla, M. Finazzi, F. Ciccacci, and L. Duò, "Bulk Cr tips for scanning tunneling microscopy and spin-polarized scanning tunneling microscopy," *Appl. Phys. Lett.*, vol. 91, no. 17, p. 173120, 2007.

[77] A. Schlenhoff, S. Krause, G. Herzog, and R. Wiesendanger, "Bulk Cr tips with full spatial magnetic sensitivity for spin-polarized scanning tunneling microscopy," *Appl. Phys. Lett.*, vol. 97, no. 8, p. 083104, 2010.

[78] D. Wortmann, S. Heinze, P. Kurz, G. Bihlmayer, and S. Blügel, "Resolving complex atomic-scale spin structures by spin-polarized scanning tunneling microscopy," *Phys. Rev. Lett.*, vol. 86, p. 4132, 2001.

[79] B. Marquardt, M. Geller, A. Lorke, D. Reuter, and A. D. Wieck, "Using a two-dimensional electron gas to study nonequilibrium tunneling dynamics and charge storage in self-assembled quantum dots," *Appl. Phys. Lett.*, vol. 95, no. 2, p. 022113, 2009.

[80] M. Geller, B. Marquardt, A. Lorke, D. Reuter, and A. D. Wieck, "A two-dimensional electron gas as a sensitive detector for time-resolved tunneling measurements on self-assembled quantum dots," *Nanoscale Res. Lett.*, vol. 5, no. 5, p. 829, 2010.

[81] A. Marent, T. Nowozin, J. Gelze, F. Luckert, and D. Bimberg, "Hole-based memory operation in an InAs/GaAs quantum dot heterostructure," *Appl. Phys. Lett.*, vol. 95, no. 24, p. 242114, 2009.

[82] T. Nowozin, A. Marent, G. Hönig, A. Schliwa, D. Bimberg, A. Beckel, B. Marquardt, A. Lorke, and M. Geller, "Time-resolved high-temperature detection with single charge resolution of holes tunneling into many-particle quantum dot states," *Phys. Rev. B*, vol. 84, p. 075309, 2011.

[83] R. Timm, H. Eisele, A. Lenz, S. K. Becker, J. Grabowski, T.-Y. Kim, L. Müller-Kirsch, K. Pötschke, U. W. Pohl, D. Bimberg, and M. Dähne, "Structure and intermixing of GaSb/GaAs quantum dots," *Appl. Phys. Lett.*, vol. 85, no. 24, p. 5890, 2004.

[84] B. Liang, A. Lin, N. Pavarelli, C. Reyner, J. Tatebayashi, K. Nunna, J. He, T. J. Ochalski, G. Huyet, and D. L. Huffaker, "GaSb/GaAs type-II quantum dots grown by droplet epitaxy," *Nanotechnology*, vol. 20, no. 45, p. 455604, 2009.

[85] R. Timm, H. Eisele, A. Lenz, L. Ivanova, G. Balakrishnan, D. L. Huffaker, and M. Dähne, "Self-organized formation of GaSb/GaAs quantum rings," *Phys. Rev. Lett.*, vol. 101, no. 25, p. 256101, 2008.

[86] R. Timm, H. Eisele, A. Lenz, L. Ivanova, V. Vossebürger, T. Warming, D. Bimberg, I. Farrer, D. A. Ritchie, and M. Dähne, "Confined states of individual type-II GaSb/GaAs quantum rings studied by cross-sectional scanning tunneling spectroscopy," *Nano Lett.*, vol. 10, no. 10, p. 3972, 2010.

[87] M. Ahmad Kamarudin, M. Hayne, R. J. Young, Q. D. Zhuang, T. Ben, and S. Molina, "Tuning the properties of exciton complexes in self-assembled GaSb/GaAs quantum rings," *Phys. Rev. B*, vol. 83, no. 11, p. 1, 2011.

[88] P. Offermans, P. M. Koenraad, J. H. Wolter, D. Granados, J. M. García, V. M. Fomin, V. N. Gladilin, and J. T. Devreese, "Atomic-scale structure of self-assembled In(Ga)As quantum rings in GaAs," *Appl. Phys. Lett.*, vol. 87, no. 13, p. 131902, 2005.

[89] P. B. Joyce, T. J. Krzyzewski, G. R. Bell, B. A. Joyce, and T. S. Jones, "Composition of InAs quantum dots on GaAs(001): Direct evidence for (In,Ga)As alloying," *Phys. Rev. B*, vol. 58, p. R15981, 1998.

[90] Q. Gong, P. Offermans, R. Nötzel, P. M. Koenraad, and J. H. Wolter, "Capping process of InAs/GaAs quantum dots studied by cross-sectional scanning tunneling microscopy," *Appl. Phys. Lett.*, vol. 85, no. 23, p. 5697, 2004.

[91] R. Blossey and A. Lorke, "Wetting droplet instability and quantum ring formation," *Phys. Rev. E*, vol. 65, no. 2, p. 021603, 2002.

[92] G. Balakrishnan, J. Tatebayashi, A. Khoshakhlagh, S. H. Huang, A. Jallipalli, L. R. Dawson, and D. L. Huffaker, "III/V ratio based selectivity between strained Stranski-Krastanov and strain-free GaSb quantum dots on GaAs," *Appl. Phys. Lett.*, vol. 89, no. 16, p. 161104, 2006.

[93] S. H. Huang, G. Balakrishnan, A. Khoshakhlagh, A. Jallipalli, L. R. Dawson, and D. L. Huffaker, "Strain relief by periodic misfit arrays for low defect density GaSb on GaAs," *Appl. Phys. Lett.*, vol. 88, no. 13, p. 131911, 2006.

[94] M. Ahmad Kamarudin, M. Hayne, Q. D. Zhuang, O. Kolosov, T. Nuytten, V. V. Moshchalkov, and F. Dinelli, "GaSb quantum dot morphology for different growth temperatures and the dissolution effect of the GaAs capping layer," *J. Phys. D: Appl. Phys.*, vol. 43, no. 6, p. 065402, 2010.

[95] M. Hayne, J. Maes, S. Bersier, V. V. Moshchalkov, A. Schliwa, L. Müller-Kirsch, C. Kapteyn, R. Heitz, and D. Bimberg, "Electron localization by self-assembled GaSb/GaAs quantum dots," *Appl. Phys. Lett.*, vol. 82, no. 24, p. 4355, 2003.

[96] A. Schliwa, M. Winkelnkemper, and D. Bimberg, "Impact of size, shape, and composition on piezoelectric effects and electronic properties of In(Ga)As/GaAs quantum dots," *Phys. Rev. B*, vol. 76, p. 205324, 2007.

[97] K. Thompson, D. Lawrence, D. J. Larson, J. D. Olson, T. F. Kelly, and B. Gorman, "In situ site-specific specimen preparation for atom probe tomography," *Ultramicroscopy*, vol. 107, no. 2, p. 131, 2007.

[98] N. N. Ledentsov, J. Böhrer, M. Beer, F. Heinrichsdorff, M. Grundmann, D. Bimberg, S. V. Ivanov, B. Y. Meltser, S. V. Shaposhnikov, I. N. Yassievich, N. N. Faleev, P. S. Kop'ev, and Z. I. Alferov, "Radiative states in type-II GaSb/GaAs quantum wells," *Phys. Rev. B*, vol. 52, p. 14058, 1995.

[99] K. Gradkowski, T. J. Ochalski, D. P. Williams, S. B. Healy, J. Tatebayashi, G. Balakrishnan, E. P. O'Reilly, G. Huyet, and D. L. Huffaker, "Coulomb effects in type-II Ga(As)Sb quantum dots," *Phys. Status Solidi B*, vol. 246, no. 4, p. 752, 2009.

[100] W. M. Haynes, *CRC Handbook of chemistry and physics, 94th ed.* Taylor and Francis, 2014.

[101] A. Luque and A. Martí, "Increasing the efficiency of ideal solar cells by photon induced transitions at intermediate levels," *Phys. Rev. Lett.*, vol. 78, p. 5014, 1997.

[102] L. Cuadra, A. Martí, and A. Luque, "Type II broken band heterostructure quantum dot to obtain a material for the intermediate band solar cell," *Phys. E*, vol. 14, no. 1, p. 162, 2002.

[103] R. B. Laghumavarapu, A. Moscho, A. Khoshakhlagh, M. El-Emawy, L. F. Lester, and D. L. Huffaker, "GaSb/GaAs type II quantum dot solar cells for enhanced infrared spectral response," *Appl. Phys. Lett.*, vol. 90, no. 17, p. 173125, 2007.

[104] T. Nowozin, L. Bonato, A. Högner, A. Wiengarten, D. Bimberg, W.-H. Lin, S.-Y. Lin, C. J. Reyner, B. L. Liang, and D. L. Huffaker, "800 meV localization energy in GaSb/GaAs/Al$_{0.3}$Ga$_{0.7}$As quantum dots," *Appl. Phys. Lett.*, vol. 102, no. 5, p. 052115, 2013.

[105] A. Mikkelsen, N. Skold, L. Ouattara, M. Borgstrom, J. N. Andersen, L. Samuelson, W. Seifert, and E. Lundgren, "Direct imaging of the atomic structure inside a nanowire by scanning tunnelling microscopy," *Nat. Mater.*, vol. 3, no. 8, p. 519, 2004.

[106] A. J. Martin, A. H. Hunter, T. W. Saucer, V. Sih, E. A. Marquis, and J. Millunchick, "Atom probe tomography analysis of different modes of Sb intermixing in GaSb quantum dots and wells," *Appl. Phys. Lett.*, vol. 103, no. 12, p. 122102, 2013.

[107] A. P. Wijnheijmer, J. K. Garleff, K. Teichmann, M. Wenderoth, S. Loth, and P. M. Koenraad, "Single Si dopants in GaAs studied by scanning tunneling microscopy and spectroscopy," *Phys. Rev. B*, vol. 84, no. 12, p. 125310, 2011.

[108] D. J. Chadi and K. J. Chang, "Energetics of DX-center formation in GaAs and Al$_x$Ga$_{1-x}$As alloys," *Phys. Rev. B*, vol. 39, no. 14, p. 10063, 1989.

[109] P. M. Mooney, "Donor-related levels in GaAs and Al$_x$Ga$_{1-x}$As," *Semicond. Sci. Tech.*, vol. 6, no. 10B, p. B1, 1991.

[110] J. Wang, T. A. Arias, J. D. Joannopoulos, G. W. Turner, and O. L. Alerhand, "Scanning-tunneling-microscopy signatures and chemical identifications of the (110) surface of Si-doped GaAs," *Phys. Rev. B*, vol. 47, no. 16, p. 10326, 1993.

[111] Z. Yi, Y. Ma, and M. Rohlfing, "Silicon donors at the GaAs(110) surface: A first principles study," *J. Phys. Chem. C*, vol. 115, no. 47, p. 23455, 2011.

[112] M. Hayne, A. Usher, A. S. Plaut, and K. Ploog, "Optically induced density depletion of the two-dimensional electron system in GaAs/Al$_x$Ga$_{1-x}$As heterojunctions," *Phys. Rev. B*, vol. 50, pp. 17208–17216, 1994.

[113] P. D. Hodgson, R. J. Young, M. A. Kamarudin, Q. D. Zhuang, and M. Hayne, "Hole migration and optically induced charge depletion in GaSb/GaAs wetting layers and quantum rings," *Phys. Rev. B*, vol. 88, p. 155322, 2013.

[114] K. Seeger, *Semiconductor physics: An introduction, 9th ed.* Springer-Verlag, 2004.

[115] J. Repp, G. Meyer, F. E. Olsson, and M. Persson, "Controlling the charge state of individual gold adatoms," *Science*, vol. 305, no. 5683, p. 493, 2004.

[116] J. Yang, S. C. Erwin, K. Kanisawa, C. Nacci, and S. Fölsch, "Emergent multistability in assembled nanostructures," *Nano Lett.*, vol. 11, no. 6, p. 2486, 2011.

[117] M. B. Haider, J. L. Pitters, G. A. DiLabio, L. Livadaru, J. Y. Mutus, and R. A. Wolkow, "Controlled coupling and occupation of silicon atomic quantum dots at room temperature," *Phys. Rev. Lett.*, vol. 102, p. 046805, 2009.

[118] S. R. Schofield, P. Studer, C. F. Hirjibehedin, N. J. Curson, G. Aeppli, and D. R. Bowler, "Quantum engineering at the silicon surface using dangling bonds," *Nat. Commun.*, vol. 4, p. 1649, 2012.

[119] H. Zheng, A. Weismann, and R. Berndt, "Tuning the electron transport at single donors in zinc oxide with a scanning tunneling microscope," *Nat. Commun.*, vol. 5, p. 2992, 2014.

[120] A. J. Heinrich, C. P. Lutz, J. A. Gupta, and D. M. Eigler, "Molecule cascades," *Science*, vol. 298, no. 5597, p. 1381, 2002.

[121] A. Sweetman, S. Jarvis, R. Danza, J. Bamidele, L. Kantorovich, and P. Moriarty, "Manipulating Si(100) at 5 K using qPlus frequency modulated atomic force microscopy: Role of defects and dynamics in the mechanical switching of atoms," *Phys. Rev. B*, vol. 84, p. 085426, 2011.

[122] C. Schirm, M. Matt, F. Pauly, J. C. Cuevas, P. Niebala, and E. Scheer, "A current-driven single atom memory," *Nat. Nanotechnol.*, vol. 8, p. 645, 2013.

[123] K. Teichmann, M. Wenderoth, S. Loth, J. K. Garleff, A. P. Wijnheijmer, P. M. Koenraad, and R. G. Ulbrich, "Bistable charge configuration of donor systems near the GaAs(110) surfaces," *Nano Lett.*, vol. 11, no. 9, p. 3538, 2011.

[124] C. S. Lent and P. D. Tougaw, "A device architecture for computing with quantum dots," *Proc. IEEE*, vol. 85, no. 4, p. 541, 1997.

[125] D. H. Lee and J. A. Gupta, "Tunable control over the ionization state of single Mn acceptors in GaAs with defect-induced band bending," *Nano Lett.*, vol. 11, no. 5, p. 2004, 2011.

[126] L. Gross, F. Mohn, P. Liljeroth, J. Repp, F. J. Giessibl, and G. Meyer, "Measuring the charge state of an adatom with noncontact atomic force microscopy," *Science*, vol. 324, no. 5933, p. 1428, 2009.

[127] W. M. Reddick and G. A. J. Amaratunga, "Silicon surface tunnel transistor," *Appl. Phys. Lett.*, vol. 67, no. 4, p. 494, 1995.

[128] G. Hoffmann, T. Maroutian, and R. Berndt, "Color view of atomic highs and lows in tunneling induced light emission," *Phys. Rev. Lett.*, vol. 93, p. 076102, 2004.

[129] M. Kemerink, J. W. Gerritsen, J. G. H. Hermsen, P. M. Koenraad, H. van Kempen, and J. H. Wolter, "Low-temperature scanning-tunneling microscope for luminescence measurements in high magnetic fields," *Rev. Sci. Instrum.*, vol. 72, no. 1, p. 132, 2001.

[130] U. Håkanson, M. K.-J. Johansson, M. Holm, C. Pryor, L. Samuelson, W. Seifert, and M.-E. Pistol, "Photon mapping of quantum dots using a scanning tunneling microscope," *Appl. Phys. Lett.*, vol. 81, no. 23, p. 4443, 2002.

[131] T. Tsuruoka, Y. Ohizumi, and S. Ushioda, "Light intensity imaging of single InAs quantum dots using scanning tunneling microscope," *Appl. Phys. Lett.*, vol. 82, no. 19, p. 3257, 2003.

[132] R. Berndt and J. K. Gimzewski, "Injection luminescence from CdS(11 − 20) studied with scanning tunneling microscopy," *Phys. Rev. B*, vol. 45, p. 14095, 1992.

[133] X. L. Guo, D. Fujita, N. Niori, K. Sagisaka, and K. Onishi, "Scanning tunneling microscopy luminescence from nanoscale surface of GaAs(110)," *Surf. Sci.*, vol. 601, no. 22, p. 5280, 2007.

[134] D. H. Lee and J. A. Gupta, "Tunable field control over the binding energy of single dopants by a charged vacancy in GaAs," *Science*, vol. 330, no. 6012, p. 1807, 2010.

[135] H. Ohno, "Making nonmagnetic semiconductors ferromagnetic," *Science*, vol. 281, no. 5379, p. 951, 1998.

[136] A. H. MacDonald, P. Schiffer, and N. Samarth, "Ferromagnetic semiconductors: Moving beyond (Ga,Mn)As," *Nat. Mater.*, vol. 4, p. 195, 2005.

[137] D. D. Awschalom and M. E. Flatté, "Challenges for Semiconductor Spintronics," *Nat. Phys.*, vol. 3, p. 153, 2007.

[138] T. Dietl, "A ten-year perspective on dilute magnetic semiconductors and oxides," *Nat. Mater.*, vol. 9, p. 965, 2010.

[139] M. Wang, R. P. Campion, A. W. Rushforth, K. W. Edmonds, C. T. Foxon, and B. L. Gallagher, "Achieving high Curie temperature in (Ga,Mn)As," *Appl. Phys. Lett.*, vol. 93, no. 13, p. 132103, 2008.

[140] J. De Boeck, R. Oesterholt, A. Van Esch, H. Bender, C. Bruynseraede, C. Van Hoof, and G. Borghs, "Nanometer-scale magnetic MnAs particles in GaAs grown by molecular beam epitaxy," *Appl. Phys. Lett.*, vol. 68, no. 19, p. 2744, 1996.

[141] S. Kuroda, N. Nishizawa, K. Takita, M. Mitome, Y. Bando, K. Osuch, and T. Dietl, "Origin and control of high-temperature ferromagnetism in semiconductors," *Nat. Mater.*, vol. 6, p. 440, 2007.

[142] D. W. Rench, P. Schiffer, and N. Samarth, "Structural and magnetic characteristics of MnAs nanoclusters embedded in Be-doped GaAs," *Phys. Rev. B*, vol. 84, p. 094434, 2011.

[143] B. Rache Salles, J. C. Girard, C. David, F. Offi, F. Borgatti, M. Eddrief, V. H. Etgens, L. Simonelli, M. Marangolo, and G. Panaccione, "Electronic properties of embedded MnAs nano-clusters in a GaAs matrix and (Ga,Mn)As films: Evidence of distinct metallic character," *Appl. Phys. Lett.*, vol. 100, no. 20, p. 203121, 2012.

[144] B. Grandidier, J. P. Nys, C. Delerue, D. Stiévenard, Y. Higo, and M. Tanaka, "Atomic-scale study of GaMnAs/GaAs layers," *Appl. Phys. Lett.*, vol. 77, no. 24, p. 4001, 2000.

[145] S. J. C. Mauger, M. Bozkurt, P. M. Koenraad, A. D. Giddings, R. P. Campion, and B. L. Gallagher, "Short–period (Ga,Mn)As/(Al,Ga)As multilayer structures studied by cross–sectional scanning tunneling microscopy," *Phys. Rev. B*, vol. 84, p. 104432, 2011.

[146] A. M. Yakunin, A. Y. Silov, P. M. Koenraad, J.-M. Tang, M. E. Flatté, J.-L. Primus, W. Van Roy, J. De Boeck, A. M. Monakhov, K. S. Romanov, I. E. Panaiotti, and N. S. Averkiev, "Warping a single Mn acceptor wavefunction by straining the GaAs host," *Nat. Mater.*, vol. 6, p. 512, 2007.

[147] M. Bozkurt, V. A. Grant, J. M. Ulloa, R. P. Campion, C. T. Foxon, E. Marega, G. J. Salamo, and P. M. Koenraad, "Atomic scale characterization of Mn doped InAs/GaAs quantum dots," *Appl. Phys. Lett.*, vol. 96, no. 4, p. 042108, 2010.

[148] S. Mauger, "Atomic–scale study of Mn– and Sb– containing III–V semiconductor nanostructures." thesis, 2013.

[149] M. Zhu, X. Li, G. Xiang, and N. Samarth, "Random telegraph noise from magnetic nanoclusters in the ferromagnetic semiconductor (Ga,Mn)As," *Phys. Rev. B*, vol. 76, p. 201201, 2007.

[150] P. M. Mooney, "Deep donor levels (DX centers) in III–V semiconductors," *J. Appl. Phys.*, vol. 67, no. 3, p. R1, 1990.

List of Abbreviations

AFM	atomic force microscopy
APT	atom probe tomography
DFT	density functional theory
DLTS	deep level transient spectroscopy
LDOS	local density of states
LT	low–temperature
MBE	molecular beam epitaxy
PL	photoluminescence
QD	quantum dot
QW	quantum well
RT	room–temperature
SNM	scanning noise microscopy
SP-STM	spin–polarized scanning tunneling microscopy
STL	scanning tunneling luminescence
STM	scanning tunneling microscopy
STS	scanning tunneling spectroscopy
TIBB	tip–induced band bending
UHV	ultra–high vacuum
X-STM	cross–sectional scanning tunneling microscopy

Probing Bistable Si Dynamics and GaSb Nanostructures in GaAs

Scanning tunneling microscopy (STM) is a technique based on quantum tunneling between a very sharp tip and a conducting sample. The tip scans over the surface, mapping it with atomic resolution. In this thesis, STM is used to probe the properties of various nanostructures and dopants on the GaAs {110} surfaces.

Self-assembled GaSb quantum dots (QDs) in GaAs grown by molecular beam epitaxy (MBE) disintegrate into a whole spectrum of nanostructures during overgrowth. The shapes that appear are visualized with cross-sectional (X-)STM and vary from pure intact GaSb dots in the form of knotted pyramids to ring-like structures and to clusters of small islands with more intermixing of As and Sb. In Chap. 3 a range of growth parameters is investigated to find optimal conditions for growing the best preserved pure QDs. It turns out that lower thermal energy during overgrowth with GaAs capping layers favors QD shape retention. Scanning tunneling spectroscopy (STS) on a quantum nanostructure reveals discrete energy levels that are linked to its size and confirms the strong hole confinement of the material system. Furthermore, the structural results of X-STM are compared to and corroborated by complementary methods performed elsewhere, e.g. $\mathbf{k} \cdot \mathbf{p}$ calculations, atom probe tomography (APT) and photoluminescence (PL). In Chap. 4 the possibility to limit the Sb diffusion during MBE growth by using Al in the capping layer is demonstrated, which enables more control over the nanostructure morphology. The observed nanostructures with X-STM are larger and retain their shape better in the case of AlAs and AlGaAs capping layers with respect to overgrowth with GaAs. However, often structural defects are found around the larger QDs in the form of stacking faults, limiting the PL response of the material. This suggests that smaller nanostructures combined with Al in the

capping layer comprises the best solution for obtaining GaSb QDs in GaAs with a good optical quality.

The electronic properties of single dopant atoms have a large influence on their local surroundings. In our low-temperature (LT-)STM, the Si dopant in the GaAs (110) surface layer was studied, that exhibits switching between a negative and positive charge state. In Chap. 5, bistable behavior of Si dopants is characterized by using the STM tip as a local probe and manipulating the charge state with a laser. The illumination produces electron-hole pairs in the sample, which enables the fast recombination and escape of electrons bound to the Si dopant. Therefore, we conclude electron escape and capture processes play an important role in the switching dynamics. This is further explored in Chap. 6, where the random telegraph noise of a single bistable Si atom is recorded by restricting the tip on top of the dopant and following the charge state in time. A physical model taking into account the tunneling barriers connects the observed switching frequency and charge state occupation with the applied tunneling conditions. Through understanding the dynamical behavior of the switching Si, the dopant atom is employed as a memory element. Using the tip as a gate, the dopant is manipulated into the negative or positive charge state and can be independently read out, effectively demonstrating a non-volatile single atom memory in the solid state.

Scanning tunneling luminescence (STL) is used to optically investigate Si dopants in GaAs, which is discussed in Chap. 7. There are atomic-scale variations in the STL intensity that directly correlate to those in the topographic image. The origin of this effect is the change of electron accumulation in the sample surface directly below the STM tip, due to the tip height variations during scanning. This means that the luminescence spectrum contains information from a nm-sized area, allowing the direct optical characterization of nanostructures and dopants. Another extension of the standard STM technique is created by employing magnetically sensitive tips for performing spin-polarized (SP-)STM. In Chap. 8, magnetic MnAs nanoclusters in GaAs are probed with antiferromagnetic Cr tips. Spectroscopic measurements reveal the metallic character of these nanostructures. Furthermore, bistable switching of relatively small MnAs clusters between two magnetic states is observed, indicating a low blocking temperature for these structures, while the larger islands remain stable. This demonstrates the importance of the control over the cluster sizes for developing room-temperature ferromagnetic semiconductor material.

The STM is a versatile tool for probing the local properties of nanostructures and dopants in semiconductor materials. For this thesis, the unparalleled spatial resolution was combined with various techniques to obtain

structural, electronic, time-resolved, optical and magnetic information from the surface to study physical phenomena at the atomic scale.

Samenvatting

Scanning tunneling microscopie (STM) is een techniek gebaseerd op quantum tunneling tussen een zeer scherpe tip en een geleidend materiaal. De tip scant over een oppervlak, dat met atomaire resolutie in kaart wordt gebracht. In dit proefschrift is de STM ingezet om de eigenschappen van verschillende nanostructuren en doteringsatomen te onderzoeken, die zich in het GaAs {110} oppervlak bevinden.

Zelf–geassembleerde GaSb quantum dots (QDs) in GaAs die zijn gegroeid met moleculaire bundel epitaxy (MBE) desintegreren tijdens de groei naar een volledig spectrum van nanostructuren. De vormen die verschijnen worden in dit werk gevisualiseerd met cross–sectionele (X–)STM en variëren van pure intacte GaSb dots lijkend op een afgeknotte pyramide tot ring–achtige structuren en ook tot clusters van kleine eilanden met meer inmenging tussen As en Sb. In Hs. 3 zijn een reeks van groeiparameters onderzocht om optimale omstandigheden te vinden voor het groeien van de best geconserveerde pure QDs. Het blijkt dat lagere thermische energie gedurende de overgroei met GaAs capping lagen gunstig is voor het behouden van de QD vorm. Scanning tunneling spectroscopie (STS) op een quantum nanostructuur onthult discrete energie–niveaus die kunnen worden gelinkt aan zijn grootte en dit bevestigt de sterke electronische gat opsluiting van dit materiaal systeem. Verder zijn de structurele resultaten van X–STM vergeleken met en bevestigd door aan–vullende methoden die in andere onderzoeksgroepen zijn uitgevoerd, nl. $\mathbf{k} \cdot \mathbf{p}$ berekeningen, atoom probe tomografie (APT) en fotoluminiscentie (PL). In Hs. 4 wordt de mogelijkheid om Sb diffusie te beperken gedemonstreerd, door gedurende de MBE groei Al in de capping laag te gebruiken, wat tot meer controle over de nanostructuur morfologie leidt. De geobserveerde nanostruc–turen met X–STM zijn groter en behouden hun vorm beter in het geval van AlAs en AlGaAs capping lagen, vergeleken met overgroei met GaAs. Echter, vaak vormen er structurele defecten rondom de grotere QDs in de vorm van

stapelfouten, wat zorgt voor een lagere PL intensiteit van het materiaal. Dit suggereert dat kleinere nanostructuren gecombineerd met Al in de capping laag de beste oplossing zijn voor het maken van GaSb QDs in GaAs met een goede optische kwaliteit.

De electronische eigenschappen van enkele doteringsatomen hebben een grote invloed op hun locale omgeving. In onze lage-temperaturen STM is het Si atoom in de GaAs (110) oppervlaktelaag bestudeerd, die het spontaan schakelen laat zien tussen een negatieve en positieve ladingstoestand. In Hs. 5 is bistabiel gedrag van Si doteringsatomen gekarakteriseerd door de STM tip te gebruiken als een lokale probe, terwijl de ladingstoestand wordt gemanipuleerd met een laser. De belichting produceert electron–gat paren in het materiaal, wat snelle recombinatie en ontsnapping mogelijk maakt van de electronen die gebonden zijn aan het Si atoom. We concluderen daarom dat electron ontsnappings– en invangprocessen een belangrijke rol spelen in de schakelingsdynamica. Dit is verder onderzocht in Hs. 6, waar "random telegraph noise" van een enkel Si atoom is vastgelegd door de tip te fixeren bovenop het doteringsatoom en vervolgens de ladingstoestand in de tijd te volgen. Een fysisch model dat rekening houdt met de tunnel-barrières maakt een connectie tussen de geobserveerde schakelingsfrequentie en ladingstoe–stand bezetting met de aangelegde tunnelcondities. Door het begrijpen van het dynamisch gedrag van het schakelende Si, kan het doteringsatoom wor–den ingezet als geheugenelement. In dit experiment wordt de tip gebruikt als een gate, waarmee het Si atoom kan worden geschreven naar de negatieve of positieve ladingstoestand. Deze kan vervolgens onafhankelijk worden uit–gelezen, waardoor effectief een atomair geheugen is gedemonstreerd in de vaste stof.

Scanning tunneling luminescentie (STL) is gebruikt om optisch Si doter–ingsatomen in GaAs te onderzoeken, wat is uitgewerkt in Hs. 7. Er zijn variaties in de STL intensiteit die we direct kunnen corelleren aan de atom–aire corrugatie in de topografie. De oorsprong van dit effect is de verandering van electronen–accumulatie in het oppervlak van het materiaal direct onder de STM tip, door de hoogte–variaties tijdens het scannen. Dit betekent dat het luminescentie spectrum informatie bevat van een gebied op de nm–schaal, wat het potentieel mogelijk maakt om nanostructuren en doteringsatomen direct optisch te karakteriseren. Een andere uitbreiding van de standaard STM techniek wordt bereikt door het gebruik van magnetisch gevoelige tips om spin–gepolariseerde (SP-)STM uit te voeren. In Hs. 8 worden MnAs nan–oclusters in GaAs onderzocht met antiferromagnetische Cr tips. Spectroscopie metingen laten het metallische karakter zien van deze nanostructuren. Verder is het bistabiele schakelen van relatief kleine MnAs clusters tussen twee

magnetische toestanden geobserveerd bij vloeibare stikstof temperatuur. Dit betekent dat deze kleine structuren een lage blokkeringstemperatuur hebben, terwijl de grotere eilanden stabiel blijven. Dit demonstreert het belang van de controle over de cluster-groottes voor de ontwikkeling van kamertemperatuur ferromagnetisch halfgeleider materiaal.

De STM is een veelzijdig werktuig om de lokale eigenschappen van nanostructuren en doteringsatomen in halfgeleider materialen te onderzoeken. Voor dit proefschrift is de zeer hoge ruimtelijke resolutie van deze techniek gecombineerd met verschillende andere methoden om structurele, electronische, tijdsopgeloste, optische en magnetische informatie te verkrijgen van het oppervlak om zo fysische verschijnselen op de atomaire schaal te bestuderen.

Dankwoord

Het werk in dit proefschrift was niet tot stand gekomen zonder de samenwerking met vele anderen en steun van de mensen om mij heen.

Ik wil beginnen met het bedanken van mijn eerste promotor. Paul, nadat je voor ons symposium "Space" in 2007 als dagvoorzitter had opgetreden, bleef mij jouw enthousiasme en inhoudelijke interesse bij. Toen ik in 2010 op zoek ging naar een promotieplaats, kon jij me vrijwel direct overtuigen om bij de PSN groep te komen en hier vier jaar mijn onderzoek te gaan doen. Ik ben ontzettend dankbaar voor je begeleiding en steun. Je hebt me altijd vertrouwd en veel ruimte gelaten voor mijn eigen intiatief. Op cruciale momenten (als er weer eens iets stuk was...) toonde je begrip en kon je iedereen op een lijn krijgen.

Dan wil ik mijn mentors van het eerste uur bedanken: Jens, Joris en Ineke. Jullie hebben me veel geleerd, gecorrigeerd, aangemoedigd en geholpen, maar bovenal hebben we samen veel plezier gehad! Jullie motivatie en werkmentaliteit waren een voorbeeld voor mij. Joost, door jouw kritische houding, geduld en vooral je interesse in de fysica heb je mij geholpen om verder te gaan in mijn onderzoek. Niet zelden gingen onze discussies aan de koffietafel ook over allerlei andere onderwerpen, soms aangemoedigd door een recente pubquiz, waar ik altijd veel plezier aan beleefde.

I also want to express many thanks to all the international collaborators that enabled the work I did in Eindhoven by supplying samples, by doing complementary measurements and by having scientific discussions that allowed me to progress and see things from a different perspective. Joanna, acting as my second promotor, and your students Andy and Matt, and also Manus and Robert, without your QD samples I would be nowhere! Also thanks to Tobias and Martin for bringing the QD2D project so far. Rolf, I owe you much for supplying the noise electronics and helping with the interpretation. Nithin and Dave, with your samples you allowed me to employ SP-STM on

a semiconductor system for the first time.

René, Rian, Frank, Martine, Marcel, Peter en Jos, jullie waren de onmisbare technici die vaak op zeer korte termijn door mij werden gevraagd met iets te helpen, en dit deden jullie zonder te morren. Daar ben ik erg dankbaar voor! Margriet, Annebee, Simone en Thérèse-Anne, heel erg bedankt voor jullie steun en gezellige gesprekken al die jaren. Erik, Andrea, Rob en Jos, de wetenschappelijke discussies met jullie heb ik altijd als erg waardevol ervaren. Ik zal jullie allemaal gaan missen!

Ramon, Juanita, Sam, Steven, Andrei, Devin, Murat and my bachelor students Paul en Joerie, we had many interesting and fun discussions and I enjoyed working with you a lot. Tilman and Sebastièn, you made life in the office very entertaining. And of course the latest additions to our little SPM group: Davide, Christian, Rianne and Sebastian. I am aware you often suffered through my relentless advice and suggestions... Luckily we had a great time working in the office and the lab together!

Ikaros, Joris, Tilman, Ryan, Anthony, Sam, Devin, Diana and Joost, we organized various beer, wine, whiskey and cocktail tastings over the years which sparked many interesting conversations on those happy evenings! I also enjoy thinking back to the good times we had at international conferences: Steven (formal dinner, really?), Davide (remember the dogs...), Sam and Juanita (almost mist the boat), Thuy, Anthony and Ikaros (Churrrooos!).

Furthermore I want to thank all the other PhD students, postdocs, technicians and staffmembers that made working in PSN so enjoyable!

Dank ook aan al mijn vrienden: de gezelligheid en avondjes uit met jullie gaven me de energie die ik nodig had om het promotieonderzoek te doen en te genieten van het leven!

Pap en mam, jullie zijn mijn bron van inspiratie en mijn grote voorbeeld. Door jullie eindeloze enthousiasme voor wetenschap ben ik ook aangestoken en heb ik gekozen voor een promotieonderzoek. Ik waardeer enorm de steun en het advies die jullie gaven wanneer het allemaal wat minder ging en ik het even niet meer wist.

De belangrijkste persoon bewaar ik voor het laatst. Lieve Jantine, mijn geliefde en soulmate, jij hebt me verder gebracht in het leven door jouw liefde, steun, begrip en kracht. Ik heb zoveel van je geleerd! Soms zat ik vast tijdens experimenten, modellen maken of het schrijven van dit proefschrift, maar jij wist me altijd weer op te beuren en te motiveren om door te gaan. Ik hou van jou!

List of Publications

E. P. Smakman, S. Mauger, D. W. Rench, N. Samarth, P. M. Koenraad,
"Structural, electronic and magnetic properties of single MnAs nanoclusters in GaAs",
in preparation.

E. P. Smakman, J. G. Keizer, C. M. Krammel, P. M. Koenraad,
"Scanning tunneling luminescence on Si dopants in GaAs",
submitted.

E. P. Smakman, P. M. Koenraad,
"Bistable Si Dopants in the GaAs (110) Surface",
submitted.

E. P. Smakman, M. DeJarld, M. Luengo-Kovak, A. J. Martin, V. Sih, P. M. Koenraad, J. Millunchick,
"Height stabilization of GaSb/GaAs quantum dots by Al-rich capping",
submitted.

E. P. Smakman, P. L. J. Helgers, J. Verheyen, R. Möller, P. M. Koenraad,
"Tunable switching dynamics of a Single Si Dopant in GaAs (110)",
Phys. Rev. B **90** 041410(R) (2014).

P. D. Hodgson, R. J. Young, M. Ahmad Kamarudin, P. J. Carrington, A. Krier, Q. D. Zhuang, **E. P. Smakman**, P. M. Koenraad, M. Hayne,
"Blueshifts of the emission energy in type-II quantum dot and quantum ring nanostructures",
J. Appl. Phys. **114** 073519 (2013).

M. Hayne, R. J. Young, **E. P. Smakman**, T. Nowozin, P. Hodgson, J. K. Garleff, P. Rambabu, P. M. Koenraad, A. Marent, L. Bonato, A. Schliwa D. Bimberg, "The structural, electronic and optical properties of GaSb/GaAs nanostructures for charge-based memory",
J. Phys. D: Appl. Phys. **46** 264001 (2013).

A. J. Martin, J. Hwang, E. A. Marquis, **E. Smakman**, T. W. Saucer, G. V. Rodriguez, A. H. Hunter, V. Sih, P. M. Koenraad, J. D. Phillips, J. Millunchick, "The disintegration of GaSb/GaAs nanostructures upon capping",
Appl. Phys. Lett. **102** 113103 (2013).

E. P. Smakman, J. van Bree, P. M. Koenraad,
"Laser and voltage manipulation of bistable Si dopants in GaAs (110) surface",
Phys. Rev. B **87** 085414 (2013).

T. Nowozin, A. Marent, L. Bonato, A. Schliwa, D. Bimberg, **E. P. Smakman**, J. K. Garleff, P. M. Koenraad, R. J. Young, M. Hayne,
"Linking structural and electronic properties of high-purity self-assembled GaSb/ GaAs quantum dots",
Phys. Rev. B **86** 035305 (2012).

E. P. Smakman, J. K. Garleff, R. J. Young, M. Hayne, P. Rambabu, P. M. Koenraad,
"GaSb/GaAs quantum dot formation and demolition studied with X-STM",
Appl. Phys. Lett. **100** 142116 (2012).

R. J. Young, **E. P. Smakman**, A. M. Sanchez, P. Hodgson, P. M. Koenraad, M. Hayne,
"Optical observation of single-carrier charging in type-II quantum ring ensembles",
Appl. Phys. Lett. **100** 082104 (2012).

Book: "The Wonder of Nanotechnology", edited by M. Razeghi, L. Esaki, K. von Klitzing,
Chapter 6: "Antimonide Quantum Dot Nanostructures for Novel Photonic Device Applications",
A. Krier, P. J. Carrington, Q. Zhuang, R. J. Young, M. Hayne, L. Qi, J. James, M. C. Wagener, J. R. Botha, P. Koenraad, **E. P. Smakman**,
SPIE, Bellingham, USA (2013).

Not Part of This Thesis

W. J. Engelen, **E. P. Smakman**, D. J. Bakker, O. J. Luiten, E. J. D. Vredenbregt,
"Effective temperature of an ultracold electron source based on near–threshold photoionization",
Ultramicroscopy **136** 73 (2014).

J. H. Northern, G. A. D. Ritchie, **E. P. Smakman**, J. H. van Helden, R. J. Walker, G. Duxbury,
"Chirped quantum cascade laser induced rapid passage signatures in an optically thick gas",
Appl. Phys. B **102** 37 (2011).

J. H. Northern, G. A. D. Ritchie, **E. P. Smakman**, J. H. van Helden, J. Cockburn, G. Duxbury,
"Rapid passage signals induced by chirped quantum cascade laser radiation: K state dependent–delay effects in the ν_2 band of NH_3",
Opt. Lett. **35** 2751 (2010).

Curriculum Vitae

Erwin Paul Smakman
born 17st of January 1986 in Tilburg, the Netherlands

2010-2014   PhD candidate,
Eindhoven University of Technology,
Photonics and Semiconductor Nanophysics

2007-2010   Master Applied Physics
Eindhoven University of Technology

master thesis at Eindhoven University of Technology
Coherence and Quantum Technology
Electron bunches from an ultra-cold plasma source.

internship at Oxford University, UK
Physical Chemistry
Quantum cascade lasers in absorption spectroscopy.

2004-2008   Bachelor Applied Physics,
Eindhoven University of Technology

internship at Eindhoven University of Technology
Coherence and Quantum Technology
Transverse laser profile shaping: Evaluating the PiShaper.

1998—2004   High School (VWO), Theresia Lyceum, Tilburg